UNIVERSITÉ DU QUÉBEC À CHICOUTIMI

THÈSE PRÉSENTÉE À
L'UNIVERSITÉ DU QUÉBEC À CHICOUTIMI
COMME EXIGENCE PARTIELLE
DU DOCTORAT EN INGÉNIÉRIE

par
Saleema Noormohammed

Nanostructured Thin Films for Icephobic Applications

Couches Minces Nanostructurées pour des Applications Glaciophobes

April 2009

## Abstract

Icing on surfaces such as cables or high voltage insulators may often lead to severe safety issues such as power outages in cold winter conditions. Conventional methods used to avoid such icing problems include mechanical deicing where the ice is scraped or broken and chemical deicing where deicers such as ethylene glycol are used. These methods have their own disadvantages of being destructive, expensive and time consuming. A better approach would be to prevent ice from forming in the first place by producing coating materials that are icephobic.

Superhydrophobic surfaces, which demonstrate high water-repellency due to the negligible contact area of water with those surfaces, are also expected to minimize the contact area of ice. A low dielectric constant surface is also expected to reduce the adhesion of ice due to the screening of mirror charges, thereby eliminating one of the strongest interaction forces – the electrostatic forces of attraction at the ice-surface interface.

In the present research work, both concepts were studied by producing superhydrophobic nanorough $low$-$\varepsilon$ dielectric surfaces on aluminum or alumina substrates. Superhydrophobic properties were achieved on surfaces of aluminum or alumina by creating a certain nanoroughness using chemical methods followed by a low surface energy coating of rf-sputtered Teflon® or fluoroalkyl-silane (FAS-17) providing a water contact angle greater than 160°. The same behavior is reported even when the nanorough substrates

were coated with dielectric thin films of ZnO (lower $\varepsilon$) or TiO$_2$ (higher $\varepsilon$). It is found that the superhydrophobic nanorough low surface energy surfaces are also icephobic and the presence of a low dielectric constant surface coating of rf-sputtered Teflon® (lowest $\varepsilon$; $\varepsilon = 2$) allows a considerable reduction of the ice adhesion strength even on non-nanotextured surfaces where ice would stick. The superhydrophobic nanorough *low-$\varepsilon$* surfaces also demonstrate morphological and chemical stability following the detachment of ice.

# Résumé

Le givrage atmosphérique des surfaces des équipements des réseaux électriques, tels que câbles ou isolateurs à haute tension peut conduire à de sérieux risques de sécurité, causés par des pannes de courant dans des conditions hivernales. Les méthodes conventionnelles utilisées afin d'éviter de tels problèmes incluent le déglaçage mécanique, par lequel on racle ou on brise la glace, et les méthodes chimiques à l'aide de d'agents dégivrants comme le glycol éthylique. Ces techniques sont souvent limitées dans leur application et généralement coûteuses en temps et en argent. Une voie intéressante pour éviter ces problèmes est la prévention de l'adhésion et des accumulations de glace par le développement et l'application de revêtements glaciophobes sur les équipements exposés.

Les surfaces superhydrophobes présentant un caractère hydrofuge élevé, grâce à une surface de contact très réduite entre les gouttelettes d'eau et le matériau, sont également susceptibles de réduire l'adhérence entre la glace et la surface. De plus, les surfaces à faible constante diélectrique devraient réduire l'adhérence de la glace au substrat grâce à la diminution des forces électrostatiques, une des principales causes de cette adhérence.

La recherche entreprise dans le cadre de cette thèse de doctorat se base sur les deux concepts ci-haut mentionnés en élaborant des revêtements superhydrophobes diélectriques nanorugeux à faible constante diélectrique sur des substrats d'aluminium ou d'alumine. Des propriétés superhydrophobes ont été obtenues sur des surfaces d'aluminium ou d'alumine

préparées en créant une certaine nanorugosité à l'aide de méthodes chimiques suivies par l'application d'un revêtement à faible énergie de surface, soit une couche de Téflon® déposée par pulvérisation radio fréquence (rf-sputtered Teflon®) ou de fluoroalkylsilane (FAS-17), donnant lieu à un angle de contact supérieur à 160°. Le même comportement est observé lorsque les substrats nanorugeux étaient revêtus d'une couche mince de faible constante diélectrique (ZnO) ou de constante diélectrique élevée ($TiO_2$).

On a constaté que les surfaces superhydrophobes nanorugeux à faible énergie de surface sont aussi glaciophobes. On a constaté également que la présence d'une surface de téflon avec une constante diélectrique relativement faible ($\varepsilon = 2$) permet une réduction importante de l'adhésion de la glace, même si la surface n'est pas nanotexturée. Les surfaces superhydrophobes nanorugeux à faible constante diélectrique ont démontrées également une stabilité morphologique et chimique suite au détachement de la glace.

# Acknowledgements

After years of research, working with a great number of expert scientists, engineers and technicians, this thesis has been finally realized and the work has been greatly valued by the scientific as well as non-scientific community. It is a great pleasure to convey my humble gratitude to all the people involved in building up this thesis.

In the first place, I would like to thank all the sponsors of this research project, namely, the NSERC/Hydro-Quebec/UQAC Industrial Chair on Atmospheric Icing of Power Network Equipment (CIGELE) and the Canada Research Chair on Engineering of Power Network Atmospheric Icing (INGIVRE) at the University of Québec at Chicoutimi. This thesis has been realized in collaboration with l'Institut National de la Recherche Scientifique - Centre Énergie Matériaux Télécommunications (INRS - ÉMT), Varennes, Québec, Canada.

I would like to acknowledge, with a deep sense of gratitude and indebtedness, Prof. Masoud Farzaneh, director of my thesis project, for his valuable suggestions and encouragement. Working with Prof. Farzaneh has been a great pleasure. His originality, experience and contributions in the field of ice have absolutely nourished the value of this thesis. An extremely busy professional, Prof. Farzaneh has always been available and kind in need. It is an honor for me to earn my graduation under his direction.

I am extremely grateful to my co-director, Prof. Royston Paynter, INRS - ÉMT, for his supervision, advice, continuous guidance, suggestions, scientific and technical criticisms and constant encouragement. Particularly, I must thank him for his patience and tolerance with my writing tasks. His truly scientific intuition exceptionally inspired and helped me grow as a student, a researcher and a scientist. I must mention that I had the opportunity to work closely with Prof. Paynter at INRS for XPS measurements and I have enjoyed the way he trained me easily to use the instrument as well as his good humor during the measurements. Thanks Prof. Paynter. I am grateful in every possible way and hope to keep up our collaboration in the future.

I am very grateful to Dr. Richard Menini, Dr. Sergei Kulinich, and Prof. Christophe Volat for accepting to be members of the doctoral examination committee in the midst of all their research and academic activity.

I would like to express my thanks to the directors of graduate studies Prof. Marcel Paquette (retired) and Prof. Duygu Kocaeffe for being present and for their valuable comments and questions raised during my evaluation seminars.

never-ending, but, will not end! Happy moments and laughter along with nice warm cup of tea and delicious snacks gave a boost to cheer me up and stir the work.

It is a pleasure to express my gratitude wholeheartedly to Prof. Farzaneh's family for their warm welcome and kind hospitality in Chicoutimi.

My dearest friends, Jayanta da and Denise, never made me feel the distance between Chicoutimi (where I live) and India (where my parents live). Thank you Jayanta da and Denise for a variety of social activities and for making me feel like family. I must mention that Emeritus Prof. Jayanta Guha, ex-Dean, is a geologist, poet, photographer and musician.

Moussa and Carlos are two other friends who never ceased to encourage me and who were there for me and my family when we were in need. Thanks guys.

I must not proceed further without a mention of my long-time companion, "the winter of Chicoutimi". Thanks to winter and tons of snow for if it did not exist, the world would be missing a good deal of interesting science and my thesis of course. Thanks to Mother Nature for also bestowing upon us a bit of summer showing the light of green life's existence too.

My family back in India deserves a special mention for their immense moral support, encouragement and prayers for the completion of my thesis. Noormohammed, my father, Fathima, my mother, and Malik and Nazeema, my siblings never stopped telling me "Yes YOU can".

Dilip, my beloved husband, is a very important contributor to the successful completion of my thesis. This wouldn't have happened if it was not for his co-operation in science as well as in family life, his sacrifice, his confidence in me, his encouragement, his affection, and his love. His scientific knowledge and research experience in the field was a great advantage for me. There are no words to thank you Dilip. Thanks to your family to have let me be your bride.

"Best for last"... my lovely beautiful daughter Shreya, now five... the best part of my life, of me. I only have tears and no words to thank her. For since she was 18 months old, she has sacrificed a lot and has missed moments every child in those years of age deserves with his or her mom that could have been the most memorable for her. Sometimes week-ends, sometimes evenings... I love you Shreya.

Finally, I would like to thank everybody who was important to the successful realization of this thesis; I apologize that I could not thank them personally one by one.

## Table of Contents

# List of Symbols and Abbreviations

| | |
|---|---|
| $\theta$, CA | Contact angle of water on any surface (°) |
| $\theta_A$ | Advancing contact angle (°) |
| $\theta_R$ | Receding contact angle (°) |
| $\theta'$ | Apparent contact angle (as used in Wenzel and Cassie equations) (°) |
| CAH | Contact angle hysteresis (°) |
| $f$ | Area fraction of the solid in contact with water drop |
| $R_w$ | Roughness factor (as used in Wenzel equation) |
| $W_A$ | Work of adhesion (mNm$^{-1}$) |
| $\gamma_{SV}$ | Surface tension of solid-vapor interface (mNm$^{-1}$) |
| $\gamma_{SL}$ | Surface tension of solid-liquid interface (mNm$^{-1}$) |
| $\gamma_{LV}$ | Surface tension of liquid-vapor interface (mNm$^{-1}$) |
| $\alpha$ | Angle of inclination of a surface (°) |
| $\Omega$ | Volume of drop (μl) |
| $g$ | Gravitational acceleration (9.8 ms$^{-2}$) |
| $\rho$ | Density of drop (gcm$^{-2}$) |
| $\sigma$ | Tensile strength of ice (Nm$^{-2}$) |
| $\tau$ | Shear strength of ice (Nm$^{-2}$) |
| ARF | Adhesion reduction factor |
| $F$ | Adhesion force (N) |
| $q$ | Charge on ice surface (C) |
| $q'$ | Induced image charge (C) |
| $\varepsilon$ | Dielectric constant |
| $r$ | Radius of the beam (m) |

| | |
|---|---|
| $\omega$ | Rotation speed of the beam (or) angular acceleration (ms$^{-2}$) |
| $m$ | Mass of accumulated ice (g) |
| $A$ | Apparent area of sample surface in contact with ice (m$^{-2}$) |
| | |
| TBOT | Tetrabutoxy titanium |
| SA | Stearic acid |
| FAS | fluoroalkyl-silane |
| SAM | Self assembled monolayer |
| | |
| CBD | Chemical bath deposition |
| FESEM | Field emission scanning electron microscope |
| EDX | Energy dispersive X-ray |
| AFM | Atomic force microscope |
| XPS | X-ray photoelectron spectroscopy |
| FT-IR | Fourier transform infrared spectroscopy |
| CAT | Centrifugal adhesion reduction test |

# List of Tables

## List of Figures

# CHAPTER 1

## INTRODUCTION

This chapter provides an introduction to the problems posed by the adhesion of ice to surfaces and a potential solution using the emerging technology of nanoscience. The hypothesis and objectives of the thesis and the methodologies employed to achieve the objectives will be outlined in the following sections.

### 1.1. Introduction

A thick transparent coating of ice formed from freezing rain on stunning bright red cherries (Figure 1.1) and the beautiful landscapes (Figure 1.2) formed as the aftermath of heavy freezing rain activity are a visual feast for nature lovers and amateur photographers.

When it comes to the next images shown in Figures 1.3, 1.4 and 1.5 photographed during the same freezing rain storms in parts of the US in December 2008 and January 2009, the general public is most likely to recognize a worrisome situation. These storms left millions of citizens out of power in the chilling weather conditions for several days, claiming more than 40 fatalities due to blackouts [1].

**Figure 1.1.** Bright red cherries coated with thick transparent ice formed from freezing rain in parts of the US in December 2008 [2]



**Figure 1.2.** A railway line bordered with ice-coated trees arched due to the weight of accumulated ice following freezing rain in parts of the US in January 2009 [3].

**Figure 1.3.** The weight of accumulated ice caused tree branches to break and fall onto the streets in parts of the US leaving thousands of citizens without power in December 2008 and January 2009 [3].
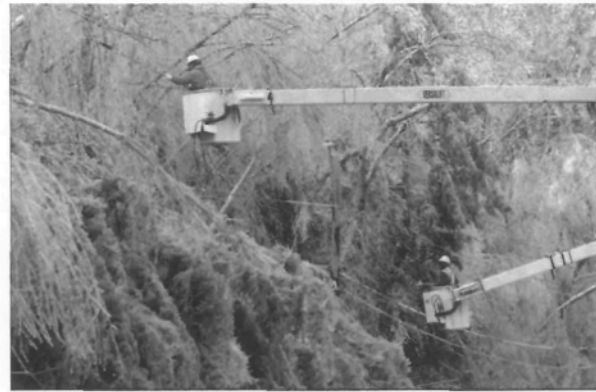


**Figure 1.4.** Tree service crews cutting iced tree limbs to restore power in the US following the December 2008 ice storm [3].
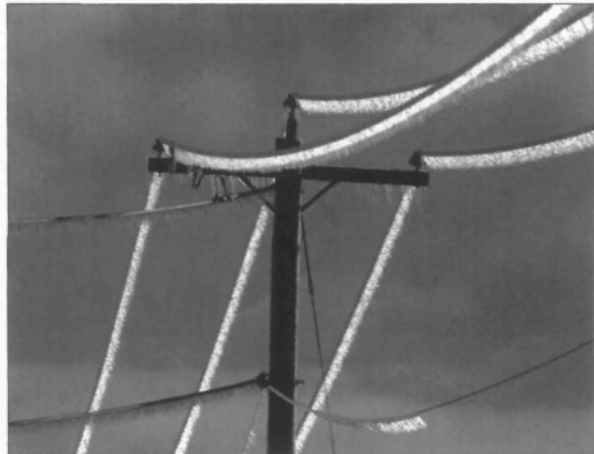
**Figure 1.5.** A glimpse of ice coated power lines in the US following an ice storm that left thousands of citizens without power in December 2008 [3].

Not the least, "The Great Ice Storm" of January 1998 deprived millions of Quebec and Ontario residents of electricity for up to 30 days [4]. Many power lines and more than 1000 pylons collapsed in this event (Figures 1.6 and 1.7) causing more than 25 fatalities due to reasons related to power outages and leading to hundreds of millions of dollars in damage.

**Figure 1.6.** A street in Montreal, Quebec, with a fallen power line post that collapsed due to the weight of ice following the freezing rain event in "The Great Ice Storm of 1998" [5].
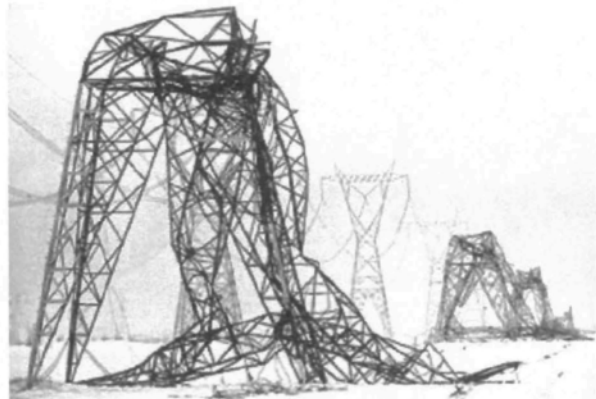


**Figure 1.7.** Giant pylons collapsed in a chain reaction like dominos following the freezing rain event of "The Great Ice Storm of 1998" [6].

***The Problem:*** A major problem in countries subjected to extreme cold weather conditions is the damage caused to the general public as well as the industrial sector following disastrous winter events such as freezing rain storms. Surfaces facing ice build-up are adversely affected and ice accumulation can result in severe damage or interrupted operation. For example ice formation and accumulation on aircraft wings endangers the plane and its passengers [7,8]. The recent crash of Continental commuter flight 3407 which claimed 50 lives is believed to be due to icing on the wings and cockpit windshields [9]. Ice on ship hulls creates navigational difficulties and the expenditure of additional power to navigate through water and ice. The need to scrape ice that forms on automobile windshields is regarded by most drivers as a bothersome and recurring chore, and any residual ice imperils visibility and safety [10]. At least 150 telecommunications towers have collapsed due to ice loads in the last 40 years [10]. The accumulation of ice on high tension power lines can lead to the mechanical failure of the cables and often results in load shedding events as is evident from the January 1998 ice storm, and the December 2008 and January 2009 storms.

Similarly, ice accretion, together with superimposed contamination, often causes a decrease in the flashover voltage of outdoor insulators, resulting in occasional outages [11]. It has been reported that in North America and Northern Europe, many power utilities have suffered network disturbances caused by the effect of ice and/or snow accumulation on insulators [12]. Insulation failures due to the ice-bridging of insulators are also reported from the USA (1970), Canada (1988), Japan (1991), Norway (1992), China (1991) and several other countries [13].

6

**Figure 1.8.** Deicing of an Air Canada flight before take-off in Montreal's Trudeau International airport [14].


*Existing solutions, their merits and demerits:* Current strategies to eliminate or reduce ice buildup such as chemical, mechanical or thermal deicing carry several disadvantages. Deicing techniques such as the use of freezing point depressants, like salt or chemical sprays, have been employed on highways [15]. Deicing fluids such as ethylene glycol and propylene glycol are used on aircraft wings and have been found to be effective [16]. Figure 1.8 shows a photograph of an Air Canada flight undergoing deicing before

take-off in Montreal. The drawback in such deicing techniques is the need to apply and maintain a sufficient quantity of deicer which is both time-consuming and expensive. Furthermore, the deicing fluids are toxic and environmentally unsafe.
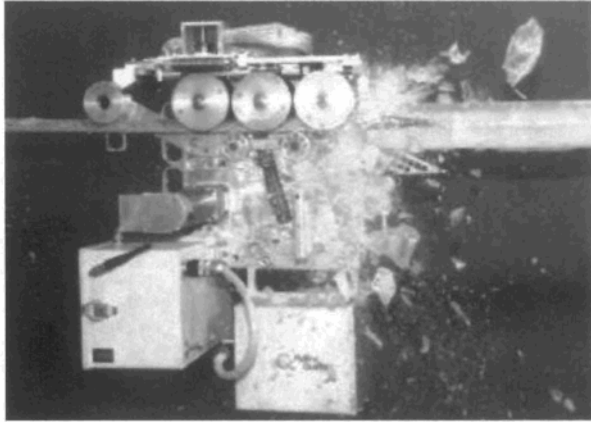


**Figure 1.9.** Deicing of an iced electric cable by a mechanical method [18].

Another commonly used de-icing method is the mechanical removal of ice from surfaces by scraping or vibrating the system vigorously [17, 18], which can cause damage to the surfaces. Figure 1.9 shows a photograph of an iced electric cable being deiced by means of mechanically crushing the ice into debris [18]. Heating the surface to melt the ice is another effective method which unfortunately requires a large supply of energy [19]. Electrolysis is one of the "smart" de-icing techniques, which is found to be effective in removing ice from metal surfaces [10]. However, none of these techniques prevents ice from forming or accumulating, rather, these techniques are used only after there is an ice build-up or accumulation. Obviously, it would be preferable to prevent the accumulation of

ice in the first place. Ice is generally accreted during periods of sub-zero temperatures by the impact of supercooled droplets of water onto the surface. A more practical and economical choice in the prevention of ice formation on surfaces at sub-zero temperatures is to apply a coating that is icephobic in nature, so that ice does not adhere to the surfaces.

## 1.2 Brief background

*Icephobicity:* The strong adhesion of ice to materials is due mainly to the properties of the ice–surface interface where polar water molecules strongly interact with the solid. Three physical processes contribute to the adhesion of ice to perfectly flat surfaces: hydrogen bonding, van der Waals forces, and direct electrostatic interactions. Ideally, all the three types of interaction must be eliminated to have zero or reduced ice adhesion. It is the electrostatic forces between charges at the ice surface and mirror charges induced in a solid substrate that have been found to largely dominate the adhesion of ice to surfaces [20,21]. The electrostatic interaction energy between ice and metals has been found to be significantly higher than the hydrogen bonding and van der Waals force at greater than intermolecular distances [20]. Charges on ice induce smaller charges on dielectrics, the reduction being related to the dielectric constant by the equation $q' = q\dfrac{\varepsilon - 1}{\varepsilon + 1}$, where $q'$ is the image charge produced by a charge $q$ on the ice surface and $\varepsilon$ is the dielectric constant of the insulator. According to the above equation, materials with a very low dielectric constant would significantly reduce the adhesion of ice by reducing the electrostatic interaction (whose force $F \propto \dfrac{qq'}{r^2}$, where $r$ is the distance between $q$ and $q'$).

Ice adhesion tests have been carried out on several surfaces with different chemical compositions. It has been observed that fluorinated and polysiloxane modified surfaces show the poorest wetting by water and the best potential as icephobic coatings [22]. Studies have also shown that aluminum surfaces rendered hydrophobic by the addition of a self assembled monolayer (SAM) of silane and fluorocarbon have reduced ice adhesion compared to the bare aluminum surface [23,24]. Theoretical predictions by Kulinich *et al.* show that the formation of SAMs with the highest possible degree of assembly can result in hydrophobic properties, and probably icephobic properties [25].

*Superhydrophobicity:* In addition to the influence of electrostatic forces on ice adhesion, the morphology and chemical composition of the solid surface play an important role, and the right combination of surface properties can dramatically lower the ability of water drops to stick [26]. In his review on "Non-sticking drops", David Quéré details the requirements for a water drop to slide on an inclined surface on the basis of the contact angle (CA, see section 2.2.1) and the contact angle hysteresis (CAH). The CAH is defined as the difference between the advancing and receding CAs of water obtained on a surface during the motion of a water drop in one direction [26]. Quéré states that a water drop can slide off a surface even if the CA is very low, say less than $20°$, provided that the CAH is less than $4-5°$, which is very difficult to achieve. On the other hand, a water drop can slide off a surface even if the CAH is higher, provided that the CA is greater than $160°$, due to the lower contact area between the liquid and the solid. Quéré concluded that "non-

sticking" drops must therefore be observed on surfaces with CA > 160° and such surfaces are termed "superhydrophobic".

Superhydrophobicity is observed on certain natural tissues such as lotus leaves. The so-called *"Lotus effect"* is due to the presence of a rough micro-nanostructure covered with waxy materials which are poorly wetting, resulting in a water contact angle greater than 150° [27]. The rough micro-nanostructure allows the entrapment of air beneath the water drop in the pores (troughs) of the rough structure and the waxy coating, which has a low surface energy, helps to reduce the interaction of the surface with water. Studies have been carried out in an attempt to understand the role of surface roughness on ice adhesion [28,29]. Learning from nature, a superhydrophobic surface can be obtained by creating an optimum surface roughness followed by passivation with a low surface energy coating leading to a very low area of contact between the solid surface and the liquid, causing a water drop to roll off the surface. As the contact area of water on a superhydrophobic solid surface is negligible, such surfaces would effectively reduce the contact area of ice as well. Therefore, ice adhesion would be significantly reduced on superhydrophobic surfaces.

A detailed background study with an expanded literature review will be provided in Chapter 2 to follow.

**1.3 Hypothesis**

Based on the above summary, it is therefore plausible that *a properly nanostructured, low dielectric constant material with an optimized surface roughness and an appropriate passivation layer will reduce the electrostatic interaction as well as the*

11

*contact area of ice with the surface, thereby inhibiting ice accumulation.* In this project, this hypothesis will be investigated by the deposition of passivated, nanostructured dielectric materials with different dielectric constants on insulator substrates, with a view to ultimately preventing ice accumulation on the insulators of high-tension lines.

## 1.4 Objectives

The context of the project being the prevention of ice formation and the elimination of ice accumulation on the insulators of high-tension lines, the main objectives of this research project are as follows:

1. Synthesize nanostructured dielectric oxide thin films with low and high dielectric constants and investigate the role of the dielectric constant in icephobicity,

2. Passivate the nanostructured dielectrics by chemical and plasma modifications to obtain a low surface energy,

3. Characterize these films by surface morphological and compositional studies, and,

4. Test for superhydrophobicity and icephobicity.

## 1.5 Methodology

The major procedures of this research work consist of the following steps:

1. *Creating nanopatterns on the desired substrates:* Nanopatterns are created on the substrates of aluminum (Al) by chemical etching, a method where the Al substrates are immersed in an etchant solution of HCl of a suitable dilution for a certain period

of time resulting in the partial removal of material from the surface creating a random pattern on the substrate.

2. *Coating with the desired dielectrics:* The dielectric coatings of ZnO or $TiO_2$ are applied on the chemically etched, nano-rough substrates of Al by a sol-gel spin-coating technique. An aged sol of ZnO or $TiO_2$ is deposited on the substrates using a spin-coater, followed by drying and annealing processes resulting in nanorough dielectric surfaces.

3. *Passivating the nanorough dielectrics:* The nanorough dielectrics are passivated using two different techniques. In the first method, the nanorough dielectric samples are immersed in a solution of fluoro-alkyl silane (FAS-17) for a certain time to lower the surface energy via a monolayer coating of FAS-17 on the surface with fluorinated carbon terminal groups oriented away from the surface. In the second method, a target of Teflon® is rf-sputtered onto the dielectric surfaces using a plasma reactor resulting in a lower surface energy.

4. *Characterizing the passivated and unpassivated nanorough dielectrics:* The passivated as well as unpassivated nanorough dielectric surfaces are characterized in terms of the surface morphology, surface composition, superhydrophobicity and icephobicity. Surface morphology studies are performed using optical microscopy, field emission scanning electron microscopy (FESEM), and atomic force microscopy (AFM). The surface compositional analyses are carried out using X-ray photoelectron spectroscopy (XPS) and Fourier-transform infrared spectrometry (FTIR). Superhydrophobicity tests are performed using a contact angle goniometer

13

and the icephobicity tests are performed using in-house test methods, namely, pulling tests and centrifugal adhesion reduction tests (CAT).

The detailed description of the experimental procedures is provided in Chapter 3.The remainder of the thesis is structured as follows:

(i)     Chapter 2 will provide a background study and literature review on superhydrophobicity and icephobicity.

(ii)    Chapter 3 will detail the experimental methods used.

(iii)   Chapter 4 will provide a discussion of preliminary trials with superhydrophobic ZnO nanotowers formed using a chemical bath deposition (CBD) technique.

(iv)    Chapter 5 will detail the major contribution of the thesis to the goal of obtaining superhydrophobic dielectric surfaces of ZnO and $TiO_2$ by a combination of substrate chemical etching and sol-gel spin-coating techniques. The chapter will also include a discussion of the surface characterizations such as morphological and chemical analyses as well as superhydrophobicity tests.

(v)     Chapter 6 will provide a detailed discussion of the ice adhesion test results obtained on the nanorough dielectric surfaces of ZnO and $TiO_2$. The chapter will also describe the effect of ice detachment from the dielectric surfaces by means of surface morphological and chemical analyses as well as superhydrophobicity tests after ice detachment.

(vi)    Chapter 7 will provide the overall conclusion to the thesis, although each contributing chapter mentioned above will have its own conclusion.

(vii)    Chapter 8 will provide recommendations for future work in the field and suggest

methods to accomplish the recommended work where appropriate.

# CHAPTER 2

# BACKGROUND AND LITERATURE

The available literature on icephobicity and superhydrophobicity will be reviewed in the following sections of this chapter.

## 2.1 Icephobicity

Icing on various structures, as previously introduced in Chapter 1, is a serious and significant problem posing safety issues and system operation problems. Examples of the most important structures exposed to ice and causing a threat to safety are hydroelectric power lines, high-tension insulators, wind turbines, aircraft, the space shuttle, ship hulls, off-shore ocean structures, highways, runways, automobile wind-shields and domestic structures such as roofs and windows. It is well known that ice bonds strongly to almost all surfaces making its removal difficult and creating the absolute necessity of a technological solution to aid in the debonding of ice. However, current de-icing techniques, as mentioned in Chapter 1 and to be discussed in detail later in the present chapter, are highly demanding of energy, destructive to surfaces and hazardous to health as well in the case of the use of certain chemicals. Therefore, making a surface where ice would not stick at all, would be an ideal and economical solution to eliminate the use of complex de-icing techniques. Such a surface on which ice would not adhere would be termed an "icephobic" surface. An

icephobic surface may be achieved by the use of a coating whose chemical components will have a weak chemical interaction with ice (whose chemical properties are similar to those of water) in combination with a surface morphological modification. The advantage of developing an icephobic surface treatment is that it can be made to be environmentally friendly and may be easily applied to various structures.

Although the main objective of the research described in this dissertation is to prevent ice formation on high-tension insulator surfaces, the methodology employed in the research is flexible and may be applied to other surfaces with appropriate materials chosen.

A theoretical background on ice types and ice adhesion principles is presented in the following section along with a literature review. It must be noted that the literature in the field of ice adhesion is sparse and an effort has been made to provide a review based on the few important literature sources available.

### 2.1.1 Theoretical background

"Ice" is a mysterious substance that has not really been well explored. Before going into a detailed discussion of ice, let us think for a moment about a beautiful, peaceful snow fall. One might have noticed that the snowflakes that reach the ground exist in various extremely beautiful shapes and sizes (Figure 2.1). Petrenko and Whitworth have detailed the types of ice formed in different icing conditions in their book on "The Physics of Ice" [21]. Some common types of atmospheric ice encountered in everyday winter life and in weather reports include ice sleets, glaze ice, rime and frost. Glaze ice on exposed surfaces is considered to be the most troublesome compared to other forms of ice. Why? The

following discussion about these common ice types may help us understand some of the concepts.
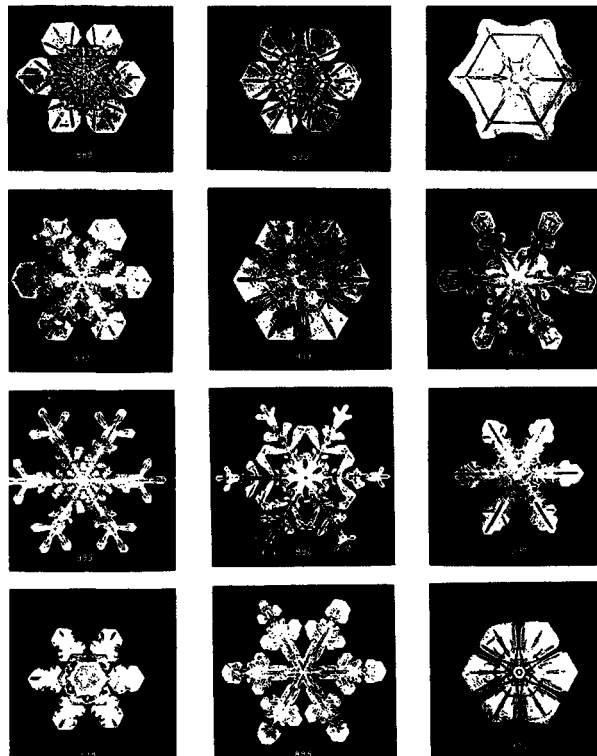


**Figure 2.1** Snow flakes in amazingly various shapes and sizes [30].

Snow begins to form in the atmosphere as water condenses into tiny droplets growing as more and more water vapor condenses on to its surface. Cold air then freezes this water into an ice crystal. Each ice crystal has a unique shape that depends on the surrounding air's temperature and water vapor content. During their fall from the sky, these crystals undergo phases of cold and warm air before they hit the ground. The snow stays or

18

melts on the ground depending on the temperature on the surface. Glaciers that form on mountains, for example, are made up of snow that accumulates on the ground and eventually turns to ice. Snow, therefore, is in fact a form of ice and it is interesting to realize that ice can exist in many different forms.

### 2.1.1.1 Types of atmospheric ice

Atmospheric ice can be categorized into two main types depending on the icing conditions, namely, in-cloud icing and precipitation icing [31,32].

*In-cloud icing*, as the name implies, occurs in clouds, describing a process in which supercooled liquid droplets collide with surface structures and instantaneously freeze onto the structure. In-cloud icing is known to accumulate thick layers of ice [33]. Structures located at higher altitudes above sea-level such as telecommunications towers, power transmission lines going through mountains, aircraft, etc., face in-cloud icing, which may be of the form glaze, hard rime or soft rime depending on the icing conditions in the cloud. McComber *et al.* reported the hazardous nature of in-cloud icing on power transmission lines going through the mountains in northern Quebec, where clouds are frequently found above an altitude of 300 m (984 ft) [34].

*Precipitation icing* may occur at any altitude. Precipitation icing occurs when either snow or rain freezes after striking the surface [35]. Wet snow can stick to a surface if the temperature is between 0 and 3 °C, conditions in which snow contains some liquid water allowing the snow crystals to bind together when they come into contact on the surface. If the temperature subsequently falls below 0 °C, the binding strength of wet snow can

become very high. On the other hand, icing can occur from a rainfall at temperatures below 0 °C. This often occurs in connection with a temperature inversion where cold air is trapped near the ground beneath a layer of warmer air. Precipitation icing also occurs in the form of glaze or rime.
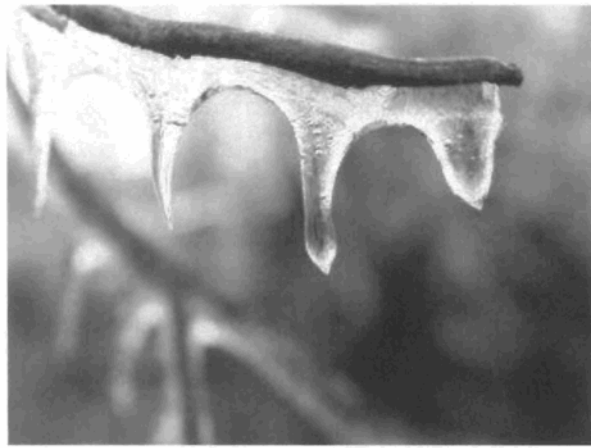


**Figure 2.2.** Example of glaze ice formed on a branch [36].

*Glaze ice:* When rain droplets or drizzle fall into a layer with cold air at a temperature below freezing the drops become supercooled [37]. They are still in the liquid (water) phase and do not freeze before they hit the ground or an object. The resulting accretion is a clear and solid ice called glaze as shown in Figure 2.2 (as well as in Figure 1.1 of Chapter 1). Glaze freezes slowly allowing the supercooled water to flow around objects before freezing is completed, mechanically interlocking the ice to objects.

Glaze ice has a high density of ~0.9 g.cm$^{-3}$ and the accretion is hard and strong and, therefore, difficult to remove [38].
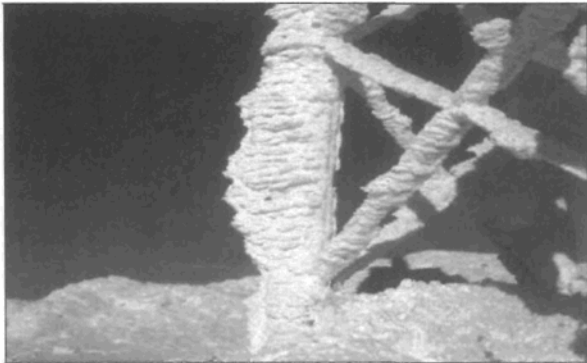


**Figure 2.3.** Rime ice, more than a meter thick, formed on towers [38].

*Rime ice:* The rapid freezing of supercooled droplets on surfaces leads to the accretion of rime ice (Figure 2.3). Supercooled fog, sea smoke and cloud droplets which are of sufficiently small size are some sources of rime ice formation [38]. Rime ice is typically relatively weak in strength and brittle in nature. Depending on the density, rime ice can be categorized into two types: soft rime and hard rime. Soft rime is lower in density due to larger air gaps between the frozen particles [35]. The density is typically between 0.2 and 0.6 g/cm$^3$ [38]. Hard rime is higher in density, between 0.7 and 0.9 g/cm$^3$ and closer to that of glaze [38]. It is harder largely due to better bonding and smaller air gaps between the frozen particles [35].

### 2.1.1.2 The physics of ice

It has been mentioned in Chapter 1 that the existing anti-icing or de-icing methods used in preventing ice formation or removing already formed ice have their drawbacks from an economical and environmental view point. Therefore, an icephobic surface, which could be accomplished by a coating and a surface morphological modification is proposed to be an ideal and economical solution in the prevention of ice accumulation. However, an understanding of the fundamental mechanisms involved in the adhesion of ice with a solid surface would be an important aspect. The physical processes involved in ice adhesion can be attributed to three different kinds of forces: chemical bonding, Lifshitz-van der Waals forces, and electrostatic forces [20,21,35]. Chemical bonding, namely hydrogen bonding, acts between molecules on opposite sides of the interface over distances of the order of 0.1-0.2 nm. At perfect contact of ice with the solid surface, the hydrogen bond interaction energy could be $\geq 0.5\ Jm^{-2}$ as reported by Ryzhkin and Petrenko [20]. Van der Waals forces are of longer range than hydrogen bonding and are always present at the interface. Van der Waals forces are the weakest intermolecular attractions and their interaction energy as mentioned by Petrenko and Qi is $26.9\ mJm^{-2}$ as determined in case of a specific polymer surface [10]. Electrostatic interactions occur between non-compensated spatial distributions of charge on opposite sides of the interface at greater than intermolecular distances and contribute significantly to ice adhesion with an interaction energy of up to $500\ mJm^{-2}$ [20].

So the electrostatic forces of attraction between charges on ice and induced image charges are considered to play a significant role in ice adhesion, although the fundamental physics of ice adhesion is yet to be fully explored. However, it is a well-known fact that ice

adheres to any surface. Exerting an external force on the ice-solid interface can lead to cohesive rupture (breaks that happen within the ice) or adhesive rupture (breaks that happen at the ice-solid interface and occur when the strength of adhesion is lower than the strength of ice) [35]. The strength of adhesion between two materials can be defined in terms of $W_A$, the work of adhesion, which is the free energy required to separate a boundary of unit area between the media and it is given by

$$W_A = \gamma_1 + \gamma_2 - \gamma_{12} \qquad (2.1)$$

where $\gamma_1$, $\gamma_2$, $\gamma_{12}$ are the surface free energies per unit area of medium 1, medium 2, and the interface respectively.

For a solid- liquid interface, $W_A$ can be written as

$$W_A = \gamma_{SV} + \gamma_{LV} - \gamma_{SL} \qquad (2.2)$$

where $\gamma_{SV}$, $\gamma_{LV}$, $\gamma_{SL}$ are the surface free energies of the solid-vapor interface, liquid-vapor interface and solid-liquid interface respectively.

The work of adhesion for liquid–solid interfaces can also be described as a function of the angle of contact, $\theta$, of the liquid with the solid surface and the surface free energy between the liquid and vapour phases, $\gamma_{LV}$ as:

$$W_A = \gamma_{LV}(1 + \cos\theta) \qquad (2.3)$$

Equation (2.3) shows that the work of adhesion is a minimum when contact angle is a maximum and vice versa. Since the binding energies of $H_2O$ molecules and different solids are expected to be similar in ice and water, it may be supposed that the values of $W_A$ on

different ice-solid interfaces will be a function of the wetting of water on these solids. A

detailed review on wetting is provided in Section 2.2 of this chapter.


## 2.1.2 A literature review on icephobic surfaces

There are so far no reports claiming the existence of an icephobic surface on which

ice would not stick at all. However, efforts have been made by researchers in the field to

reduce the adhesion of ice to surfaces to lead to easy de-icing.
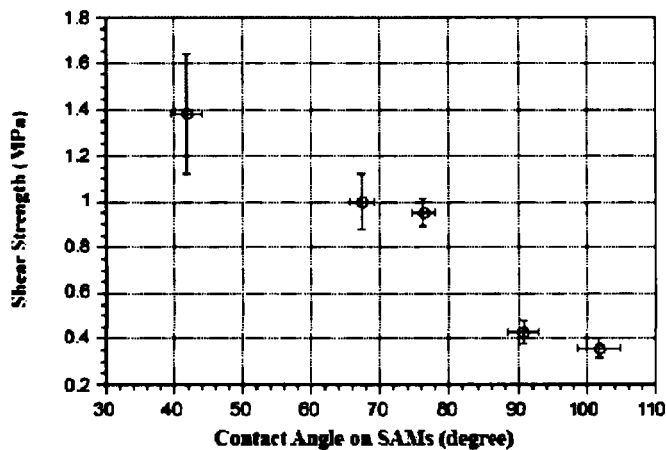


**Figure 2.4.** Dependence of the shear strength of ice on the water contact angle [39].


Petrenko and Peng collected measurements of the shear strength of ice adhered to

hydrophilic and hydrophobic self-assembled monolayers (SAM) on gold surfaces [39].

Obviously a hydrophobic SAM is expected to demonstrate a higher contact angle than a

hydrophilic SAM. Petrenko and Peng showed in their measurements that the shear strength

24

of ice decreased with an increase in the contact angle of water (Figure 2.4). Their report shows the promise of a considerable reduction in ice adhesion strength by producing surfaces with a very high contact angle of water.

A hydrophobic SAM is formed when molecules spontaneously adsorb in a monomolecular layer on a surface with their hydrophilic tail group bonding with the substrate and their low surface energy hydrophobic head group pointing outward from the surface. Solmo and Gupta studied the effect of various SAMs, namely, polyimide (PI), polymethylmethacrylate (PMMA) and dimethyl-$n$-octadecilchlorosilane (DMOCS), on 6061 Al surfaces on the tensile strength of ice adhesion and compared their results with that obtained on bare Al [23]. They showed that SAM treated Al surfaces showed reduced ice adhesion as compared to the bare Al surfaces. A summary of their results is provided in Table 2.1. Their results emphasize the importance of lowering the surface energy in reducing ice adhesion to surfaces.

**Table 2.1.** Tensile strength of ice adhesion on SAM treated and untreated Al surfaces.

| Al samples | Adhesion strength (MPa) |
|---|---|
| Bare Al (mechanically polished) | 274 |
| PI/Al | 177 |
| PMMA/Al (Hydrophilic) | 190 |
| DMOCS/Al (Hydrophobic) | 131 |

The results of NASA LEWIS and BF Goodrich studies indicate that hydrophilic materials have substantial ice-adhesive properties [40]. Other research performed on a group of thermoplastics and coatings to reduce ice accretion reported a maximum reduction in ice accretion with Teflon® in comparison with other candidates indicating the importance of a low surface energy [41]. Recently, a hydrophobic coating obtained from a mixture of Rain-X and MP55 PTFE (powder Teflon®) has also been reported to reduce ice adhesion to the surfaces of space shuttle components [42]. Surface roughness, one of the important factors in enhancing the water contact angle on surfaces, has also been investigated by researchers for its role in ice adhesion [28]. However, as reported by Saito *et al.*, an increase in surface roughness led to an increase in ice adhesion [29]. Recent studies show that a combination of surface roughness and a low surface energy coating leads to very high water contact angles and enhances a reduction in the adhesion strength of ice [43,44]. A recent dissertation submitted by A. Safaee titled "Nanostructured metal surfaces and their passivation for superhydrophobic and anti-icing applications", UQAC 2008, also shows superhydrophobic surfaces as promising candidates for reducing ice adhesion [45]. Therefore, surfaces which repel water have a substantial potential for the elimination of ice adhesion problems as on such surfaces, the contact area of water drops is negligible. A background and literature review on superhydrophobicity follows in the next section.

## 2.2 Superhydrophobicity

**2.2.1 Theoretical background:** Superhydrophobicity being a pre-requisite in going towards icephobicity, a knowledge of the water-solid interface would be important in understanding the ice-solid interface.

Wettability is one of the most important properties of a solid surface. Many practical applications depend on the wetting or non-wetting characteristics of the solid surface. When a water drop comes in contact with a surface, the surface is either wet or not wet depending on the hydrophilicity or hydrophobicity of the surface, respectively. The degree of wetting is characterized by the angle of contact the water drop makes with the surface which is the angle at which the liquid-vapor (LV) interface meets the solid-liquid (SL) interface and the solid-vapor (SV) interface (Figure 2.5).

If the surface is hydrophilic, the water drop is strongly attracted to the surface and will spread on the surface providing a contact angle close to $0°$. Less strongly hydrophilic surfaces can have a contact angle up to $90°$. If the surface is hydrophobic, the interaction forces between the water drop and the solid are weaker and the water drop will have a tendency to form a compact droplet on the surface. The contact angle on such surfaces is usually greater than $90°$. The contact angle, therefore, is determined by the strength of the interfacial forces between the water drop and the solid surface. These interfacial forces are sometimes denoted as interfacial tensions or interfacial free surface energies. The Young equation (equation 2.4) deduced in 1805 by Young describes the connection between the surface free energies of the solid-liquid ($\gamma_{SL}$), solid-vapor ($\gamma_{SV}$) and liquid-vapor ($\gamma_{LV}$)

27

interfaces and the contact angle $\theta$ between the tangent drawn to the spherical surface of the water drop from any point on the boundary where all the three phases meet [46].

$$\cos\theta = \frac{\gamma_{SV} - \gamma_{SL}}{\gamma_{LV}} \qquad (2.4)$$

Figure 2.5 shows a schematic of a liquid drop resting on a solid surface with the various parameters governing the contact angle $\theta$ of the liquid drop. The Young equation is a result of the thermodynamic equilibrium of the three interfaces. Depending on the value of the contact angle of a water drop with a surface, the surface is categorized as hydrophilic ($\theta < 90°$), hydrophobic ($\theta > 90°$) or superhydrophobic ($\theta > 150°$). These values are static contact angles which are obtained by sessile drop measurements using a goniometer in which a water drop is deposited on the surface.
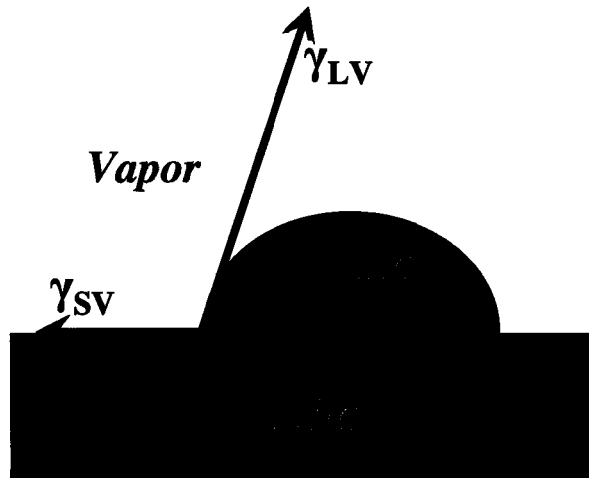


**Figure 2.5.** Interfacial forces acting on a water-drop in contact with a solid surface and its contact angle with the solid surface.

28

Another method used in characterizing the wetting characteristics is to measure the dynamic contact angle in which a water drop is allowed to advance in one direction as shown in Figure 2.6 and the difference between the advancing contact angle $\theta_A$ and the receding contact angle $\theta_R$ is measured. This parameter is called the contact angle hysteresis (CAH). The CAH value can reveal the ability of a water drop to stick or slide on a surface. On a surface with a very low CAH, the water drop would roll off easily with a slight tilt of the surface and on a surface with a high CAH, the water drop would stick to the surface.
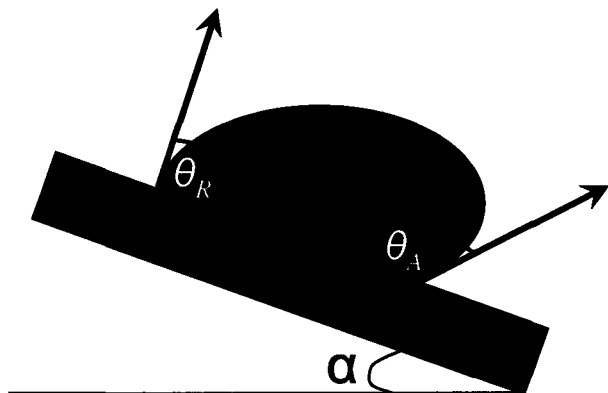


**Figure 2.6.** Contact angle hysteresis ($\theta_A$ - $\theta_R$) on an inclined surface at an inclination angle of $\alpha$

Superhydrophobic surface treatments of various substrates have proved to be of great interest in recent years [47]. To reach extreme values of the contact angle, greater than 150°, surface roughness is often added to amplify the hydrophobicity of the coating

materials. These contact angles are sometimes addressed in the literature as apparent contact angles as the contact angle obtained does not represent the real contact angle on the corresponding flat surface. The surface topography effects have been mathematically described by the Wenzel model (Figure 2.7) and the Cassie-Baxter model (Figure 2.8) [48,49].

In Wenzel model [48], the water drop penetrates the surface irregularities as shown in Figure 2.7. Mathematically, Wenzel equation is written as

$$\cos \theta' = R_w \cos \theta \qquad (2.5)$$

where the roughness factor $R_w$ is the ratio of the true and apparent (geometric) surface areas. According to the Wenzel model, when the true contact angle $\theta$ of water on a smooth surface is less than $90°$, the apparent contact angle $\theta'$ is less than the true contact angle $\theta$ on a rough surface, and when the true contact angle $\theta$ is greater than $90°$, the apparent contact angle $\theta'$ is greater than the true contact angle $\theta$ on a rough surface. It has been shown that the contact angle and the contact angle hysteresis increase as the roughness factor increases [50]. However, it has also been demonstrated that the contact angle continues to increase when the roughness factor exceeds a certain level ($\sim 1.7$), whereas the hysteresis starts to decrease [50]. This decrease in the CAH is attributed to a transition from the Wenzel regime to the Cassie-Baxter regime where the water drop does not penetrate the surface irregularities; rather, it stays suspended on the tips of the rough crests due to the entrapment of air pockets in those crests (Figure 2.8).
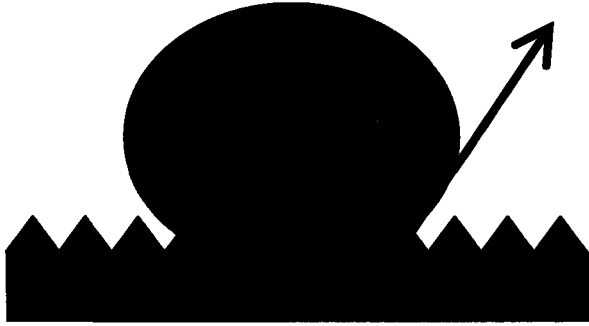
**Figure 2.7.** Schematic of the Wenzel model

The Cassie-Baxter model [49] describes the effect of roughness on chemically heterogeneous structures where the apparent contact angle is mathematically derived from the Cassie equation as follows:

$$\cos\theta' = f_1 \cos\theta_1 + f_2 \cos\theta_2 \qquad (2.6)$$

where $\theta'$ is the apparent contact angle of the composite coating consisting of two components with contact angles $\theta_1$ and $\theta_2$ and corresponding area fractions $f_1$ and $f_2$. In such a composite system $f_1$ is assumed to be the solid surface and $f_2$ is assumed to be air where $\theta_2$ is 180° and as $f_1 + f_2 = 1$, Equation (2.6) can be written as

$$\cos\theta' = f_1(\cos\theta_1 + 1) - 1 \qquad (2.7)$$

This equation explains that on a rough surface with large amount of air entrapment in the surface irregularities, one can achieve a highly superhydrophobic surface with a very small

area fraction $f_1$ of the surface in contact with the water drop. The configuration leads to a very high contact angle and a very low contact angle hysteresis leading to the rolling-off of water drops on the contacting solid.

The water drops with reduced contact area with the solid are termed "non-stick" drops. David Quéré deduced a condition for a drop of radius 0.5 mm to stick or slide by relating the CA and CAH on a surface inclined at an angle $\alpha = 90^o$ (Figure 2.9) [26].

$$\pi d \gamma \left( \cos \theta_R - \cos \theta_A \right) \geq \rho g \Omega \sin \alpha \qquad (2.8)$$

Here $\pi d$ is the contact line where all three interfaces meet; $\theta_R$ and $\theta_A$ are the receding and advancing contact angles, respectively; $\rho$, the density of drop; $g$, the gravitational acceleration; $\Omega$, the volume of drop; and $\alpha$ is the angle of inclination of the surface.
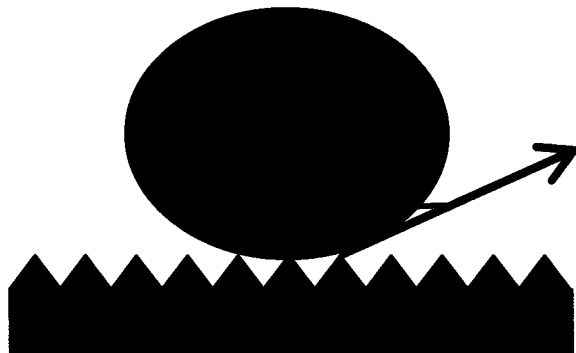


**Figure 2.8.** Schematic of the Cassie model

Equation 2.8 provides the condition for a drop to remain stuck on the surface, i.e. a condition for which the adhesion forces between the drop and the surface are greater than the gravitational force tending to make the drop slide. It is obvious, however, from the Equation 2.8 that for a negligibly small CAH ($<4 - 5^{\circ}$), the condition expressed can never be satisfied and the drop will slide.

The author plotted the contact angle hysteresis against the contact angle using Equation (2.8) and showed theoretically that non-stick drops may be achieved even with contact angles as low as $<20^{\circ}$ provided that the CAH is very low ($<5^{\circ}$). However, such an ideal surface is practically difficult to achieve. The author also showed that water drops must slide on a surface if the contact angle is greater than $160^{\circ}$ even if the CAH is higher due to the lower contact area between the water drop and the solid. It can be seen from the Figure 3.5 that the ideal conditions to obtain a superhydrophobic surface with non-stick water drops would be to obtain a contact angle of $>160^{\circ}$ as well as a CAH $<10^{\circ}$.
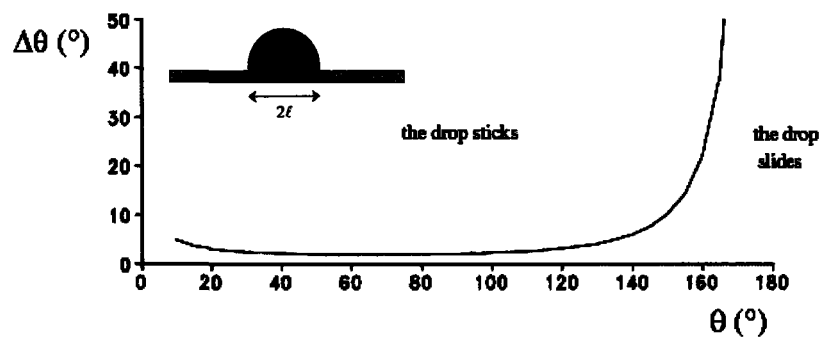


**Figure 2.9.** Relation between CA and CAH for non-stick drops [26].

**2.2.2 A literature review on superhydrophobic surfaces**

Superhydrophobic surfaces have attracted a lot of interest both in academia and industry due to their non-wetting and self-cleaning properties. To date, a literature search in "web of science" alone provides a list of 342 articles on superhydrophobicity written in the last decade.

**2.2.2.1 Superhydrophobicity in nature:** Nature's wonder inspires not only poetry, but also science, in an attempt to learn more about the world and the way it works [51]. Technology is frequently the application of science, which is in turn inspired by nature. The technology used by many researchers in making superhydrophobic surfaces is one such example. Numerous plant surfaces and body parts of certain insects and animals exhibit superhydrophobic properties, evolved to survive many of nature's hazards by repelling dirt and dust particles in rain or snow. To start with, the leaves of the sacred Lotus, scientific name Nelumbo nucifera, have this inherent property of water repellency due to which water drops roll off their surfaces, carrying away dirt and leaving the surfaces of the leaves clean [27]. This property is also referred to as self-cleaning and the "Lotus effect". Barthlott and Neinhuis showed in their study that the key element in this water-repellency is the presence of hydrophobic surface components (epicuticular wax crystalloids) on the microscopically rough structure of the leaf's surface [27]. Gould reports that each leaf surface is covered with tiny bumps, 5-10 μm high and about 10-15 μm apart [52]. This uneven surface is itself covered with waxy, hydrophobic crystals, measuring around 1 nm in diameter [52].
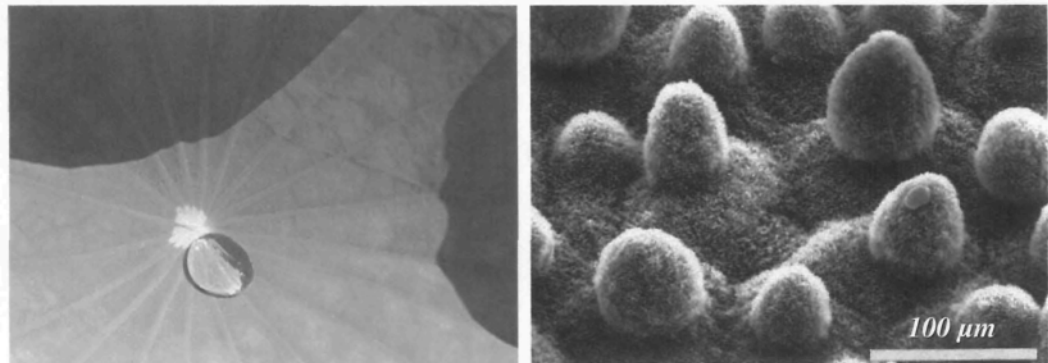
**Figure 2.10.** (Left) Photograph of a floating non-stick water drop seen on the surface of a lotus leaf [53], (Right) SEM image of lotus leaf surface [27].

Bathlott and Neinhuis reported a water contact angle of $160.4 \pm 0.7^{\circ}$ on the surface of the lotus leaves [27]. Figure 2.10 (left) shows a photograph of a spherical water drop on the surface of a lotus leaf and Figure 2.10 (right) shows the SEM image of the leaf's surface microstructure.

Among plant leaves, there exist many other examples which exhibit the Lotus-effect [54]. Feng *et al.* [54], showed that the water contact angle on the surfaces of rice leaves, taro leaves and India Canna leaves are respectively $157 \pm 2^{\circ}$, $159 \pm 2^{\circ}$ and $165 \pm 2^{\circ}$. An example of a rice leaf with water drop on its surface and the corresponding microstructure of the rice leaf are shown in Figure 2.11.
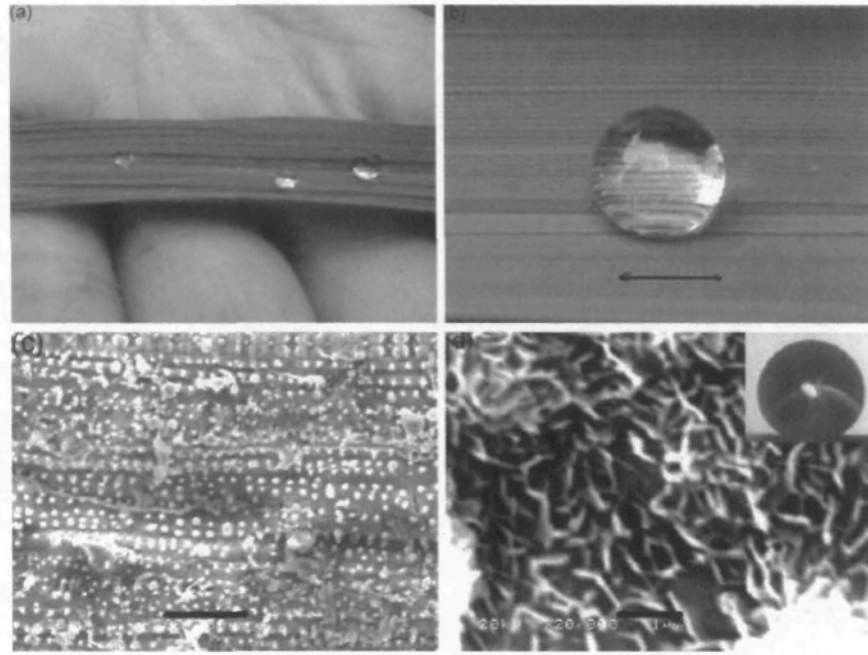
**Figure 2.11.** Photographs of (a) a few of water droplets on a rice leaf, (b) a water droplet floating on a rice leaf, (c and d) SEM images of a rice leaf with different magnifications. The scale bars of (c and d) are 50 and 1 μm, respectively [54].

Certain leaves' surfaces also have been shown to demonstrate the Lotus-effect on both the frontal and rear faces. For example, purple setcreasea and perfoliate knotweed leaves showed water contact angles of $167 \pm 2^{\circ}$ and $165 \pm 2^{\circ}$ on the frontal and rear face, respectively [54]. In all these cases, Feng *et al*. state that a rough microstructure and a hydrophobic compound on the surface are the reasons for the water-repellency [54].

Nature also produces this remarkable property on the surfaces of certain insect parts. A popular example is the water strider's legs. Water striders effortlessly walk and stand on the surface of water showing that that their legs are strikingly water repellent. According to Gao and Jiang [55], the ability of the insect to stand or walk easily on the water's surface is due to the legs' special hierarchical structure which is covered with a large number of oriented tiny hairs (microsetae) and fine nanogrooves coated with waxy materials as shown in Figure 2.12.
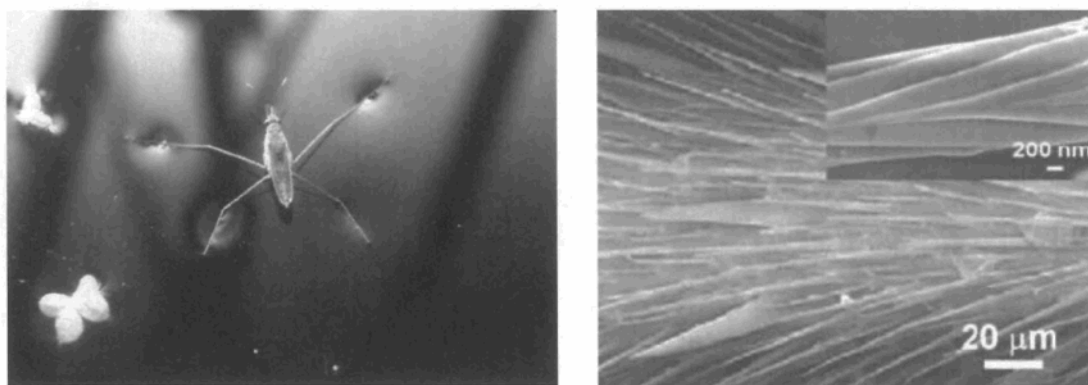


**Figure 2.12** (Left). Water strider standing on the surface of water, (Right) Microstructure of a water strider's leg showing the special hierarchical arrangement of large numbers of oriented tiny hairs (microsetae) with fine nanogrooves coated with waxy materials [55].

Research on butterfly wings indicates that water droplets easily roll off their surfaces (Figure 2.13), a special ability resulting from the direction-dependent arrangement of flexible nano-patterns on ridging nano-stripes and overlapping micro-scales on the wings as seen in Figure 2.13, where two distinct contact modes of a droplet with the orientation-

tunable microstructures occur and thus produce different adhesion forces [56]. Zheng *et al.* measured a water contact angle of $152 \pm 1.7^\circ$ on the surfaces of the butterfly wings [56].

Superhydrophobicity in nature is not restricted to the examples mentioned above and many more natural candidates demonstrate this property. However, a few important examples have been reviewed to emphasize the importance to water repellency of the rough microstructure and the presence of a hydrophobic coating on the various surfaces.
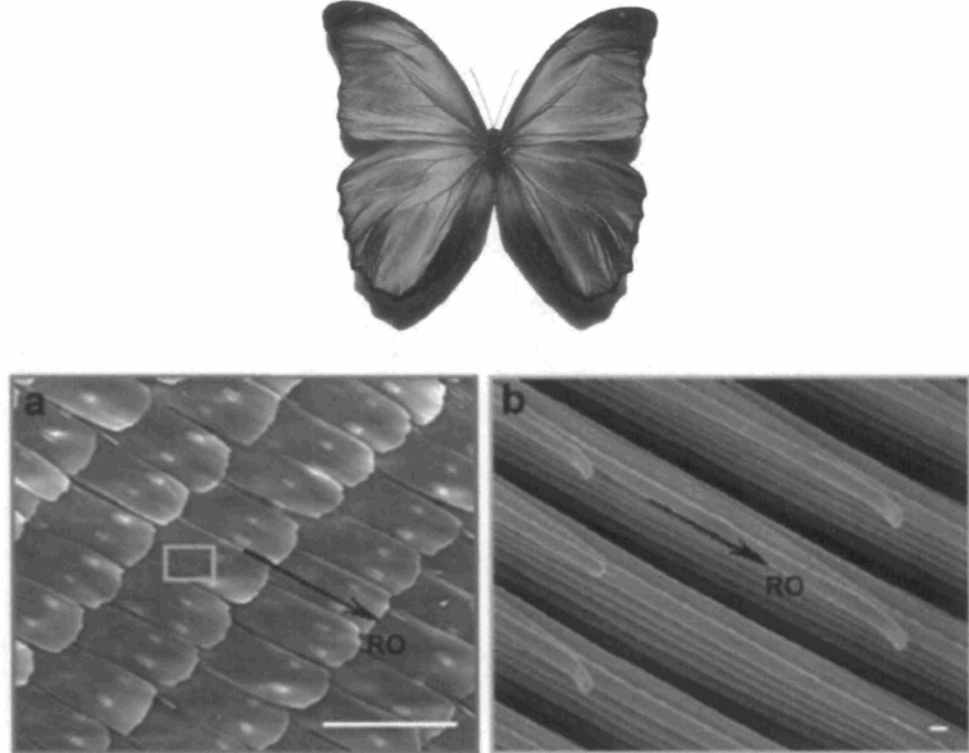


**Figure 2.13.** (Top) An iridescent blue butterfly *M. aega* [57], (Bottom) Hierarchical micro- and nanostructures on the surface of the wings. (a and b) SEM images of the periodic arrangement of overlapping micro-scales on the wings and fine lamella-stacking nano-stripes on the scales. Scale bars: (a) 100 μm; (b) 100 nm [56].

**2.2.2.2 Mimicked superhydrophobic surfaces:** Due to the tremendous importance of superhydrophobic surfaces in today's emerging technologies, many efforts have been made to replicate nature. The term "bio-mimicking" is commonly used to denote the artificial production of superhydrophobic surfaces as the technology to make them involves copying nature's solutions. The applications of superhydrophobic surfaces are diverse due to their unique water-repellency and self-cleaning abilities. The most common areas where superhydrophobic surfaces attract attention include antibiofouling paints for boats [58] , bio-chips [59], biomedical applications [60], microfuidics [61], corrosion resistance [62], eyeglasses, self-cleaning windshields for automobiles [26], stain resistant textiles [63], antisticking of snow for antennas and windows [64], expected inhibition of adherence of snow, oxidation, current conduction [65] and many others.

A literature survey on the various attempts to make a superhydrophobic surface has shown that the methods can be basically divided into two categories: (i) a one-step approach in which a low surface energy material is roughened, and (ii) a two-step procedure in which a surface is first roughened and then modified chemically or physically to lower the surface energy [66-69]. Both the approaches, however, emphasize the importance of the combination of roughness and low surface energy. Details from a recent review of the most common methods in achieving superhydrophobicity on various surfaces are provided in the following paragraphs. However, the field is vast and the methods reviewed here may not constitute an exhaustive list.

**(i) One step procedures**: As mentioned above, the approach involves simply roughening a low surface energy material. Onda *et al.* obtained an enhanced contact angle as large as

~174° by via a procedure of "wax solidification" [70]. In their procedure, a glass plate is dipped into melted wax-like alkylketene dimer (AKD) at a temperature of 90 °C and subsequently cooled to room temperature to solidify the coating, during which the AKD undergoes fractal growth as shown by the SEM image in Figure 2.14. The CA of water on a flat AKD surface is 109°.
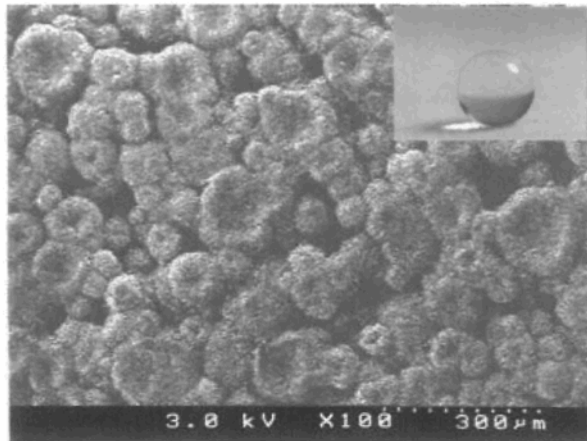


**Figure 2.14.** SEM images of the fractal AKD surface with inset showing a water droplet on an AKD surface with $\theta = 174°$ [70].

Another similar example in which the low surface energy material is allowed to roughen during deposition has been reported by Singh *et al.* [71]. The surface is formed via an electrospinning technique in which a highly fluorinated polymer "poly[bis(2,2,2-trifluoroethoxy)phosphazene]" mixed in tetrahydrofuran, methylethyl ketone, and acetone is electrospun on to a substrate. The highest CA those authors achieved was ~159° with a

40

very low CAH of <4°. Recently, Menini *et al.* reported a variation of the contact angle with the viscosity of polymer solutions of polystyrene since the morphology and hence the roughness on the polystyrene nanofibres produced in their process vary with viscosity [72]. Shiu *et al.* treated a Teflon® film, a well known commercial low surface energy material, with an oxygen plasma and obtained a rough surface which provided a CA of 168° [73]. Similarly, Minko *et al.* have reported the plasma treatment of PTFE for the fabrication of self-adaptive surfaces [74]. Oxygen plasma etched PTFE showed a water CA of about 160°. Zhang *et al.* reported a simple and effective way to achieve a superhydrophobic film by stretching a poly (tetrafluoroethylene) (Teflon®) film. The extended film consisted of fibrous crystals with a large fraction of void space in the surface which was believed responsible for the superhydrophobicity [75]. A few other examples of achieving superhydrophobicity by roughening low surface energy materials have been summarized by Mei *et al.* [68], Zhang *et al.* [67], and Ma *et al.* [66]. Figure 2.15 shows SEM images of other examples of low surface energy materials roughened in order to obtain superhydrophobicity.

**(ii) Two step processes:** In this procedure, a rough pattern is first created on a substrate and the final rough substrate is modified with a low surface energy material by chemical or physical methods in order to obtain superhydrophobicity.

Methods to produce a thin film with a certain roughness or to create a certain roughness on a substrate may result in either ordered or random surface morphological features depending on the method used. Superhydrophobicity has been achieved on both ordered as

41

well as randomly patterned surfaces following passivation, a term used for the process by which the surface energy is lowered via surface modification.
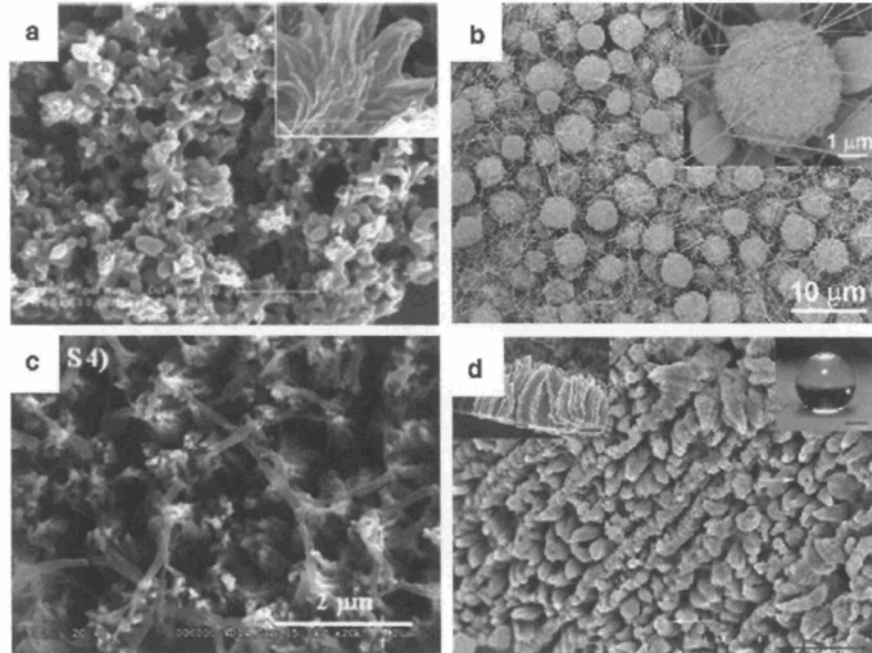


**Figure 2.15.** SEM images of superhydrophobic surfaces created by roughening organic materials. (a) Floral-like crystal structures of PE; (b) PS surface made by electrostatic spinning and spraying; (c) aligned PS nanofibers replicated from nanoporous anodic aluminum oxide and (d) double-roughened poly(alkylpyrrole) film made by electrochemical polymerization; scale bar: 15 µm [66].

Several methods such as lithography [76] (photolithography [77], electron beam lithography [78], nanosphere lithography [79], soft lithography [80] etc.), etching [81], particle aggregation [82], sol-gel processes combined with spin coating or dip-coating

[83,84], electrochemical deposition [85], galvanic exchange reaction or electroless deposition [86], hydrothermal [87], wet chemical routes such as chemical bath deposition [88], etc., exist which use a two-step process in obtaining superhydrophobic surfaces [66-68,76].

*Lithographic techniques* such as photolithography, soft lithography, nanosphere lithography, nanoimprint lithography etc., are used to generate superhydrophobic surfaces where the shape of the features and the pattern is well defined. That is, the surfaces treated by lithographic techniques produce a well-ordered microstructure.
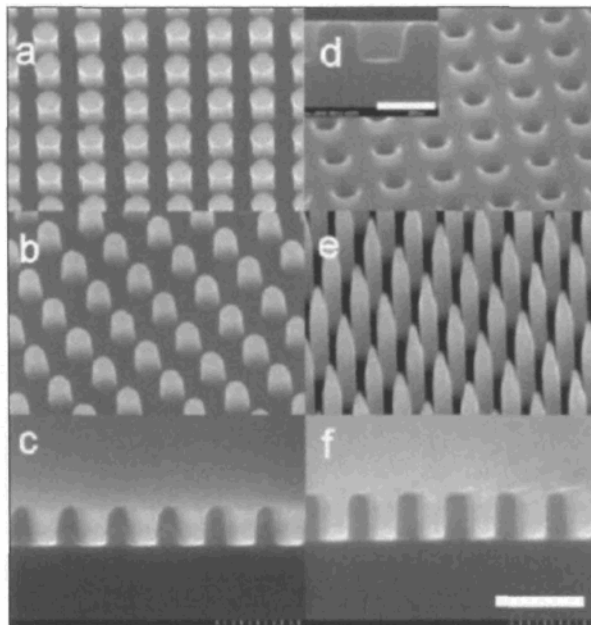


**Figure 2.16.** SEM images of nanopits and nanopillars formed on silicon by photolithography; scale bar 500 nm (a–f) and 200 nm (inset in (d)), respectively [77].

Lithography usually involves irradiation with light through a mask with the desired features imprinted onto a photoresist which coats the substrate (often silicon). Subsequent etching steps yield the desired patterned surfaces [68]. Photolithography can be again categorized into X-ray, UV, electron beam lithography etc., depending on the type of radiation used [76]. Figure 2.16 shows SEM images of nanopillars and nanopits produced on silicon by photolithography [77].
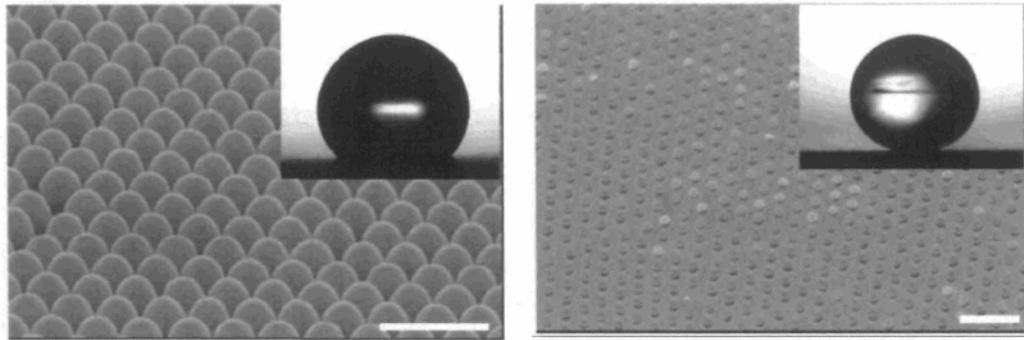


**Figure 2.17.** SEM images of size-reduced polystyrene beads and the water contact angle measurement on the corresponding modified surfaces (insets). The diameters of polystyrene beads and water contact angles on these surfaces are (left) 400 nm, 135°, (right) 190 nm, 168°. Scale bar: 1 $\mu$m [82].

A photocatalytic lithographic technique used in patterning gold surfaces produced superhydrophobic gold surfaces with CAs of 150–160° following perfluorodecanethiol (PFDT) modification [89]. Nanosphere lithography has been used to create well-ordered, spherically shaped nanopatterns of polystyrene [79,82]. Shiu *et al.* reported contact angles

tunable from 132° to as high as 170° using a polystyrene nanosphere lithographic pattern as shown in Figure 2.17 [82].

*Substrate etching* is another method used in creating rough patterns on substrate surfaces. Etching is performed by dry or wet etching. Plasma treatments, reactive ion etching (RIE) etc., are techniques used in dry etching [68,90]. A combination of photolithography and deep reactive ion etching (DRIE) has been used by Callies *et al.* in producing superhydrophobicity on photolithographically patterned silicon surfaces with a reported CA of higher than 160° [90]. Wet chemical etching has been recently carried out by Sarkar *et al.* and a CA of 164° and a CAH less than 2.5° have been reported [81].

*Sol-gel chemistry* is widely used to make a coating solution, which upon simple evaporative drying and annealing processes, develops a nanoscopically rough coating surface [91,92]. Sol–gel processes have been used to fabricate superhydrophobic surfaces from a variety of materials [93]. Shang *et al.* [83] described a procedure to make a transparent superhydrophobic surface by modifying silica-based gel films with a fluorinated silane. The authors reported a CA of 165° after passivation with fluoro-1,1,2,2-tetrahydrooctyldimethylchlorosilane (TFCS, $CF_3(CF_2)_5(CH_2)_2(CH_3)_2SiCl$). Sol-gel processes are also used to directly deposit a superhydrophobic film by incorporating low surface energy materials in the sol. Hikita *et al.* used colloidal silica particles and fluoroalkylsilane as the starting materials and prepared a sol–gel film with super-liquid-repellency by the hydrolysis and condensation of alkoxysilane compounds [84]. They reported a CA of ~150°.

*Electrodeposition* is another common method used to obtain superhydrophobic surfaces via electrochemical processes [85]. Zhang *et al.* prepared dendritic gold deposited by electrochemical deposition onto an indium tin oxide (ITO) electrode modified with a polyelectrolyte multilayer, which shows super-hydrophobic properties after further chemisorption of a self-assembled monolayer of n-dodecanethiol, providing a CA variation from 156° to as high as 173° depending on the deposition time (Figure 2.18) [85].
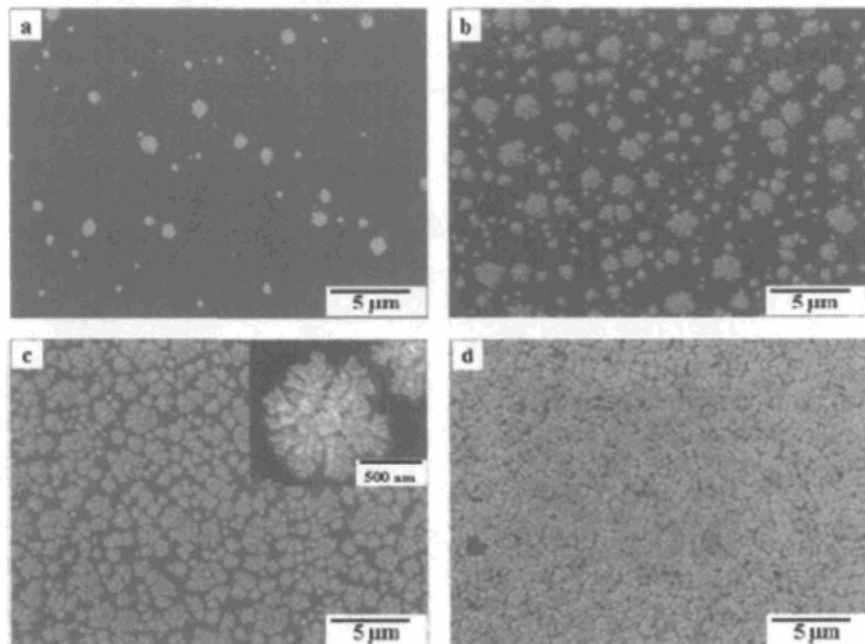


**Figure 2.18.** SEM images of dendritic gold clusters formed on an ITO electrode modified with a polyelectrolyte multilayer by electrochemical deposition at -200 mV (vs Ag/AgCl). Deposition time is 2 s (a), 50 s (b), 200 s (c), 800 s (d) [85].

Anodization is another electrochemical process which is in use to produce porous microstructures on the surface [94]. A CA of $160^{o}$ and CAH $<1^{o}$ has been reported on polytetrafluoroethylene replicate using porous alumina produced by an anodization process.
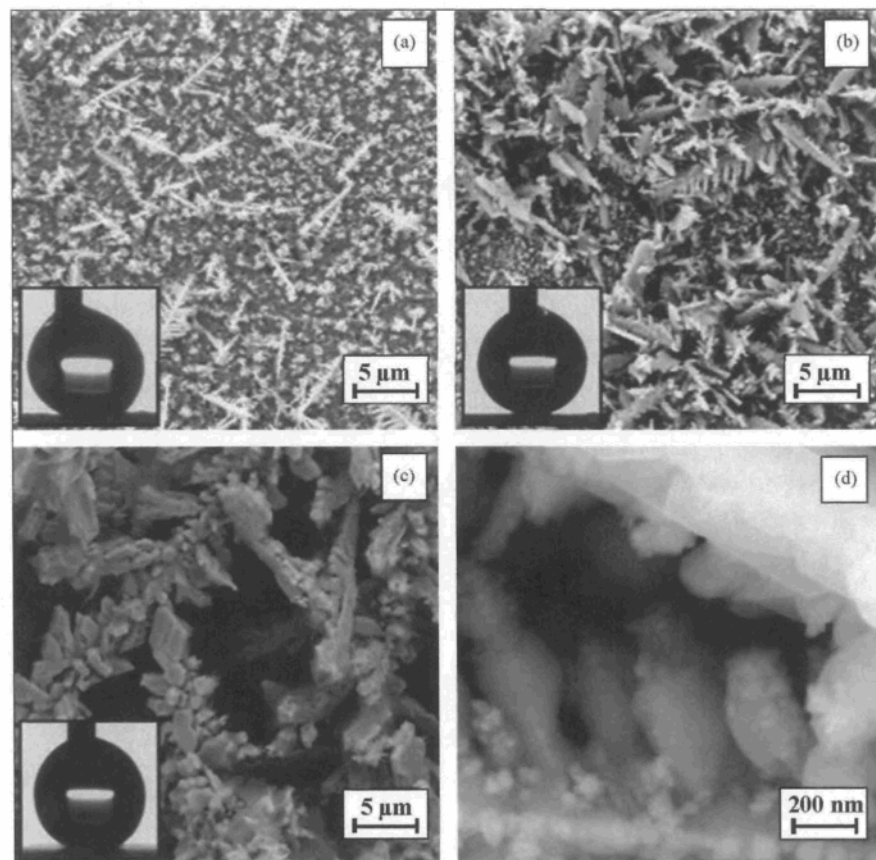


**Figure 2.19.** SEM images of samples prepared using three different initial Ag+ concentrations of (a) 13.2 mM, (b) 24.75 mM and (c) 396 mM, respectively; and (d) a magnified section of (b). In the insets, the appearances of the droplets are shown [86].

Another process in electrochemistry is a simple electroless technique, also referred to as a galvanic exchange reaction [86]. Safaee *et al.* produced fractal-like silver films on copper substrates by simply immersing a copper substrate in a solution of silver nitrate (Figure 2.19); an electrochemical reaction takes place in which copper reduces silver ions. The authors reported a variation in the CA with respect to the concentration of the silver nitrate solution which apparently controls the surface morphology of the silver films leading to different roughness factors. The highest CA achieved by the authors following passivation with *-CH₃* terminated stearic acid was 156° with a CAH <5°, using a solution containing 24.75 mM silver nitrate.

*Chemical bath deposition (CBD)* is a simple wet chemical route to deposit micro-nanorough layers which involves a controlled precipitation from a solution of a compound on a suitable substrate. Saleema *et al.* obtained a CA as high as ~173° and a CAH as low as 1.4° on ZnO nanotowers deposited on silicon substrates via a CBD technique [88].

Several other techniques such as chemical or physical vapor deposition (CVD, PVD) [95], phase separation [96], sublimation [97], template methods [98], layer-by-layer methods [99], etc., exist in preparing superhydrophobic surfaces. A list of papers on the processing of superhydrophobic surfaces and films up to the year 2000 has been provided by A. Nakajima *et al.* in Table 1 in their "invited review" article [65].

The *passivation* of surfaces, roughened or micro-nanopatterned for superhydrophobicity, is usually performed using one of two methods: chemical and physical. Chemical methods involve the self-assembly of a monolayer of fatty acids, methylated or fluorinated compounds by simply immersing the substrate into a solution of

the passivating molecules. A self-assembled monolayer of the compound is formed on the substrate surface with the low surface energy hydrophobic head groups oriented upward away from the surface. The surface energies of the methylated and fluorinated groups decrease in the following manner: - $CF_3$ < $CF_2H$ < - $CF_2$ - < - $CH_3$ < - $CH_2$ – [83]. Shang *et al.* reported that the higher the fluorine content, the lower will be the surface energy. Physical methods such thin film coating with fluorinated-diamond like carbon (F-DLC) using a plasma are used to lower the substrate surface energy [100,101]. The aforementioned examples of creating roughness with a view to achieving superhydrophobicity have also provided examples of passivation in certain cases.

This brief review on superhydrophobicity emphasizes the importance of two requirements - roughness and low surface energy – in creating superhydrophobic surfaces.

# CHAPTER 3

# EXPERIMENT

In this chapter, the techniques used for synthesizing and characterizing the materials will be discussed along with the experimental procedures used. This chapter will be divided into two sections - Materials synthesis and Materials analysis.

## 3.1 Materials synthesis

Superhydrophobic dielectric surfaces were produced using three successive steps – (i) creating nanoroughness on the substrate surface; (ii) coating of the nanorough substrate surface with a dielectric film; and (iii) passivating the nanorough dielectric surface to lower the surface energy. The substrate materials used were mainly silicon (100) (Si (100)) and aluminum 6061 Al alloy (Al 97.9 wt.%, Mg 1.0 wt.%, Si 0.60 wt.%, Cu 0.28 wt.%, Cr 0.20 wt.%).

**3.1.1 Substrate cleaning:** Prior to any treatment, the substrates were ultrasonically cleaned for 20 minutes with 1% LIQUINOX (Sigma Aldrich) followed by ultrasonication in de-ionized water for 20 minutes and dried with nitrogen followed by oven drying at 70 °C for several hours to remove excess water.

**3.1.2 Creation of surface nanoroughness on the substrates:** Surface roughness plays a very important role in obtaining superhydrophobic properties. Therefore, substrate chemical etching was used to create nanorough substrates.

**Substrate chemical etching:** "Etching" refers to the removal of material from a surface via wet or dry processes. In dry etching, the material is sputtered or removed using reactive ions or a vapor phase etchant. In wet etching, the material is dissolved by immersing in a chemical solution and the technique is often referred to as "chemical etching". Chemical etching is a very simple and less expensive technique which needs simply an appropriate chemical etchant and a proper container.

In this work, aqueous potassium hydroxide (KOH) and dilute hydrochloric acid (HCl) were used as etchants to etch Si (100) and Al, respectively. Si (100) coupons were immersed for 10 min in KOH solutions of various concentrations after the solution reached a temperature of 70 °C on a hotplate. A chemical reaction of KOH with Si (100) occurs resulting in a rough micro-pyramidal surface pattern. After 10 min of etching, the substrates were rinsed in de-ionized water and cleaned ultrasonically to remove any debris resulting from etching. The Al coupons, washed in tap water, were immersed in 40% aqueous HCl solution at room temperature for ~ 3 min. A chemical reaction of HCl with Al removes some material from the Al surface leading to a rough nano-porous structure on the surface. The etched coupons were then rinsed in running tap water to stop further reaction and cleaned by ultrasonication in de-ionized water to remove any debris. The nanorough Si (100) as well as nanorough Al substrates were dried in an oven for several hours to remove excess water from their surfaces.

51

**Preparation of alumina substrates:** Alumina substrates were prepared by plasma oxidizing Al substrate surfaces in an inductively coupled plasma reactor by applying a power of 50 W using $O_2$ and Ar gases at a flow rate of 28 sccm and 7 sccm, respectively. The oxidation of the Al surfaces was carried out at room temperature with a total process time of 30 min. The Ar pressure within the process was maintained at 20 mTorr and the base pressure in the chamber was $2 \times 10^{-6}$ Torr. A DC bias of 25 V was applied during the process.

### 3.1.3 Preparation and coating of oxide thin films:
Nanostructures of oxides can be generated by numerous preparation methods typically described as physical and chemical methods [102,103]. Physical methods which include sputtering, pulsed laser deposition (PLD), atomic layer deposition (ALD) etc., [104] that have been used for preparing titania, zirconia and alumina nanostructures [103], require high vacuum conditions and are usually expensive. Chemical methods include chemical vapor deposition (CVD), metal-organo chemical vapor deposition (MOCVD), liquid phase methods such as sol-gel synthesis, chemical bath deposition (CBD), etc. [105]. Among these, the solution routes are comparatively simple and easy, not only for continuous film deposition [106,107] but also for films composed of particles with specific sizes [108]. Sol-gel synthesis, a solution route, is becoming a standard method for oxides and is based on the hydrolysis of reactive metal precursors, usually alkoxides in an alcohol solution, resulting in a gel that is subsequently thermally treated to yield the nanostructured product. [93,109]. In general, sol-gel polymerization occurs in three stages: the polymerization of monomers to form particles,

the growth of particles, and the linking of particles into chains and then networks that extend throughout the liquid medium, thickening into a gel. Metal oxide films such as alumina [110], titania [107] and zirconia [111] are easy to fabricate by sol-gel methods combined with a spin or dip coating technique. A basic recipe to coat oxide particles on a substrate by the sol-gel method is schematically represented in Figure 3.1. CBD is another chemical route which involves the controlled precipitation from solution of a compound on a suitable substrate.
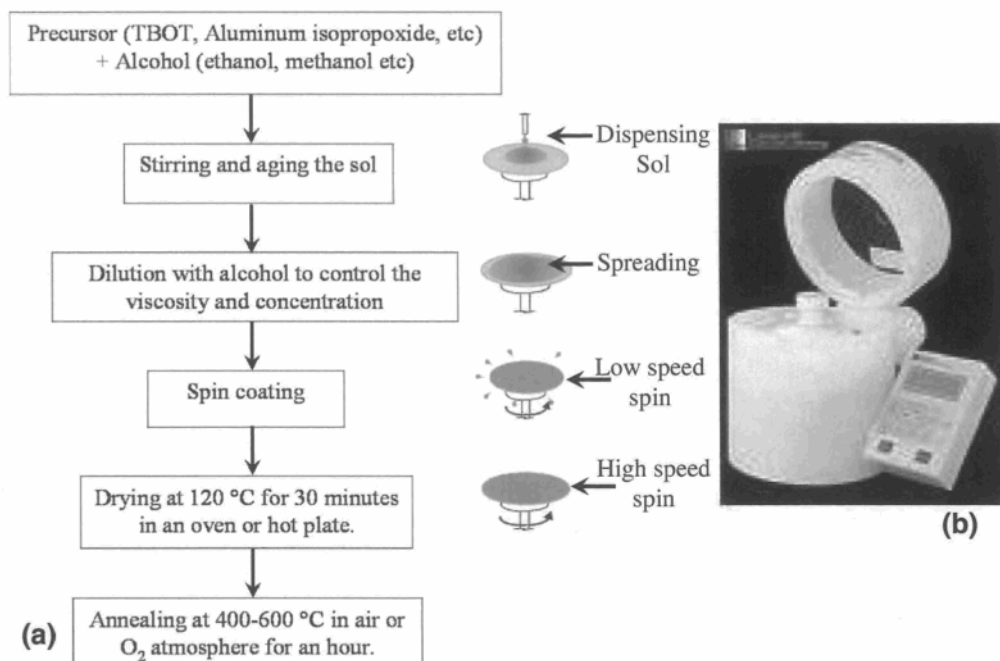


**Figure 3.1.** (a) Basic procedures in a sol-gel spin-coating or dip-coating technique, (b) the spin-coater (model WS-400B-6NPP, Laurell technologies corporation)

In this study, two oxides with different dielectric constants, namely, ZnO ($\varepsilon = 8$) and TiO$_2$ ($\varepsilon = 80$), were coated onto Si (100) and Al substrates via a sol-gel spin coating procedure. Sol-gel procedures described in the literature were followed to prepare the two oxides whose dielectric constants are in the lower range of ~8 for ZnO as reported by Alexander *et al.* [112] and in the higher range of ~80 for TiO$_2$ as reported by Sarkar *et al.* [113,114]. Although we did not measure the dielectric constants of the oxide films we deposited, the physical properties such as the crystal structure and film thickness of the dielectric coatings have been investigated by X-ray diffraction (XRD) and Rutherford backscattering spectrometry (RBS) measurements respectively *(see Appendix 1)*, and were found to be consistent with those literature reports. It is therefore reasonable to expect that the electrical properties will also be similar to those described by Alexander *et al.* and Sarkar *et al.* A brief list of oxides and their dielectric constants is also provided by Robertson [115]. The details of the preparation procedures used for the two dielectrics are given in the following paragraphs. In addition to the sol-gel procedures mentioned above, chemical bath deposition was employed to create superhydrophobic ZnO nanotowers on Si (100) substrates.

**Chemical bath deposition (CBD):** A chemical bath consisting of 100 ml of aqueous 0.1 M zinc nitrate (Zn(NO$_3$)$_2$) and 4 ml of 28% aqueous ammonium hydroxide (NH$_4$OH) solution was prepared. Ultrasonically cleaned and hydrofluoric acid etched silicon substrates were immersed in the chemical bath for the growth of ZnO nanotowers. The growth process of ZnO nanotowers involves a chemical reaction during which the zinc nitrate decomposes to give ZnO in the presence of ammonium hydroxide [116].

54

**Sol-gel spin coating of ZnO:** A stock solution of 0.5 M ZnO sol was prepared by dissolving 10.975 g zinc acetate dihydrate (($CH_3CO_2)_2Zn.2H_2O$) (Sigma Aldrich) in 100 ml methanol under constant stirring at 500 rpm on a hotplate maintained at 80 °C for 30 min. The resulting transparent sol was aged for ~48 h prior to coating. A desired concentration of the stock ZnO sol was deposited dropwise onto the substrates and spin coated using a spin-coater (Laurell Tech, model WS-400B-6NPP) (Figure 3.1 (b)) at 3000 rpm for 30 s followed by drying on a hotplate at 120 °C for 30 min and then annealing in air at 450 °C for another 30 min.

**Sol-gel spin-coating of TiO₂:** A stock solution of 0.4M $TiO_2$ sol was prepared by diluting the tetrabutoxy titanium (TBOT) precursor with ethanol at a 1:1 volume ratio under constant stirring at 500 rpm for 10 min at room temperature. A desired concentration of the 48 h aged stock $TiO_2$ sol was deposited dropwise onto the substrates and spin coated at 4000 rpm for 30 s followed by drying on a hotplate at 120 °C for 30 min and then annealed in air at 450 °C for 30 min.

**3.1.4 Passivation techniques:** Passivation is a term used for the modification of a surface to lower its surface energy either by chemical or by physical methods without altering the surface morphology. CBD ZnO nanotowers were passivated by immersing in stearic acid (SA) solution. The dielectric oxide coated surfaces were passivated either by immersing the samples in a solution of fluoroalkyl-silane (FAS-17) or by sputtering material from a Teflon® target onto the sample surfaces using an inductively coupled plasma reactor.

**SA passivation:** The as-prepared ZnO samples, with an oxide layer coated at an oven temperature of 70 °C, were oven dried for more than 10 h at 70 °C, cooled to room temperature, and then passivated with $2 \times 10^{-3}$ M stearic acid (SA) ($CH_3(CH_2)_{16}COOH$) in acetone for 30 min by immersion. The chemical structure of SA is shown in Figure 3.2.
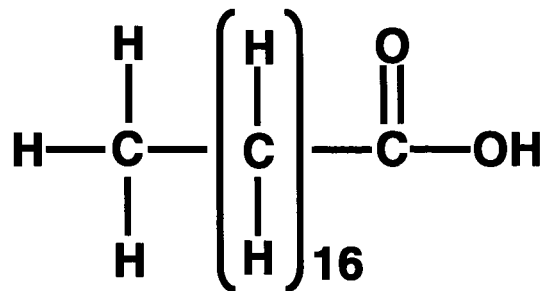


**Figure 3.2.** Chemical structure of stearic acid molecule.

**FAS-17 Passivation:** The chemical structure of an FAS-17 molecule ($C_{16}H_{19}F_{17}O_3Si$) (Sigma Aldrich), a fluorine-containing organosilane compound, is shown in Figure 3.3. The samples were immersed in beakers containing FAS-17 dissolved in ethanol. The passivation was carried out for a period of 10 min to allow the self-assembly of a monolayer of FAS-17 molecules on the sample surface. The passivated samples were dried in an oven for several hours prior to any further characterization.
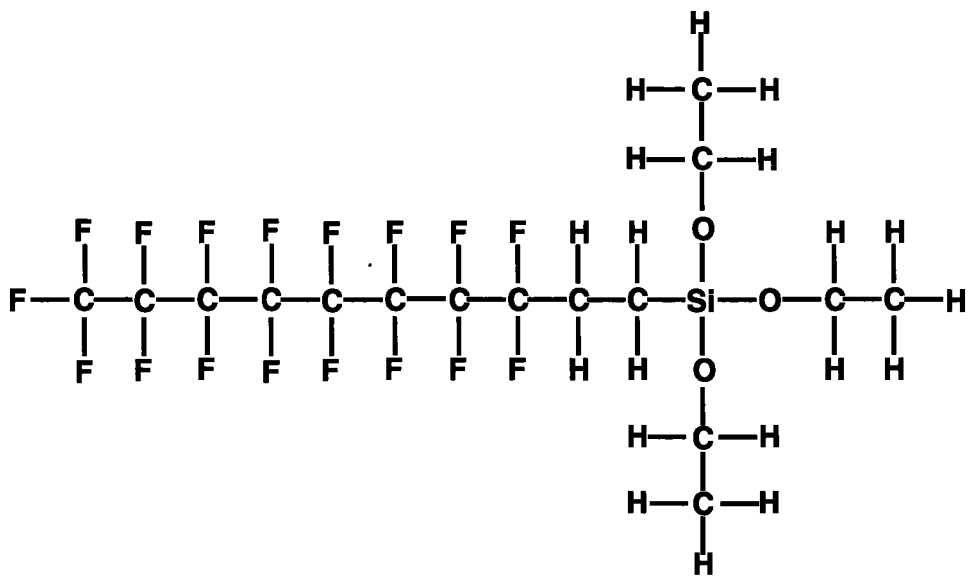
**Figure 3.3.** Molecular structure of FAS-17.

**Rf-sputtered Teflon® coating:** Sputtering is a technique used to deposit thin films onto a substrate surface. By accelerating ions from a gaseous plasma (usually Ar) onto a source material (a target), the source material is eroded via energy transfer and ejected as neutral particles, which may be either individual atoms or clusters of atoms or molecules. These neutral particles, during their trajectory, come into contact with the surface of the substrate and are deposited as a thin film of the source material.
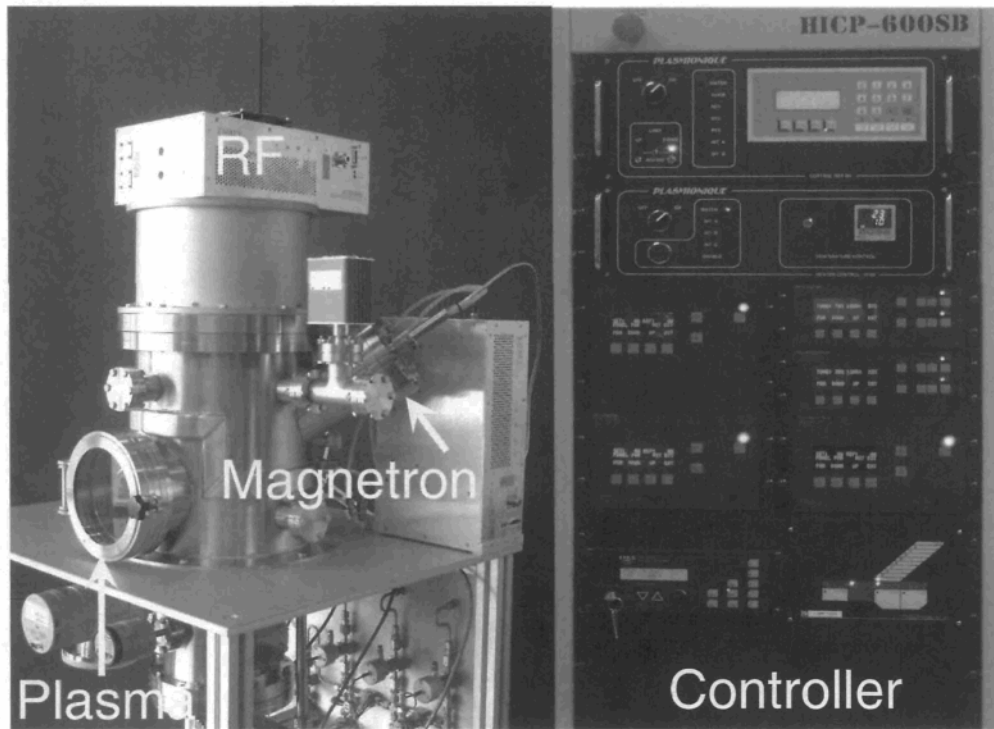
**Figure 3.4.** Inductively coupled plasma reactor (CIGELE, UQAC) used for 13.5 MHz rf-sputtered Teflon® coating.

In this study, material from a Teflon® target was sputtered onto the sol-gel spin-coated oxide surfaces using an Ar plasma in an inductively coupled plasma reactor (Figure 3.4) by applying a power of 50 W. The distance between the target and the substrate was 30 cm. The sputtering process was carried out for ~ 20 min at an Ar pressure of 20 mTorr in the chamber during process. The base pressure was $2 \times 10^{-6}$ Torr.

## 3.2 Materials analysis

**3.2.1 Morphological analyses:** An atomic force microscope (AFM) (Digital Nanoscope IIIa by Digital Instruments, Veeco) and a scanning electron microscope (SEM/EDX) (JEOL JSM 6300F FESEM, INRS, Varennes and LEO FESEM, CTA, Chiocutimi) were used for morphological characterizations.
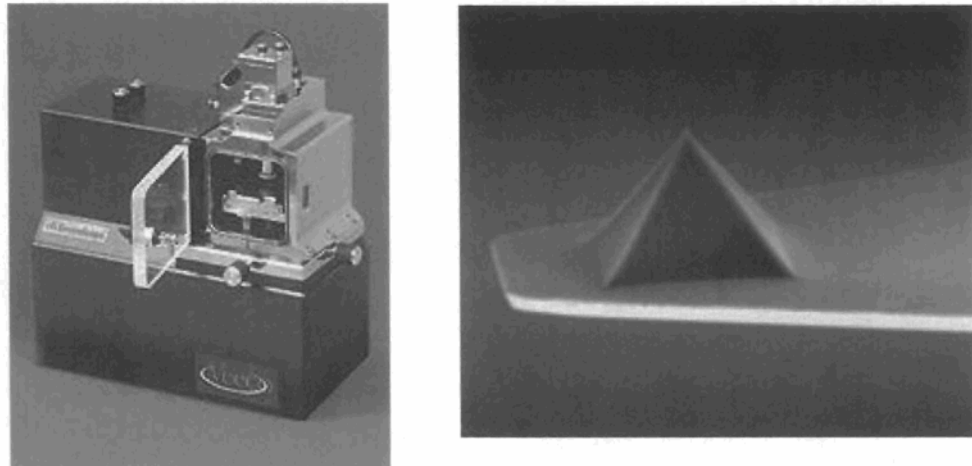


**Figure 3.5.** (Left) Atomic force microscope (AFM), (Nanoscope III by Veeco), CIGELE, UQAC, (Right) silicon nitride probe (tip radius <15 nm) fixed on a cantilever.

**Atomic force microscope (AFM):** AFM (Figure 3.5 (Left)) measurements were performed in tapping mode, in which the topography of the surface is mapped by lightly tapping the surface with an oscillating silicon nitride probe (Figure 3.5 (Right)) of tip radius less than 10-15 nm and height 10-15 μm fixed on a cantilever of length 220-230 μm and

width 35-45 µm. The surface topography is imaged by monitoring the changes in the cantilever's oscillation amplitude as it scans over the surface. The advantage of using AFM is that it can image the three dimensional (3-D) topography of the surface and provide information such as the dimensions of the nanoscale features of the surface including the z-height, surface roughness, etc.
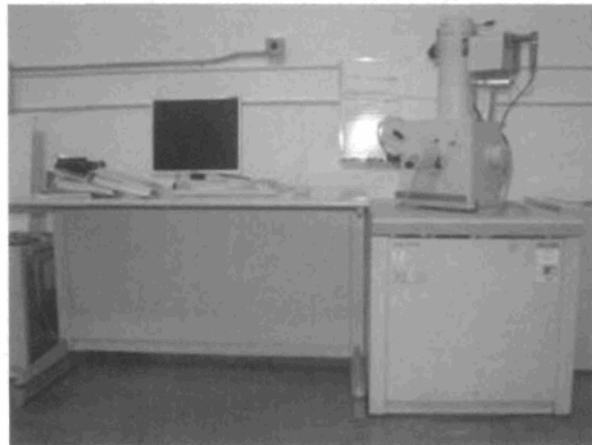


**Figure 3.6.** JEOL JSM 6300F FESEM, INRS-ÉMT, Varennes, Montréal; electron acceleration voltage: 20kV

**Scanning electron microscope (SEM/EDX):** SEM/EDX (Figure 3.6) measurements were performed in two different laboratories. The dielectric samples were coated with either carbon (INRS) or platinum (CTA) prior to imaging to prevent surface charging effects. SEM measurements provide a two dimensional image of the morphological features of the surface as well as the chemical composition of the material

via energy dispersive X-ray analyses. Most importantly, SEM can image surfaces with any degree of roughness unlike AFM which is not suitable when a surface is too rough.

**3.2.2 Surface chemical analyses:** X-ray photoelectron spectroscopy (XPS) (ESCALAB 220iXL, INRS-ÉMT, Varennes) and Fourier transform infrared spectroscopy (FTIR) (PerkinElmer Spectrum One, UQAC) were used for the surface chemical analyses of the dielectric coatings prior to and after passivation as well as prior to and after ice adhesion tests.

**X-ray photoelectron spectroscopy (XPS):** XPS is a surface analysis technique used to determine the atomic composition and chemistry of a surface. XPS, which is very surface-sensitive with a sampling depth of only a few nanometers, is based on the photoelectric effect and works by irradiating a sample surface with low-energy (~1.5 keV) X-rays, in order to provoke the emission of photoelectrons. These photoelectrons are collected and analyzed by the instrument to produce a spectrum of emission intensity versus electron binding energy ($E_b$), which is the difference between the X-ray photon energy $h\upsilon$ and the kinetic energy of the photoelectron $E_k$. Since each element has a unique set of orbital binding energies, XPS can be used to identify the elements on the surface.

Figures 3.7 shows the photograph of the XPS instrument of INRS-Varennes. The XPS spectra at INRS were collected by using the ESCALAB 220iXL spectrometer, with a Mg $K_\alpha$ (1253.6 eV) X-ray source. Certain samples were measured using an Al $K_\alpha$ (1486.6 eV) source. The spectrometer is equipped with six channeltron detectors. The analyzer pass energy was set to 100 eV for the survey scans and to 20 eV for the high resolution core-

level spectra of all the elements of interest. The power of the X-ray source was set to 300 W. The base pressure in the analyzer chamber is close to $10^{-10}$ Torr. The acquired XPS data were processed by using CasaXPS software.



**Figure 3.7.** XPS ESCALAB 220iXL, INRS-ÉMT, Varennes, Montréal

**Fourier transform infrared (FTIR) spectroscopy:** In FTIR spectroscopy (Figure 3.8), infrared radiation is passed through a sample and some of the infrared radiation is absorbed by the sample. The resulting spectrum represents the molecular absorption, creating a molecular fingerprint of the sample. FTIR was useful in elucidating

the molecular structure of the organic molecules used for surface passivation, particularly in recognition of the functional groups as well as the bonding of the dielectric coatings with the substrates. An ultrasonically cleaned piece of silicon was used as a reference for background subtraction prior to measurement of the samples. The number of scans used was 20.



**Figure 3.8.** Fourier transform infrared spectroscopy (FTIR) apparatus (PerkinElmer Spectrum One, UQAC)

**3.2.3 Superhydrophobicity - contact angle (CA) measurements:** A contact angle goniometer (Krüss GmbH, Germany) (Figure 3.9 (a)) was used to test the hydrophobic and superhydrophobic properties of the different surfaces studied. A standard experimental procedure [90] was followed to measure the contact angle hysteresis, which is the difference between the advancing and receding contact angles (Figure 3.9 (b)).
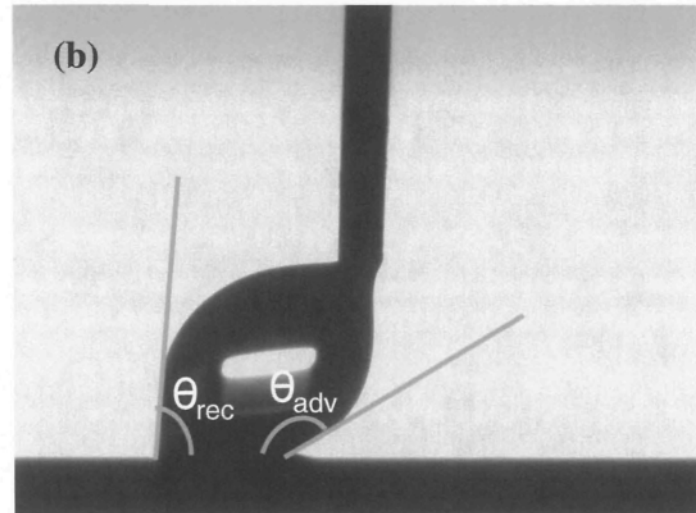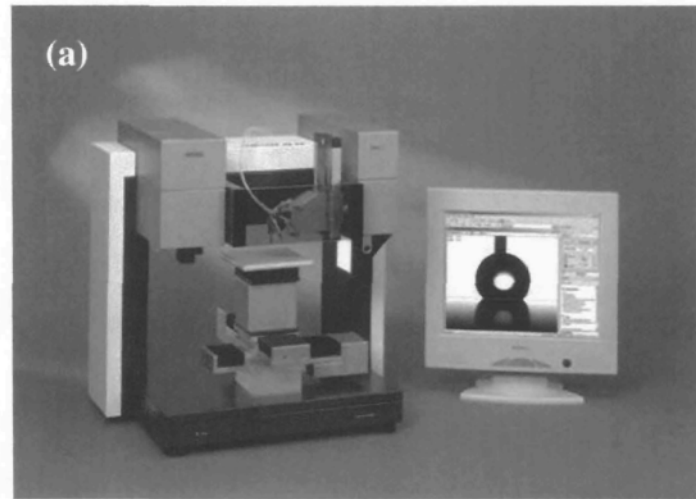
**Figure 3.9.** (a) Contact angle measuring device (DSA 100, Krüss Germany), CIGELE, UQAC; water drop size 5-7 µL, (b) Contact angle hysteresis measurement on a sticky surface $(CAH=\theta_{adv}-\theta_{rec})$.

A water drop of volume ~5 µL is suspended from the syringe needle and brought into contact with the superhydrophobic surface using a computer controlled device as provided by Krüss GmbH. The advancing and receding contact angles are measured by holding the needle stationary and moving the sample in one direction. The static contact angle data were acquired by fitting the symmetric water drops using the Laplace-Young equation and the advancing and receding contact angles were measured on the asymmetric water drops using the tangent-2 method [117].

**3.2.4 Ice adhesion tests:** Ice adheres strongly to almost all surfaces and yet test methods to evaluate the strength of ice adhesion to surfaces are scarce. A few test methods do exist but they use complicated time consuming test procedures and moreover, these methods are quite expensive [118-120]. Therefore, two simple methods were developed at the CIGELE laboratories using the available resources such as a wind-tunnel, to evaluate the adhesion strength on the various surfaces studied which are of dimensions as small as 2.5 × 2.5 cm$^2$ – the Pulling test and the Centrifugal adhesion reduction test (CAT).

**Pulling Test:** In this method, the adhesion strength of ice is evaluated by measuring the force required to detach the ice grown on a sample surface by mechanically pulling the ice from the surface (Figure 3.10). A thermocoal block with a hole drilled through the centre with the sample affixed at one end is used as the mold to grow the ice. The ice is grown by freezing de-ionized water at ~ -20 °C. The ice grown on the sample is then separated from the mold by cleaving off the thermocoal surrounding the cylindrical column of ice. The apparatus used to test the adhesion strength of ice mainly consists of a stand

holding a pulley and a strong base to hold the sample with the ice intact. A cord goes over the pulley to a spring balance attached to the ice on the sample. With the sample fixed to a base, the ice is slowly pulled vertically upwards by applying a force to the free end of the cord and the force needed to detach the ice from the surface read from the spring balance provides the force of adhesion and hence the adhesion strength $\sigma = F/A$, where $A$ is the geometric area of contact of ice with the surface and $F = mg$, where $m$ is the mass required to detach the ice from the sample surface and $g$ is the gravitational force. This method is useful in determining the adhesion strength of ice on hydrophilic samples as ice adheres strongly on those surfaces with lower water contact angles. However, on surfaces that are superhydrophobic with very low contact angle hystereses and very high contact angles of water, this method was not found to be effective as the ice just slid off those surfaces during separation from the mold due to its poor adhesion.
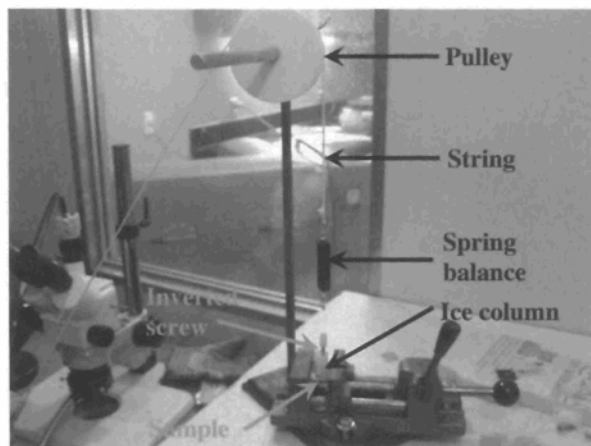


**Figure 3.10.** Photograph of the apparatus used to measure the ice adhesion strength.

**CAT tests:** The CAT apparatus was designed and developed in-house at CIGELE laboratories following the intensive use by the Anti-icing Materials International Laboratory (AMIL), UQAC, Chicoutimi, of their own CAT apparatus as a standard method for testing various surfaces for ice adhesion strength [121]. In this method, an aluminum beam (32 mm wide and 30 cm long) with the test sample (32 mm × 50 mm) with accumulated ice attached to one end, and a counter weight attached to the other end to balance the beam, is fixed in the home-built centrifuge test chamber (Figure 3.11) maintained at $-10\,^{\circ}$C. The beam is then rotated at increasing speeds resulting in a controlled ramp of the centrifugal force. When this force reaches the adhesion force of ice, the ice detaches from the sample surface. The exact rotation speed at the time of ice detachment is determined from the computer software developed in-house.

The adhesion force $F = mr\omega^2$ is determined after the ice detaches, where $m$ is the mass of ice; $r$ is the radius of the beam; and $\omega$ is the rotation speed. The shear adhesion strength ($\tau = F/A$) of ice is then determined from the apparent area $A$ of the sample surface which was in contact with ice. Bare aluminum was used as a standard reference sample, confirming after several test runs the adhesion strength of ice to be $420 \pm 27$ kPa, in agreement with the literature values [17,121,122]. The adhesion reduction factor (ARF) is calculated for the different coatings as compared to the bare aluminum. The higher the ARF, the higher will be the reduction of ice adhesion to the surfaces. The ARF of bare Al is 1.
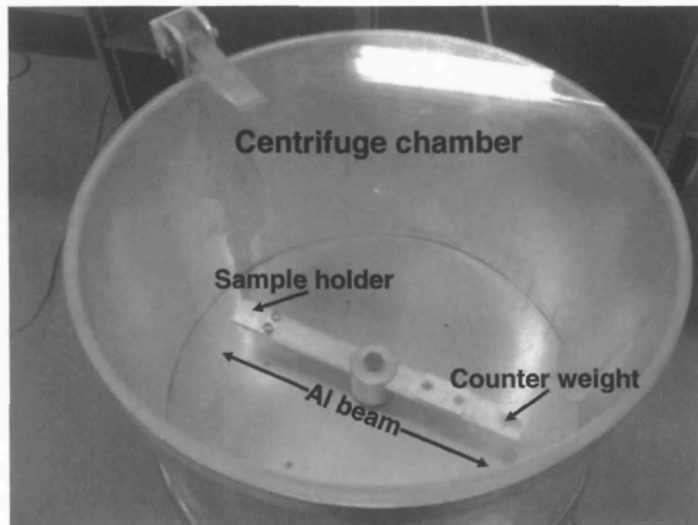
**Figure 3.11.** Centrifugal chamber where the ice-covered samples are fixed on the sample holder and the Al beam rotated under computer control.

Prior to the rotation in the centrifugal apparatus, the beams with the sample fixed are weighed both before and after the accumulation of ice to obtain the mass ($m$) of the accumulated ice. Ice is accumulated on the test samples from a freezing drizzle of supercooled water droplets of droplet size ~20 µm at –10 °C in a wind tunnel (Figure 3.12) at a fixed wind speed of 10 ms$^{-1}$ in order to simulate atmospheric icing conditions in natural outdoor situations. Figure 3.13 shows a schematic representation of the ice accumulation procedure in the wind tunnel. The samples are placed vertically in the tunnel as shown in Figure 3.13, perpendicular to the direction of flow of the freezing drizzle.
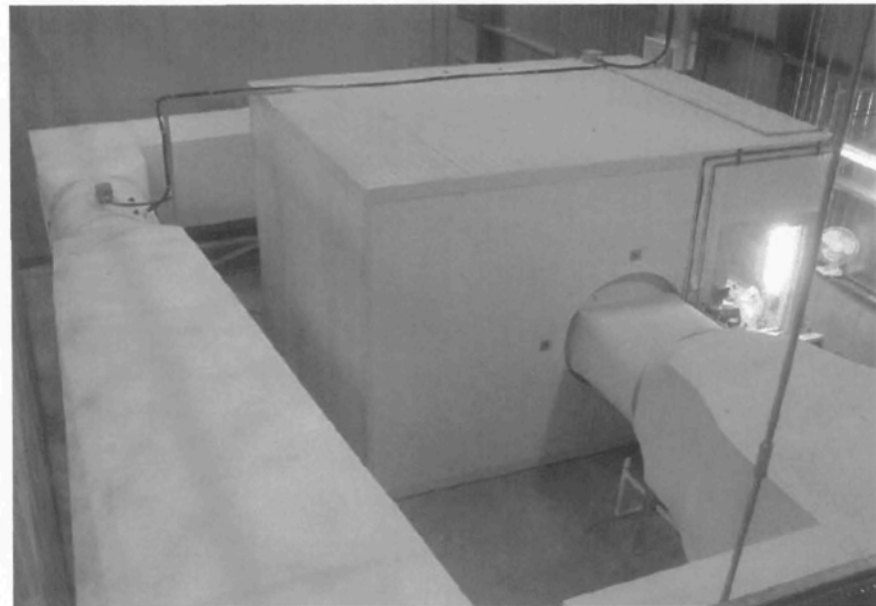
**Figure 3.12.** Top view of CIGELE's atmospheric icing wind-tunnel.



SAMPLE

-10 ºC

WIND TUNNEL

FREEZING
DRIZZLE
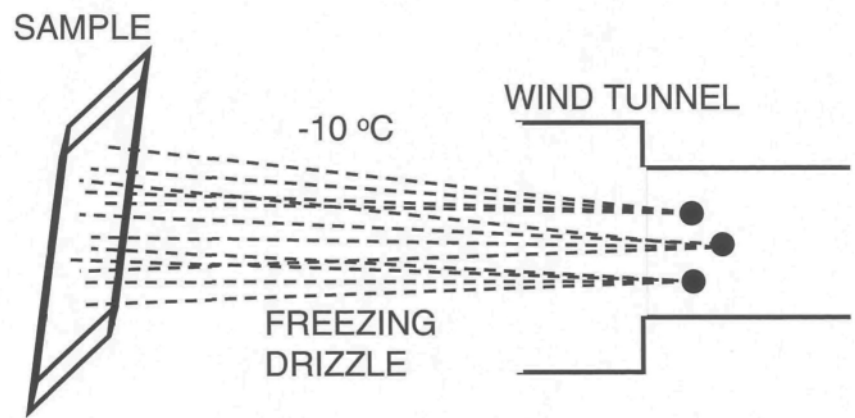
**Figure 3.13.** Schematic of ice accumulation on a sample surface in the wind tunnel

# CHAPTER 4

## NANOTOWERS BY CHEMICAL BATH DEPOSITION

### 4.1 Introduction

Zinc oxide (ZnO), widely used in a diverse range of technological applications such as solar cells, photo detectors, light emitting devices, gas sensor elements, etc., has attracted attention in the field of nanoscience due its unique structural, optical and electrical properties [123-125]. There exist several sophisticated techniques to synthesize ZnO thin films such as sputtering, pulsed laser deposition, chemical vapor deposition, molecular beam epitaxy, sol–gel process, etc. for different applications [126-130]. Chemical bath deposition (CBD), among various techniques, has gained popularity recently because it is simple, low cost and can be performed at low temperatures [131,132]. In this thesis, since superhydrophobicity is proposed as a pre-requisite to icephobicity, achieving superhydrophobic surfaces was initially given priority. Due to the feasibility of ZnO deposition via CBD and sol-gel processes, and due to the initially limited laboratory resources, the two methods were used to produce ZnO surfaces. Superhydrophobicity on those surfaces was achieved by passivating those surfaces with stearic acid (SA) $((CH_3(CH_2)_{16}COOH))$ molecules dissolved in acetone. Although superhydrophobicity on CBD ZnO surfaces has previously been achieved using other organic compounds such as FAS [133], the strength of bonding of those compounds to ZnO has not yet been described.

70

Studies on the thermal decomposition of surfactant coatings such as oleic acid, stearic acid and poly(ethylene glycol) have been carried out on nanostructured metal surfaces [134,135], however, such studies are scarce on oxide surfaces. Therefore, the present study on SA passivated CBD ZnO surfaces was further advanced to investigate the thermal stability of the superhydrophobic properties by investigating the thermal desorption of the SA molecules on those surfaces following annealing at elevated temperatures. The thermal desorption studies were carried out by monitoring the change in the FTIR peak intensities of the organic components present in SA.

In the following sections, this chapter details the achievement of superhydrophobic ZnO nanotowers via CBD following passivation with SA molecules and the thermal stability of the superhydrophobic properties of those surfaces.


## 4.2 Surface characterization

In the CBD of ZnO, the ZnO growth process involves a chemical reaction during which zinc nitrate decomposes to give ZnO in the presence of ammonium hydroxide, as follows:

$$Zn(NO_3)_2 + 2NH_4OH \rightarrow Zn(OH)_2 + 2NH_4NO_3$$

$$Zn(OH)_2 + NH_4OH \rightarrow (NH_4)ZnO_2^- + H_2O + H^+$$

$$(NH_4)ZnO_2^- + H^+ \rightarrow ZnO + NH_4OH$$
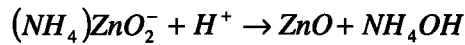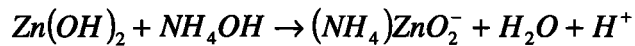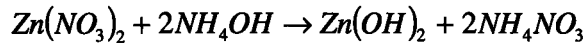
Figure 4.1 shows the FESEM images of the CBD ZnO nanotowers. Figure 4.1a shows the presence of randomly oriented hexagonal patterned ZnO nanotowers, and the hexagonal

patterns that have regular edges with an angle of 120° between adjacent sides are demonstrated in Figures 4.1b and 4.1c. The tendency to form hexagonal morphological features is due to the hexagonal crystal structure of ZnO [136]. Previous studies on the dimensions of the nanocolumnar ZnO from cross-sectional SEM analysis show a wide range of diameters and lengths of ~50–500 nm and ~250–2000 nm, respectively [136-140]. However, from the SEM image of the ZnO nanotowers, in Figures 4.1b and 4.1c, the diameter and the length of the nanotowers, further decorated throughout the top few nanometers with several nanosteps, could be ~500 and 700 nm, respectively, indicating that the ZnO nanotower films exhibit a high roughness. These observations reveal the presence of a rough binary structure with a combination of nanosteps on the nanotowers, which is a basic geometrical requirement along with chemical modification of the surface to achieve superhydrophobicity [68,69,141].

The as-deposited CBD ZnO nanotower film dried in a closed and clean oven was found to completely absorb water demonstrating hydrophilicity. However, the ZnO nanotower film became highly superhydrophobic following passivation with SA, providing a contact angle as high as $173 \pm 1.1°$ and a contact angle hysteresis as low as $1.4 \pm 0.5°$, water drops rolling off the surface with even the slightest tilt of the sample. Such a very low hysteresis of $1.4 \pm 0.5°$ is comparable with very low hystereses of ~2° as reported by Ming *et al.* [142] on poly(dimethylsiloxane) modified rough raspberry-like silica particles and <1° as reported by Zhu *et al.* [143] on fluorocarbon coated carbon nanotube arrays.

The cause for such a low hysteresis on the superhydrophobic ZnO nanotower surface could be attributed to the presence of a rough structure with a two-tier roughness that eventually reduces the area of contact between the drop and the nanotowers and trapping more air [142-144].
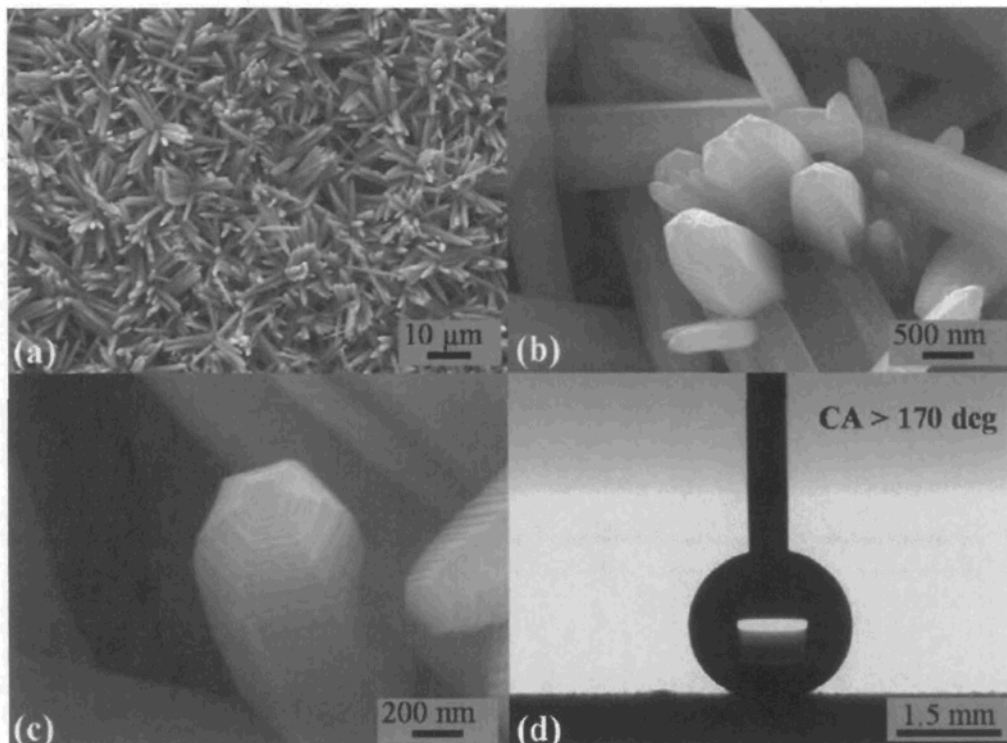


**Figure 4.1.** FESEM images of ZnO nanotowers at (a) low magnification (b) at high magnification showing the hexagonal morphology; (c) close up view of a single nanotower showing the nanosteps; (d) image of a water drop on the surface of these nanotowers after SA passivation.
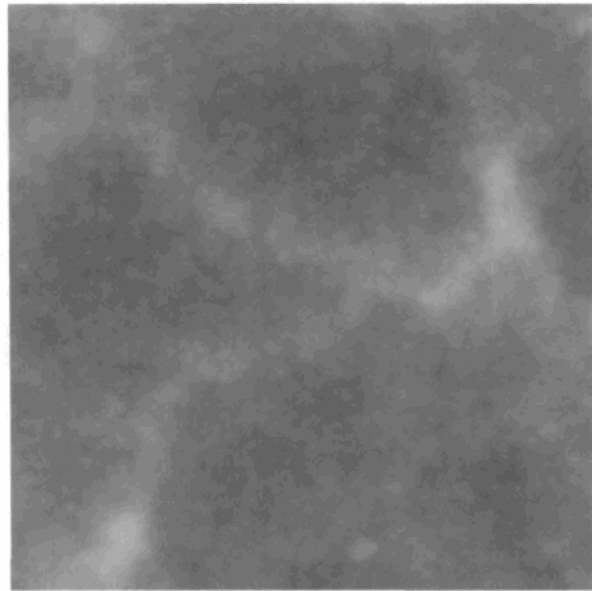
**Figure 4.2**. 2D AFM images of scan size 1x1 μm of sol-gel derived flat ZnO

As mentioned previously in the Chapter 2, the Wenzel and Cassie-Baxter models are used to explain the wetting behavior of a rough surface measured by means of the water contact angle. The Wenzel model [48], which applies to a situation in which air is not trapped beneath the water drop, states that true contact angles lower than $90^{\circ}$ on a smooth surface translate to an apparent contact angle lower than the true contact angle on a rough surface and vice versa. Therefore, a flat ZnO surface was prepared using a sol-gel technique as explained in the Chapter 3 (Experiment). Figure 4.2 shows the AFM image of the flat ZnO surface on which the *rms* roughness obtained was ~2 nm. The water contact angle of water of only $29.5 \pm 0.2^{\circ}$ on the as-prepared flat ZnO surface increased to $73.5 \pm 4^{\circ}$

following SA passivation which is still <90°. According to the Wenzel model, when such a surface is roughened, the CA is expected to be lower than 73.5 ± 4°. Therefore, the obtained contact angle of 73.5 ± 4° (<90°) on the stearic acid passivated, smooth ZnO surface (SA/ZnO) clearly indicates that the Wenzel model cannot explain the contact angle of 173 ± 1.1° observed on passivated ZnO nanotowers. The high superhydrophobicity of the ZnO nanotowers would be possible to explain considering the Cassie model [49], where the contact angle of water is determined by the contact angles on the composite structure of SA/ZnO and the trapped air between the nanotowers.

The Cassie-Baxter equation, which, as explained in Chapter 2, applies to a situation in which air is trapped beneath the drop in the interstices of the nanorough surface, is written as

$$\cos\theta_c = f_1 \cos\theta_1 + f_2 \cos\theta_2 \tag{4.1}$$

where $\theta_c$ is the CA on the composite coating consisting of two components with the CAs $\theta_1$ and $\theta_2$ and corresponding area fractions $f_1$ and $f_2$. In such a composite system, if *component 1* is assumed to be the solid surface and *component 2* is assumed to be air where $\theta_2$ is 180°, and as $f_1 + f_2 = 1$, Equation (4.1) can be written as

$$\cos\theta_c = f_1(\cos\theta_1 + 1) - 1 \tag{4.2}$$

Hence, for SA passivated ZnO nanotowers (composite of SA/ZnO and air) with $\theta_1 = 73°$ and $\theta_c = 173°$, the calculated $f_1$ contact fraction is ~0.006. Such a small value of $f_1$ confirms the existence of trapped air between the nanotowers that effectively leads to a very low contact angle hysteresis making the water drops roll off easily. Figure 4.1d shows

an image of a water drop captured on the surface of these ZnO nanotowers after SA passivation.

### 4.2.1 Effect of temperature on superhydrophobic properties

Fourier transform infrared (FTIR) and CA investigations were carried out to evaluate the stability of the organic molecules of SA on the superhydrophobic surfaces as well as to determine the thermal desorption temperature of the SA molecules.

FTIR spectra of the SA modified ZnO nanotowers confirm the presence of the $-CH_n$ groups of SA. Figure 4.3 shows the FTIR spectra of the samples, after annealing at different temperatures for 30 minutes, in the wavenumber range of 2550-3150 cm$^{-1}$ showing only the $-CH_n$ peaks of stearic acid. The two peaks at 2919 cm$^{-1}$ and 2850 cm$^{-1}$ belong to the asymmetric and symmetric C-H stretching modes of the $-CH_2$ groups of stearic acid respectively, and the peak at 2958 cm$^{-1}$ is assigned to the asymmetric in-plane C-H stretching mode of the $-CH_3$ group [143]. The ZnO peak was observed at 418 cm$^{-1}$ [116]. The three peaks of stearic acid remain nearly unchanged until 160 $^{\circ}$C with a drastic change occurring in their intensity at 200 $^{\circ}$C due to thermal desorption, and a continued decrease in intensity with increasing temperature.

Figure 4.4 shows the variation of the area under the peak at 2919 cm$^{-1}$ following annealing at different temperatures. The area under the peak is ~0.12 au.cm$^{-1}$ up to 160 $^{\circ}$C, falls to 0.04 au.cm$^{-1}$ at 200 $^{\circ}$C and becomes zero at 350 $^{\circ}$C. The inflection point of the curve of Figure 4.4 is found to be at 184 $^{\circ}$C by differentiation and is considered to be the thermal desorption temperature.
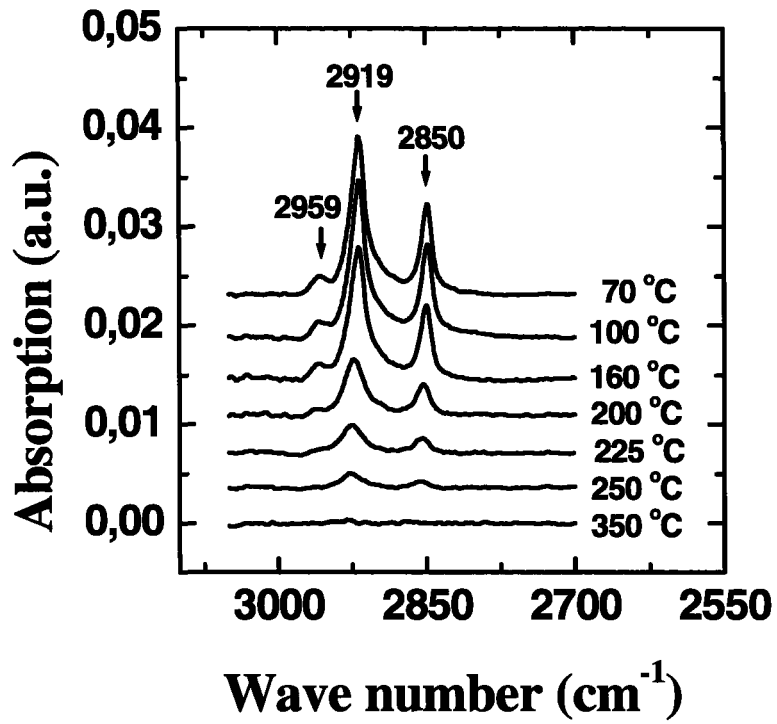
**Figure 4.3.** FTIR spectra showing $-CH_n$ peaks of stearic acid following annealing at various temperatures.

Figure 4.5 shows the contact angle and contact angle hysteresis data following annealing at elevated temperatures. The contact angle, as shown in the inset of Figure 4.5, remains >170° up to 160 °C and starts dropping with a minor decrease up to 250 °C at which point the contact angle is still >160°, showing superhydrophobicity. The contact

angle hysteresis (Figure 4.5) undergoes an increase with increasing annealing temperature, from 1.5° at 70 °C to 6° at 250 °C, although the water drops still roll off the surface easily. However, the contact angle continues to fall as the annealing temperature is increased.
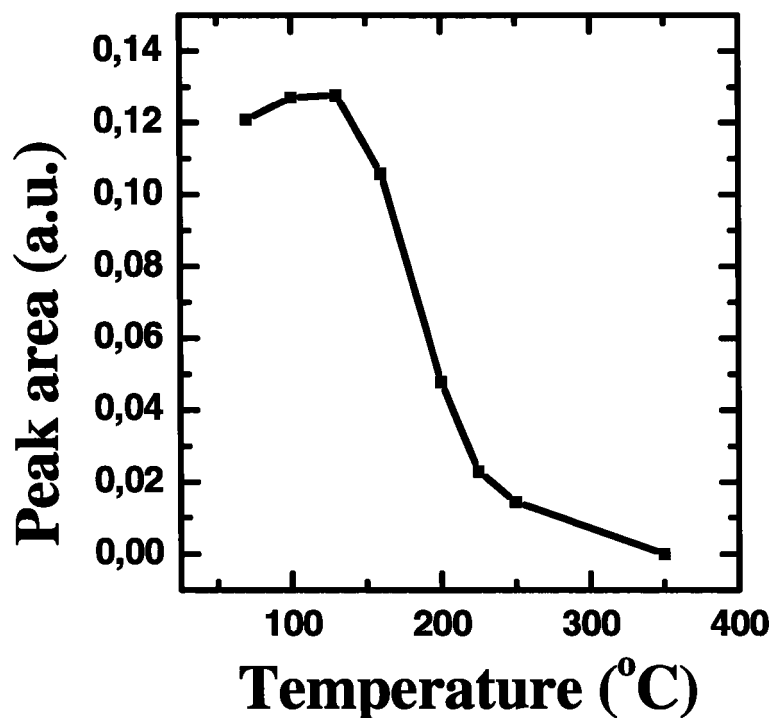


**Figure 4.4.** Variation of the area under the peak at 2919 cm$^{-1}$ as a function of the annealing temperature.
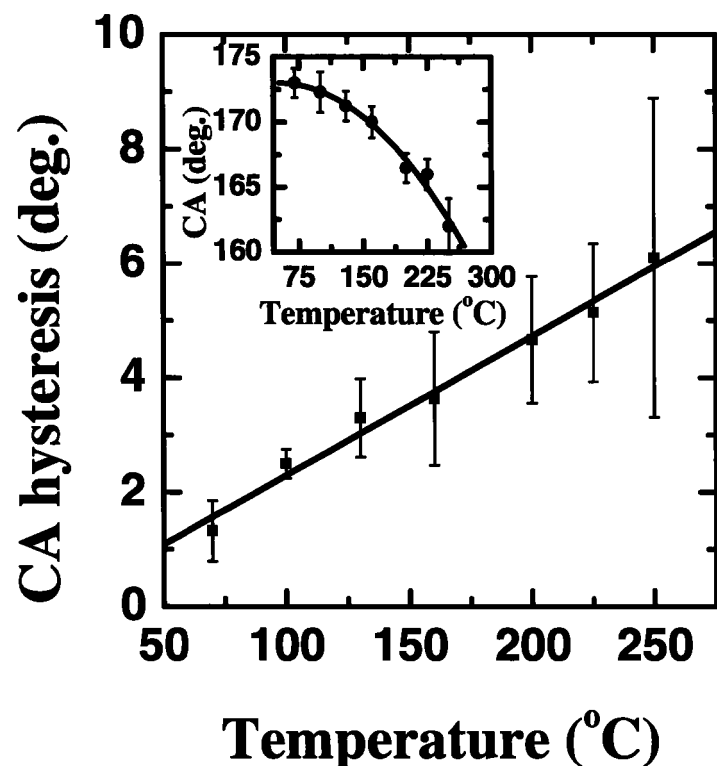
**Figure 4.5.** Contact angle hysteresis vs. annealing temperature. Inset shows contact angle vs. annealing temperature.

A strong correlation has been established between the thermal desorption of stearic acid and the loss of the superhydrophobic behavior of ZnO nanotowers. The nearly constant contact angle and very low contact angle hysteresis measured at room temperature

following an anneal at a temperature below160 °C observed in Figure 4.5 is due to the presence of a nearly constant coverage by stearic acid below the annealing temperature of 160 °C as observed in Figure 4.3. As the coverage of stearic acid starts to decrease above an annealing temperature of 184 °C as derived from the inflection point in Figure 4.4, the contact angle begins to decrease, with an increasing, although not inordinately large, contact angle hysteresis. Following annealing at 350 °C, the water drop spreads completely on the surface and the FTIR spectrum shows an absence of $-CH_n$ peaks. Due to the complete desorption of SA at 350 °C, the water drop interacts directly with the ZnO and the surface shows a hydrophilic character.

## 4.3 Summary and Conclusions

Superhydrophobicity was achieved on stearic acid passivated ZnO nanotowers, composed of several nanosteps on each nanotower, via a chemical bath deposition technique, providing a very high contact angle of ~173±1.1° with a very low contact angle hysteresis of ~1.4±0.5°. Water drops were found to roll off those surfaces even with the slightest angle of inclination. The thermal stability of the superhydrophobicity of these passivated ZnO nanotowers was studied by annealing them in air at elevated temperatures. The superhydrophobicity is found to deteriorate with increasing annealing temperature due to the thermal desorption of stearic acid that occurs at approximately 184 °C. These superhydrophobic ZnO nanotowers become hydrophilic by further annealing at 350 °C due to the complete desorption of SA at this temperature. It can be concluded that the

superhydrophobic properties of the ZnO nanotowers obtained following passivation with stearic acid are retained even at temperatures as high as 300 °C.

# CHAPTER 5

# NANOPATTERN FORMATION BY SUBSTRATE CHEMICAL ETCHING

## 5.1 Introduction

Superhydrophobicity was successfully achieved on SA passivated ZnO nanotower surfaces possessing a rough structure grown via the CBD technique [88]. However, the objectives of this thesis involve the evaluation of the ice adhesion strength on superhydrophobic dielectric surfaces and the study of the effect of the dielectric constant on ice adhesion. It was therefore necessary to prepare surfaces having different dielectric constants with similar surface roughnesses in order to eliminate the influence of the surface roughness on the ice adhesion strength. Moreover, not all the oxides can be prepared via CBD. While ZnO is easy to prepare via the CBD technique, it is not possible to prepare $TiO_2$ via CBD. Creating a certain roughness on the substrate surface and coating the rough surface with the preferred dielectric material can help solve the problem.

The formation or creation of micro-nanopatterns on a substrate surface results in a surface roughness that may lead to interesting properties. For example, substrate roughness has been investigated in many systems for its effect on wetting and adhesion [145]. Examples of such surfaces include water-repellent insect legs such as those of the water strider [55], the setae on the feet of geckos [146], and engineered self-cleaning glass [47]. Micrometer- and nanometer-scale patterns, formed by merging chemistry and fabrication,

are indispensable and ubiquitous in a range of applications such as electronic devices [147,148], electro-optical devices [149], (bio)chemical sensors [150], etc.

So, how can a pattern be created on a substrate surface? Common techniques recently used in pattern creation include lithography techniques, block copolymer and polymer masking, pattern creation using an AFM tip and so on [151-155]. These techniques use complex procedures and are rather expensive. Etching is a common method used to create random or ordered patterns on a substrate. Etching basically refers to the removal of material from a surface via wet or dry processes. In dry etching, the material is sputtered or removed using reactive ions or a vapor phase etchant. In wet etching, the material is dissolved when immersed in a chemical solution. Wet etching or chemical etching, however, is a simple technology which requires only a container with a liquid solution that will dissolve the material in question. The choice of a proper etchant and the etching parameters such as the etchant concentration, temperature of etchant, etc., are important factors in substrate chemical etching.

For example, the wet chemical etching of silicon in strongly anisotropic etchants such as aqueous potassium hydroxide (KOH) is used for the fabrication of three-dimensional microstructures on silicon wafers [156]. KOH is one of the most commonly used silicon etchants for micromachining silicon wafers [156-158]. The other etchants used are tetramethylammonium hydroxide (TMAH), $NH_4F$ [159], NaOH [160] etc. The KOH etch rate strongly depends on the crystallographic orientation of the silicon [161]. The etch rate distribution for different planes has been measured by several authors as a function of the temperature and of the face of the silicon monocrystal [162].

Aluminum is another common material usually patterned by two methods: (i) conventional photolithography, followed by metal deposition and liftoff; (ii) reactive ion etching (RIE) of a continuous film, a procedure that also involves a step of photolithography for pattern definition [163]. In the case of metal deposition followed by liftoff, the pattern is transferred by the physical removal of the aluminum in the unwanted regions by dissolution of an underlying polymer. No etching of the aluminum occurs; for larger features, however, complete removal of the unwanted aluminum can be difficult. Conventional photolithography requires access to appropriate facilities and is not always convenient, nor is it applicable to curved surfaces. The chemical etching technique is a non-photolithographic procedure for patterning aluminum. Common ingredients for chemically etching aluminum include different combinations of ammonium bifluoride, chromic acid, sodium hydroxide, hydrochloric acid, and hydrofluoric acid.

In this study, chemically etched substrates of Si (100) and Al were coated with thin films of the dielectrics ZnO and $TiO_2$ using sol-gel spin-coating processes. Si (100) was initially used to understand the formation of nanopatterns by etching with KOH. However, for ice adhesion studies, as it was necessary to drill holes in the substrates as described in Chapter 3 (Experiment) for the CAT tests, Al was chosen as the substrate material. HCl was used as the etchant to create nanopatterns on Al following an oxidation process using an oxygen plasma to obtain nanorough $Al_2O_3$ substrates. The nanorough dielectric surfaces were passivated to lower their surface energies and to impart superhydrophobic properties.

In this chapter, the surface characterization and the wetting characteristics of the nanorough dielectric surfaces prior to and following passivation will be summarized.

## 5.2 Surface characterization

### 5.2.1 Morphological analyses

**5.2.1.1 Formation of nanopatterns on Si (100) surfaces:** Figure 5.1 shows the FESEM image of a Si (100) surface following etching with 0.1M KOH solution while the inset of Figure 5.1 shows the same before etching. The SEM image reveals the morphological features of the rough micro-pyramidal nanopatterns formed following etching. The base of the Si micro-pyramids is ~3-4 µm in size with heights of ~3.5-4 µm. The distances between the Si pyramids are random due to the anisotropic etching behavior of Si in aqueous KOH.
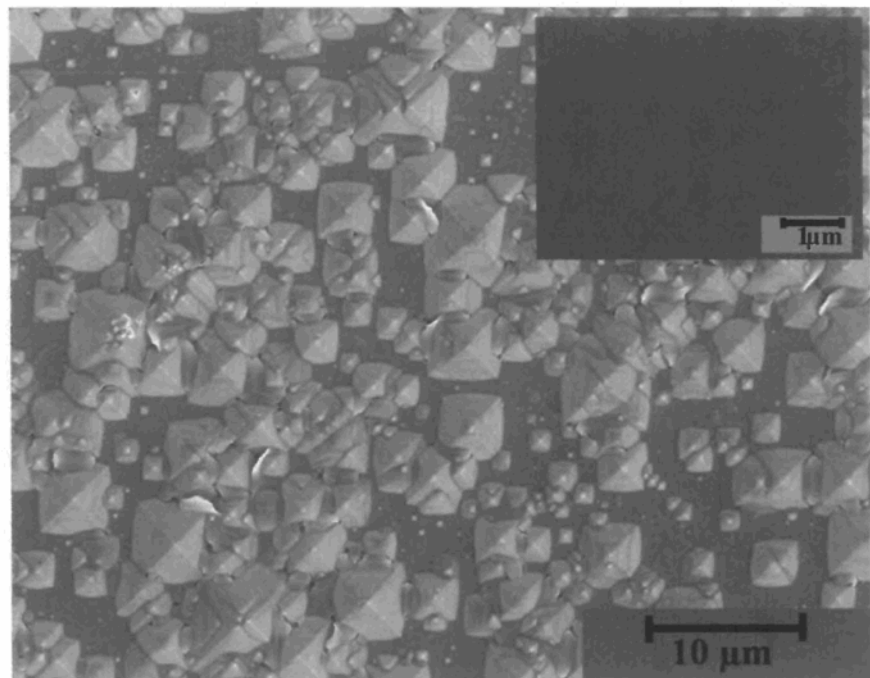


**Figure 5.1.** FESEM image of nanopatterned Si (100) created by KOH etching; inset shows the Si (100) surface before etching.

**5.2.1.2 Formation of nanopatterns on Al surfaces:** Figure 5.2 shows the FESEM image of an Al surface etched in 40% HCl and the inset of Figure 5.2 shows the Al surface prior to etching. The formation of a rough coral-like nanopattern following etching is evident from the SEM images.
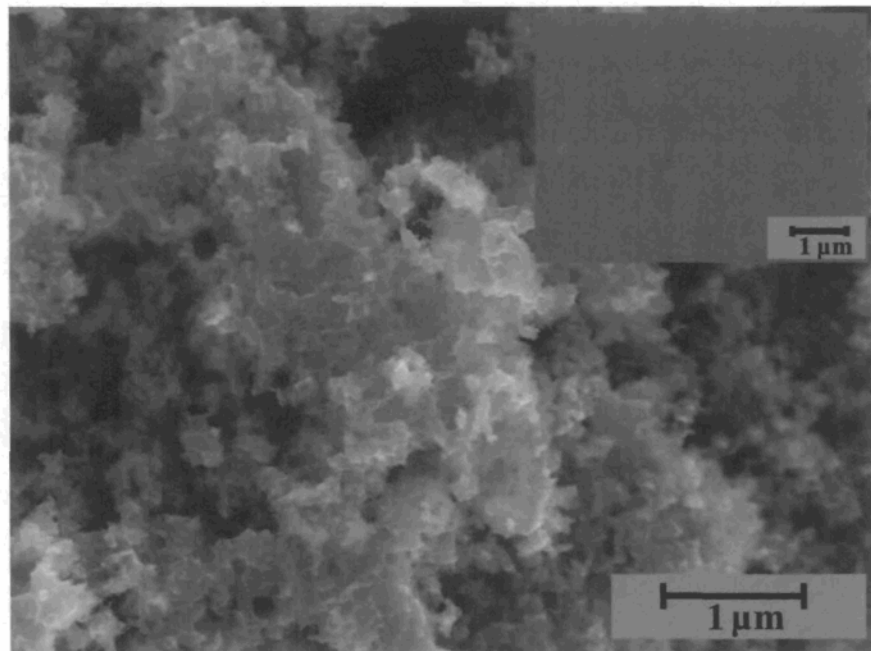


**Figure 5.2.** FESEM image of nanopatterned Al created by HCl etching; **inset** shows the Al surface before etching.

**5.2.1.3 Dielectric coatings of ZnO and TiO$_2$ on the nanorough substrates**

Before coating the dielectrics on nanorough substrates of Si (100) or Al$_2$O$_3$, it is important to obtain dielectric coatings of lower roughnesses on a flat surface in order to

compare the wetting behavior on the nanorough substrates. Therefore, flat Si (100) substrates were initially coated individually with the dielectrics of ZnO and $TiO_2$ by sol-gel spin-coating processes as described in Chapter 3 (Experiment). Figure 5.3 shows the 1×1 μm scan size AFM images of the two dielectric surfaces of similar roughness obtained following the optimization of the process parameters, for example, the concentration of the dielectric sols, ageing time of the sols, spin parameters, etc. The AFM images reveal the uniformity of the two coatings and the AFM analyses showed that both the dielectric coatings of ZnO and $TiO_2$ posses a root-mean-square (*rms*) roughness as low as ~2 nm.
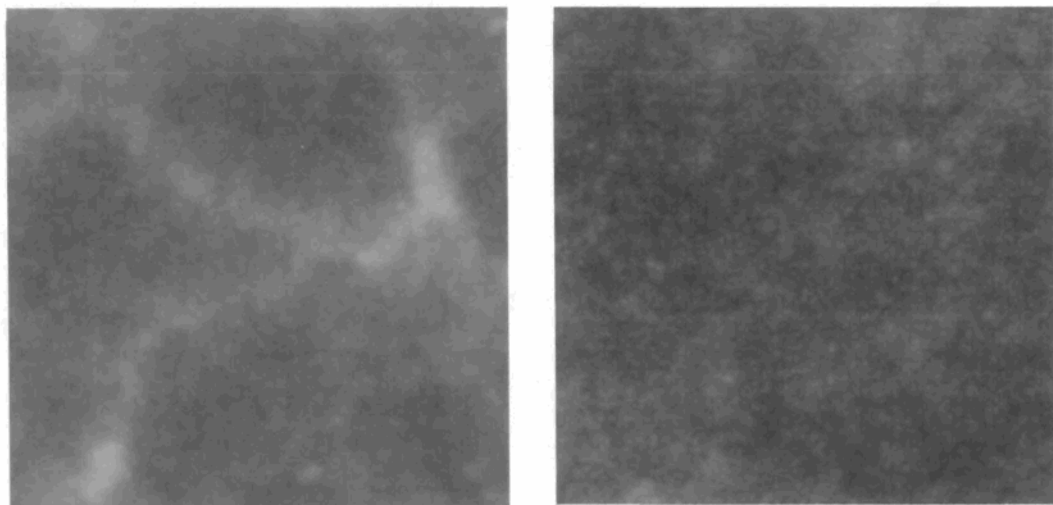


**Figure 5.3.** 2D AFM images of scan size 1×1 μm of (a) ZnO and (b) $TiO_2$ on flat Si.

ZnO and $TiO_2$ were then coated on the nanorough $Al_2O_3$ surfaces. The presence of a layer of either of the dielectric coatings on the rough substrate surface is found to retain the

morphological features of the substrate surface. This observation is evident from FESEM images of both the dielectric films on either of the nanorough substrates (Si or $Al_2O_3$) as shown in Figure 5.4 (ZnO in Figure).
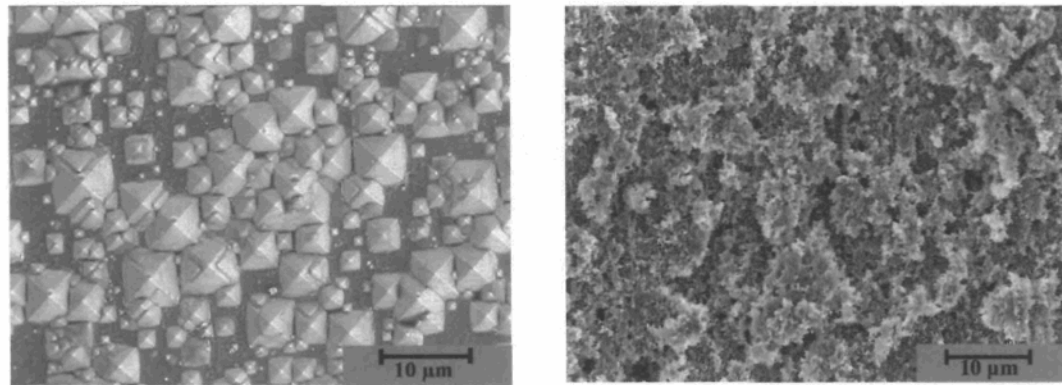


**Figure 5.4.** SEM images of dielectric (ZnO in Figure) coated nanopatterned (a) Si (100) and (b) $Al_2O_3$ surfaces.

### 5.2.2 Chemical analyses

### 5.2.2.1 XPS analysis of the nanorough dielectric surfaces:

Dielectric coatings of ZnO and $TiO_2$ were applied separately on the nanorough substrates of Si (100) and $Al_2O_3$. The presence of ZnO and $TiO_2$ were confirmed from the XPS spectra of the two oxides on both substrates. The XPS analysis of dielectric coated nanorough Si (100) will be discussed in the following sections.

**Nanorough ZnO surface:** Figure 5.5 shows the high resolution peaks of $Zn2p_{3/2}$ and O1s (in inset). The binding energy of the $Zn2p_{3/2}$ peak was 1021.6 eV [164]. The O1s spectrum shows two distinct peaks located at 530.28 eV and 532.0 eV. The O1s peak at

lower binding energy corresponds to ZnO [165] and the peak at the higher binding energy

corresponds to $SiO_2$ and possibly zinc hydroxide. The presence of a strong O1s peak at a

higher binding energy may be due to the partial coverage of ZnO on the etched surfaces. Si

peaks were observed in the survey spectrum at 99 eV and 103 eV.
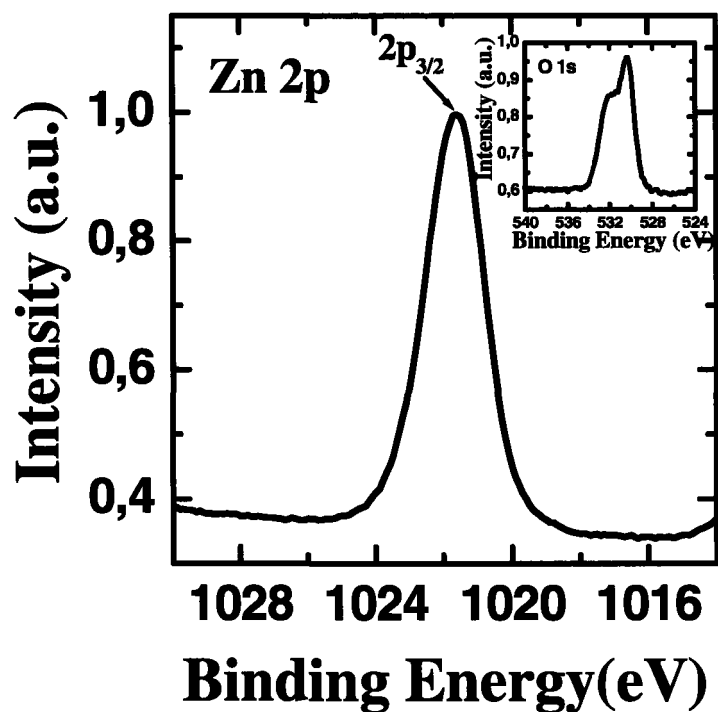


**Figure 5.5.** XPS high resolution Zn2p spectrum and O1s (**inset**) spectrum of ZnO-coated nanorough silicon.

**Nanorough TiO₂ surface:** Figure 5.6 shows the high resolution peaks of Ti2p and

O1s (in inset) of $TiO_2$ coated on a nanopatterned Si (100) substrate. The binding energies of

the $Ti2p_{3/2}$ and $Ti2p_{1/2}$ peaks are 458.85 eV and 464.53 eV, respectively. The O1s peak

shows a main component at the lower binding energy of 530.1 eV and a shoulder at a

higher binding energy of 531.88 eV [152,166].
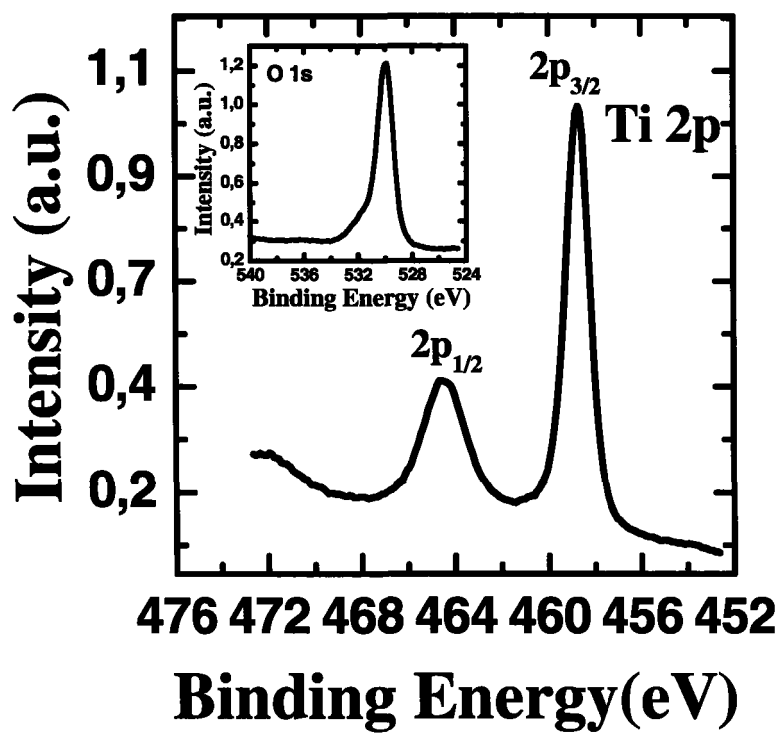


**Figure 5.6.** XPS high resolution Ti2p and O1s (inset) spectra of $TiO_2$-coated nanorough silicon.

### 5.2.2.2 XPS analysis of the passivated nanorough dielectric surfaces:

The surfaces of the nanorough dielectric coatings were passivated to lower the surface energy with a view to obtaining superhydrophobicity. Two methods of passivation were used: (i) by immersing the oxide-coated samples in a solution containing FAS-17; and (ii) by coating rf-sputtered Teflon® onto the surfaces of the nanorough dielectric films using a plasma technique. XPS analysis carried out on both the dielectric surfaces passivated by both methods will be discussed in the following section.

**FAS-17:** The C1s core level spectrum of a surface passivated with FAS-17 is shown in Figure 5.7, resolved into seven components namely $-CF_3$ (293.47 eV), $-CF_2$ (291.25 eV), $-CH_2-CF_2$ (289.10eV), $-C-O$ (286.21 eV), $-C-C$ (285 eV), $-C-Si$ (282.97 eV) and $-C-$Metals (280.91 eV). The inset of Figure 5.7 shows the high resolution F1s spectrum from FAS-17 having a F1s binding energy of 688.5 eV. Table 5.1 summarizes the relative proportions of all seven components resolved from the C1s peak fit. The ratio of $CF_3$/Si from the spectra was found to be 0.94 compared to 1 in the FAS-17 molecule. The $CF_3$/$CF_2$ ratio from the C1s spectrum was found to be 0.20, compared to a ratio in the FAS-17 molecule of 0.14. The higher $CF_3$/$CF_2$ ratio observed in the spectrum, in contrast to other reports indicates that the FAS-17 molecules are oriented in such a way that their $CF_3$ head groups are preferentially aligned away from the surface of the dielectric [167]. Moreover, the $CF_3$ and $CF_2$ concentrations from the spectra which are 10.86% and 52.21%, respectively, are higher than the theoretical values obtained from the molecular structure, which are 6% and 41%, respectively, indicating that the low surface energy $CF_3$ and $CF_2$ components comprise the outermost surface of the passivation coating.
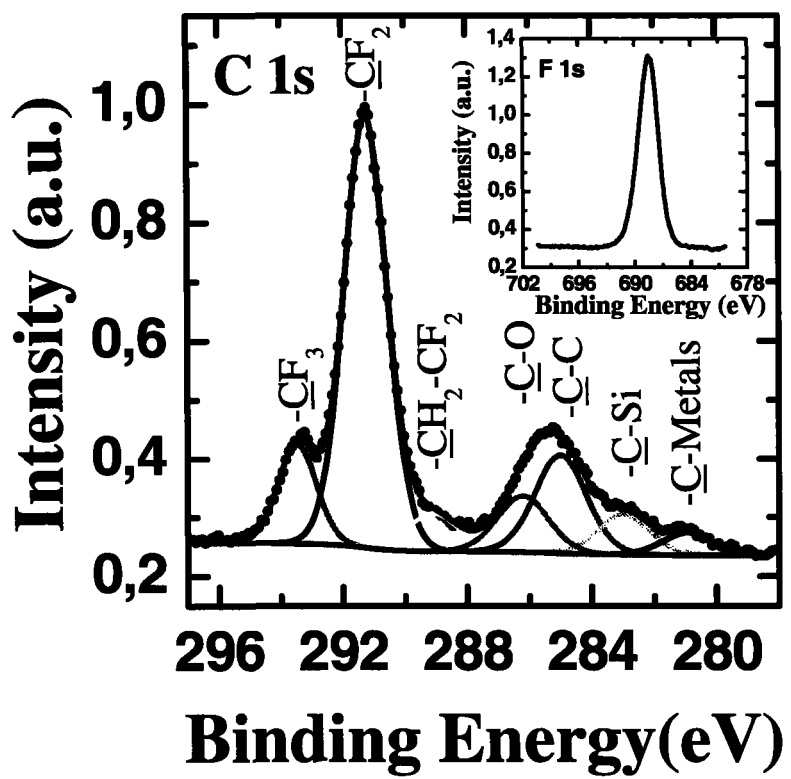
**Figure 5.7.** XPS high resolution spectra of C1s and F1s (**inset**) of an FAS-17 coating.

**Table 5.1.** Summary of C1s peak fitting of FAS-17.

| Component | BE (eV) | Conc (%) | Theoretical Conc (%) |
|---|---|---|---|
| C1s (-$\underline{C}F_3$) | 293.47 | 10.86 | 6 |
| C1s (-$\underline{C}F_2$) | 291.25 | 52.21 | 41 |
| C1s (-$\underline{C}H_2$-$CF_2$) | 289.10 | 5.462 | 6 |
| C1s (-$\underline{C}$-O) | 286.21 | 8.102 | 18 |
| C1s (-$\underline{C}$-C) | 285.00 | 14.3 | 24 |
| C1s (-$\underline{C}$-Si) | 282.97 | 5.802 | 6 |
| C1s (-$\underline{C}$-Metals) | 280.91 | 3.268 | - |

**Rf-sputtered Teflon®:** Figure 5.8 shows the C1s core level spectrum of rf-sputtered Teflon® resolved into seven components: $-CF_3$ (293.50 eV), $-CF_2$ (291.43 eV), $-CF-CF_n$ (289.35 eV), $-C-F$ (287.84 eV), $-C-CF_n$ (286.92 eV), $-C-C$ (285 eV) and $-C$-Metals (283.20 eV). The relative proportions of all seven components resolved from the C1s peak fit are summarized in Table 5.2. The higher concentration of the low-energy surface energy groups $-CF_3$ (22.35%) and $-CF_2$ (37.66%) in contrast to other reports, which hardly chow any $CF_3$ peaks ,indicates that more of those components are oriented outward from the surface [168,169]. The binding energy of F1s from rf-sputtered Teflon® as shown in the inset of Figure 5.8 was at 688.5 eV.
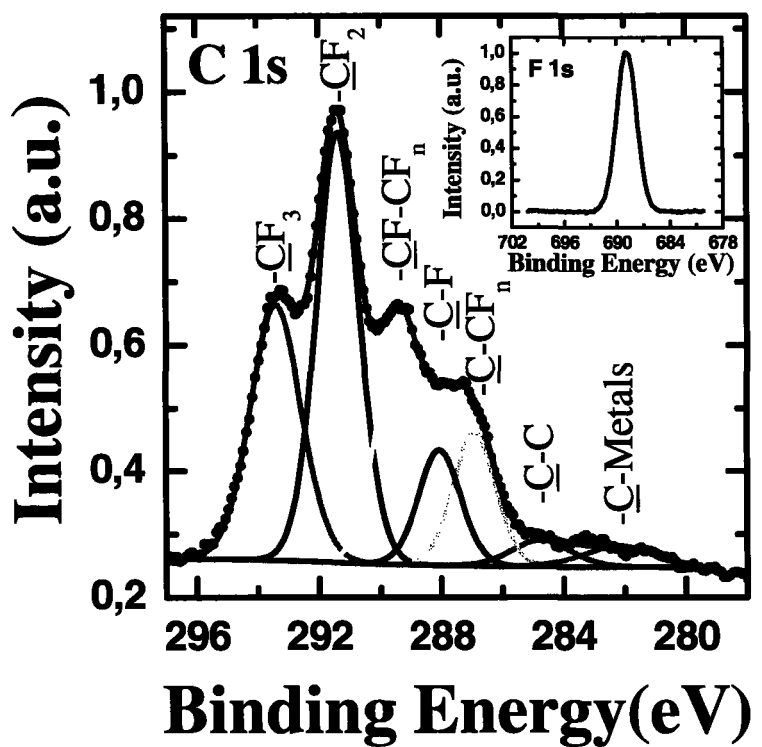
**Figure 5.8.** XPS high resolution spectra of C1s and F1s (**inset**) of an rf-sputtered Teflon® coating.

**Table 5.2.** Summary of C1s peak fit of rf-sputtered Teflon®.

| Component | BE (eV) | Conc (%) |
|---|---|---|
| C1s (-$\underline{C}F_3$) | 293.50 | 22.35 |
| C1s (-$\underline{C}F_2$) | 291.43 | 37.66 |
| C1s (-$\underline{C}F$-$CF_n$) | 289.35 | 19.83 |
| C1s (-$\underline{C}$-F) | 287.84 | 7.65 |
| C1s (-$\underline{C}$-$CF_n$) | 286.92 | 9.98 |
| C1s (-$\underline{C}$-C) | 285 | 1.11 |
| C1s (-$\underline{C}$-Metals) | 283.20 | 1.41 |

### 5.2.3 Hydrophobicity

The dielectric coatings of ZnO and $TiO_2$ on flat and nanorough substrates of Si (100) and $Al_2O_3$ were tested for hydrophobicity via contact angle measurements prior to and following surface passivation. The contact angle data obtained on the two dielectrics on different substrates is tabulated in Tables 5.3 and 5.4.

**Table 5.3.** Contact angle data on ZnO coated onto different substrates.

| Substrate | ZnO (Contact angle and contact angle hysteresis in degrees) | | | | | |
|---|---|---|---|---|---|---|
| | Contact angle | | | Contact angle hysteresis | | |
| | Un-passivated | FAS-17 passivated | Rf-sputtered Teflon® coated | Un-passivated | FAS-17 passivated | Rf-sputtered Teflon® coated |
| Flat Si | 17 ± 1 | 123 ± 1 | 127 ± 1 | *** | *** | *** |
| Etched Si | 18 ± 2 | 150 ± 1 | 152 ± 4 | Absorbed | 15 ± 1 | 17 ± 1 |
| Flat $Al_2O_3$ | 31 ± 2 | 124 ± 0.3 | 126 ± 2 | *** | *** | *** |
| Etched $Al_2O_3$ | Absorbed | 161 ± 2 | 162 ± 2 | Absorbed | 2 ± 0.5 | 1 ± 0.5 |

***These data were unobtainable

**Table 5.4.** Contact angle data on $TiO_2$ coated onto different substrates.

| Substrate | $TiO_2$ (Contact angle and contact angle hysteresis in degrees) | | | | | |
|---|---|---|---|---|---|---|
| | Contact angle | | | Contact angle hysteresis | | |
| | Un-passivated | FAS-17 passivated | Rf-sputtered Teflon® coated | Un-passivated | FAS-17 passivated | Rf-sputtered Teflon® coated |
| Flat Si | 19 ± 1 | 129 ± 4 | 124 ± 1 | *** | *** | *** |
| Etched Si | 39 ± 3 | 150 ± 2 | 156 ± 1 | *** | 19 ± 2 | 17 ± 3 |
| Flat $Al_2O_3$ | 43 ± 1.5 | 126 ± 1 | 123 ± 1.5 | *** | *** | *** |
| Etched $Al_2O_3$ | 25 ± 0.1 | 165 ± 1 | 163 ± 2 | *** | 4 ± 0.6 | 2 ± 1 |

***These data were unobtainable

All of the as-deposited dielectric surfaces studied, either flat or rough, which had no passivation layer demonstrated hydrophilicity irrespective of the type of oxide coated and the substrate used. The contact angles of water on all those surfaces were below 50°. However, on applying a passivation layer, of either FAS-17 or rf-sputtered Teflon®, the water contact angles were found to increase leading to hydrophobic and superhydrophobic properties depending on the roughness of the surface. A surface is hydrophobic when the water contact angle is above 90° and superhydrophobic when the water contact angle is above 150°. The flat dielectric surfaces when passivated provided contact angles of below 150° but above 90° and therefore demonstrate hydrophobicity. However, the water drops on those surfaces stuck to the surface making it impossible to measure the contact angle hysteresis. On the other hand, the water contact angles obtained on nanorough dielectric surfaces following passivation are greater than 150° demonstrating superhydrophobic properties. The highest contact angles of >160° and lowest contact angle hystereses of <5° were obtained on passivated dielectric coated nanorough $Al_2O_3$ surfaces. The contact angles

obtained on passivated dielectric coated nanorough Si ($\sim$150° - 156°) are slightly lower. Although the water drops rolled off those surfaces easily with slight incline of the sample surface, the contact angle hysteresis was higher ($\sim$15° -19°) on the passivated dielectric coated nanorough Si (100) surface than on passivated dielectric coated nanorough $Al_2O_3$ (<5°).

The difference in the contact angle hysteresis in the two cases could be attributed to the difference in the amount of air entrapment in the rough structures of the surfaces. Table 5.5 shows the area fraction $f$ for the different dielectric surfaces in contact with the water drop after passivation as calculated from the Cassie-Baxter equation [49] written as $\cos\theta' = f(\cos\theta + 1) - 1$ where $\theta'$ is the apparent contact angle obtained on the rough surface and $\theta$ is the contact angle obtained on the flat surface. The $\theta'$ and $\theta$ values are taken from Tables 5.3 and 5.4. The $f$ values obtained on passivated dielectric coated nanorough Si are $\sim$0.3 and higher compared to the fraction of only $\sim$0.1 obtained on passivated dielectric coated nanorough $Al_2O_3$. The true surface area, compared to the geometric surface area, formed as a result of etching Si could be lower than that on etched Al, leading to a lower entrapment of air and a greater contact fraction as determined from the Cassie-Baxter equation.

Regardless of the type of dielectric coating (ZnO or $TiO_2$), in all cases it is obvious that the addition of a low energy coating on the surfaces enhances the hydrophobicity by providing a greater contact angle as compared to those samples without a passivation layer. Adding nanoroughness to a hydrophobic surface leads to superhydrophobicity. The low area fraction $f$ of the solid and the water drop results in a large amount of air entrapment in

the rough structure of the surface leading to the highest water contact angles and the lowest

contact angle hystereses. Therefore, from the contact angle measurements (Tables 5.3 and

5.4), it is evident that the two most important factors in obtaining a very high CA and a

very low CAH are the nanopatterns created on the substrate, that govern the geometry of

the surface, and the presence of a low surface energy passivation layer which optimizes the

chemistry of the surface. Therefore, the contact area of the water drops with a surface can

be considerably reduced with these two criteria fulfilled, irrespective of the type of oxide

coating present on the substrate. Moreover, the area fraction $f$ of the surface in contact with

the water drop must be very small as compared to the fraction of the water drop in contact

with the air entrapped in the geometrically patterned surface [26,49] in order to obtain

superhydrophobic properties. Therefore, the optimization of the geometry of the surface

must be based on obtaining a smaller $f$-factor in order to achieve superhydrophobicity.

**Table 5.5.** Fraction ($f$) of the surface in contact with the water drop as calculated from the
Cassie equation.

| Samples | Area fraction "$f$" |
|---|---|
| FAS-17 passivated ZnO/nanopatterned Si (100) | 0.33 |
| rf-sputtered Teflon® coated ZnO/ nanopatterned Si (100) | 0.30 |
| FAS-17 passivated ZnO/ nanopatterned $Al_2O_3$ | 0.12 |
| rf-sputtered Teflon® coated ZnO/ nanopatterned $Al_2O_3$ | 0.12 |
| FAS-17 passivated $TiO_2$/ nanopatterned Si (100) | 0.36 |
| rf-sputtered Teflon® coated $TiO_2$/ nanopatterned Si (100) | 0.20 |
| FAS-17 passivated $TiO_2$/ nanopatterned $Al_2O_3$ | 0.08 |
| rf-sputtered Teflon® coated $TiO_2$/ nanopatterned $Al_2O_3$ | 0.09 |

Ice adhesion tests (Chapter 6) were subsequently carried out on the hydrophilic, hydrophobic as well as the superhydrophobic passivated dielectric surfaces, which were characterized by morphological and chemical compositional studies prior to and following the ice tests. Due to the reduced contact area of water drops on the superhydrophobic surfaces, it is expected that ice also will have less adherence to those surfaces. These results will be discussed in Chapter 6.

## 5.3 Summary and Conclusions

Superhydrophobic nanorough dielectric surfaces of ZnO and $TiO_2$ were obtained via the wet chemical etching of the Si or Al substrate surfaces. Morphological analyses by FESEM confirmed the presence of a rough nanostructure on the substrates of Si (100) as well as $Al_2O_3$ following etching. FESEM images also showed that a coating of the dielectric of either ZnO or $TiO_2$ did not alter the surface morphology of the rough substrates. XPS analyses confirmed the presence of the dielectric coatings on the rough substrates. The FAS-17 and rf-sputtered Teflon® passivating coatings on the nanorough dielectric surfaces were also investigated by XPS. The higher apparent concentration of low surface energy groups $-CF_3$ and $-CF_2$ in both FAS-17 and rf-sputtered Teflon® coatings indicates that more of those components are oriented outward on the surface apparently leading to superhydrophobic properties. The lowest contact angle hysteresis ($<5°$) and highest contact angle ($>160°$) was achieved on passivated dielectric coated nanorough $Al_2O_3$ surfaces. A slightly lower contact angle ($\sim150°$-$156°$) and higher contact angle hysteresis ($\sim15°$ -$19°$) was obtained on nanorough Si (100) substrates coated with

passivated dielectrics. The cause for the difference is attributed to the higher fraction of the solid surface $f$ of ~0.3 in contact with the water drop in the case of Si (100) substrates as compared to a fraction $f$ of 0.1 in the case of $Al_2O_3$ substrates indicating a larger amount of air entrapment in the case of $Al_2O_3$ substrates. Therefore, morphological analyses, chemical analyses and hydrophobicity tests show that a low energy surface with a certain nanoroughness leading to the lowest $f$-value leads to highly superhydrophobic surfaces with very high contact angles and very low contact angle hystereses.

# CHAPTER 6

## ICE ADHESION

### 6.1 Introduction: Adhesion strength of ice – an overview

Ice adheres strongly to almost all kinds of surfaces. It is a known fact that the strong adhesion of ice to various surfaces such as aircraft parts, streets and side-walks, automobile windshields, conducting cables and insulator surfaces poses a major inconvenience or even a significant danger. Removing the stuck ice from a surface is not an easy task. The adhesion strength of ice on surfaces such as steel or aluminum can vary from ~0.03 MPa to ~2 MPa depending on the test conditions and the roughness of the surface [153]. Mechanical and chemical methods that are currently in use to remove such strongly adhered ice cause great damage to surfaces and are mostly expensive (See Chapter 1 "Introduction"). Therefore, in this study, an effort was made in preventing ice from adhering to substrate surfaces or in minimizing the strength of adhesion of ice to the surfaces by applying icephobic coatings.

An appropriate test method would be an important asset to evaluate the adhesion strength of ice to such coatings in order to estimate the icephobic nature of the coating applied. There is a gap in the literature on the methods of evaluation of ice adhesion strengths on different coatings, particularly with samples as small as 2.5 × 2.5 cm$^2$ used in the experiments of the current research. Jellinek *et al.* [170] used a "sandwich" technique to

study the adhesive and cohesive strength of snow-ice sandwiched between polished circular 304 stainless steel plates approximately 0.3 cm apart. Shear stresses developed from torsional loads provide the adhesion strength values [171]. Techniques such as cone tests used at the CRREL Laboratory, employ an apparatus typically used to evaluate the performance of adhesive joints [118]. In this test, ice is used as an adhesive to bond concentric cones of variable angle and then an axial load is applied to pull the cones apart [119]. By varying the cone angle, the relative amounts of shear and tension being applied to the adhesive joint is controlled. Another test by Archer and Gupta [119] measures the adhesion strength of ice coatings on structural surfaces, in which a laser-induced compressive stress pulse travels through a 1 mm-thick substrate disc that has a layer of ice grown on its front surface. The compressive stress pulse reflects into a tensile wave from the free surface of the ice and pulls the ice interface apart, given a sufficient amplitude. The interface strength is calculated from the free surface velocity of an Al substrate using a Doppler interferometer and calculating the stress at the interface using a finite-difference elastic wave mechanics simulation with the free surface velocity as an input [120]. These techniques are highly expensive tools and use quite complicated procedures and are not suitable for samples of smaller dimensions. A relatively simple technique employing a rotating rotor centrifugal force was first introduced by Beams *et al.* [172] in 1955 to measure the adhesive and tensile strength of thin films of ice on metals. The same method was used by Raraty and Tabor [173] to measure the adhesive shear strength of ice, on polished, cleaned stainless steel. LIMA-AMIL, UQAC [121] used the same principle and developed an apparatus called the centrifugal adhesion reduction test (CAT), in which iced

samples are rotated at high speed in a centrifugal chamber and the shear adhesion strength is determined by measuring the centrifugal force which causes a shear failure and detaches the ice from the sample's surface. Due to the simplicity of the procedure used in this technique, CIGELE labs also developed a CAT apparatus in one of its cold chambers. Another simple test was also developed at the CIGELE labs – a pulling test, in which the force required to mechanically detach the ice is determined by pulling the ice vertically from the surface of the sample. The details of the two tests have been described in Chapter 3 (Experiment). Morphological and chemical compositional studies as well as hydrophobicity tests were performed on the ice-tested hydrophilic and superhydrophobic coatings and compared with those prior to ice adhesion tests to evaluate the re-usability of the icephobic coating. These tests have been performed using SEM/EDX, XPS and CA goniometry. The ice adhesion strengths on the various surfaces studied will be discussed in this chapter followed by a discussion of the surface characterizations. The ice adhesion strengths determined by both pulling tests and CAT tests and the ARF of the CAT tested samples in comparison with their water contact angles and contact angle hystereses have been tabulated in a single table, Table 6.1, in order to avoid repetition.

## 6.2. Ice adhesion results

**6.2.1 Pulling test:** In this method, ice adhesion tests were performed by measuring the force of debonding of ice from the ice-dielectric interfaces by mechanically pulling ice from the sample surface (detailed in chapter 3 - Experiment). Bare Al was used as a standard reference, confirming the adhesion strength of ice on bare Al to be $450 \pm 43$ kPa

following several test runs. This value is comparable to the ice adhesion strength determined by other methods reported in the literature [17,121,122].

The ice adhesion strength (Table 6.1) on dielectric-coated flat Al surfaces was found to be $431 \pm 43$ kPa for ZnO and $319 \pm 71$ kPa for $TiO_2$. On nanorough dielectric surfaces, the adhesion strengths were similar: $478 \pm 56$ kPa for ZnO and $375 \pm 86$ kPa for $TiO_2$. In both cases, however, $TiO_2$ shows a lower adhesion strength than ZnO. According to the concept of image charges [20], ZnO should show a lower adhesion strength and the reason for such an inverse behavior is unknown. Factors such as hydrogen bond and dipolar interaction also play an important role in bonding between ice and the substrate, which have not been taken into account in this study. However, regardless of this difference, these values may be assumed to be similar to and comparable with the adhesion strength of ice on bare Al, taking the measurement errors into consideration.

The behavior was different when the surfaces of uncoated and dielectric-coated aluminum substrates were coated with rf-sputtered Teflon®. The ice slid off those surfaces during the separation of the thermocoal mold used to grow the ice on those surfaces. The adhesion strength of ice on these surfaces was difficult to measure as the ice debonded spontaneously from these surfaces without application of force (Figure 6.1). The adhesion strength in this case was therefore considered to be zero. This technique is therefore more suitable for the measurement of the adhesion strengths of ice on hydrophilic samples than on superhydrophobic samples.

The tests were also performed on various surfaces passivated with FAS-17 which showed a behavior similar to the rf-sputtered Teflon® coated surfaces. Therefore, those values have not been discussed here.

**Table 6.1.** Ice adhesion strength by pulling and CAT tests on various surfaces and ARF of CAT tested surfaces as compared with their water contact angles.

| Samples | Adhesion Strength (kPa) | | ARF (CAT) | CA (°) | CAH (°) |
|---|---|---|---|---|---|
| | Pull test | CAT test | | | |
| Bare Al | 369±89 | 420±27 | 1 | 161 ± 3 | 2 ± 1.2 |
| Tef/Al | 45±22 | 188±12 | 2.23 | 116 ± 2.5 | High |
| nrAl | 444±32 | 466±122 | 0.90 | Absorbed | *** |
| Tef/nrAl | *** | 133±136 | 3.16 | 165 ± 2 | 2.5 ± 1.5 |
| ZnO/Al$_2$O$_3$ | 431±43 | 450±101 | 0.93 | 33 ± 2 | *** |
| Tef/ZnO/Al$_2$O$_3$ | 45±0 | 158±41 | 2.66 | 120 ± 2.5 | *** |
| ZnO/nrAl$_2$O$_3$ | 478±56 | 482±125 | 0.87 | *** | *** |
| Tef/ZnO/nrAl$_2$O$_3$ | *** | 66±38 | 6.36 | 162 ± 3 | 2 ± 0.5 |
| TiO$_2$/Al$_2$O$_3$ | 319±71 | 460±75 | 0.91 | 36 ± 2 | *** |
| Tef/TiO$_2$/Al$_2$O$_3$ | 34±19 | 138±18 | 3.04 | 121 ± 3 | *** |
| TiO$_2$/nrAl$_2$O$_3$ | 375±86 | 480±60 | 0.88 | *** | *** |
| Tef/TiO$_2$/nrAl$_2$O$_3$ | *** | 122±30 | 3.44 | 163 ± 2.5 | 2 ± 1.5 |

***These data were unobtainable; Tef stands for rf-sputtered Teflon®, nrAl and nrAl$_2$O$_3$ stand for nanorough Al and nanorough Al$_2$O$_3$, respectively.
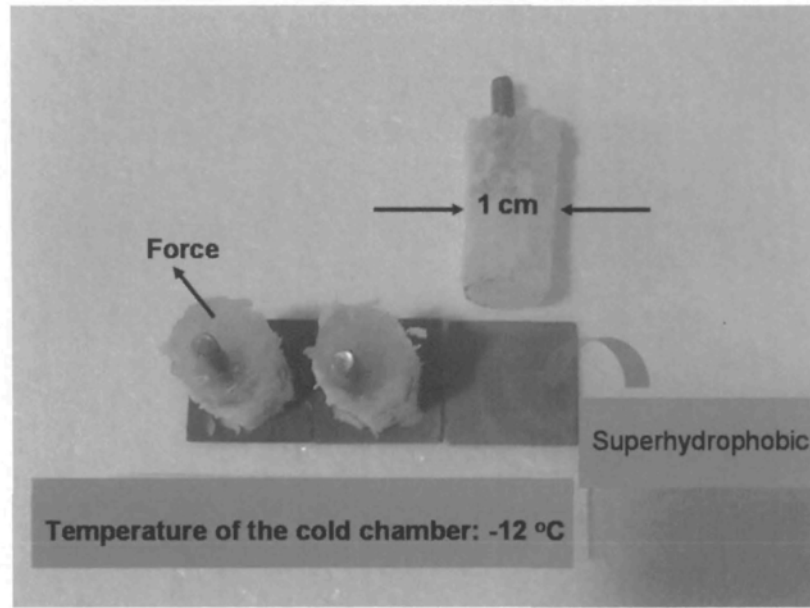
**Figure 6.1**. Photograph of the ice cylinders formed on the unpassivated dielectrics as compared to the superhydrophobic rf-sputtered Teflon® coated dielectrics (ZnO in Figure).

Another test method, a home made centrifugal ice adhesion reduction test (CAT) apparatus, was used to further investigate the effect of the dielectric constant on ice adhesion. These results are discussed in the following sections.

**6.2.2 Centrifugal ice adhesion test (CAT):** In this method, the samples are subjected to a freezing drizzle to accumulate ice under controlled conditions in an icing wind tunnel as explained in Chapter 3 (Experiment). The adhesion strength is determined from the

centrifugal force required to detach the ice from the sample surface fixed on an Al beam when subjected to an accelerating rotation in a centrifugal chamber (See Chapter 3 - Experiment). Bare Al was tested several times with the CAT apparatus before testing the samples to compare with literature values and the adhesion strength of $420\pm27$ kPa measured was found to be in good agreement with those found in the literature [17,121,122].

Similar to the results obtained in the pulling test, CAT measurements showed a poor adhesion of ice on superhydrophobic samples irrespective of the presence or absence of the dielectric coating of ZnO or $TiO_2$ and higher adhesion strengths on those surfaces not coated with rf-sputtered Teflon®. Figure 6.2 and Figure 6.3 show the photographs of the superhydrophobic (with rf-sputtered Teflon® coating) and hydrophilic (with no rf-sputtered Teflon® coating) nanorough sample surfaces before and after ice accumulation in the icing wind tunnel. It is clear from Figure 6.3 that ice hardly forms on superhydrophobic surfaces as the quantity of ice accumulated is much smaller on the superhydrophobic surfaces than on the hydrophilic surfaces for the same period of accumulation under same conditions.
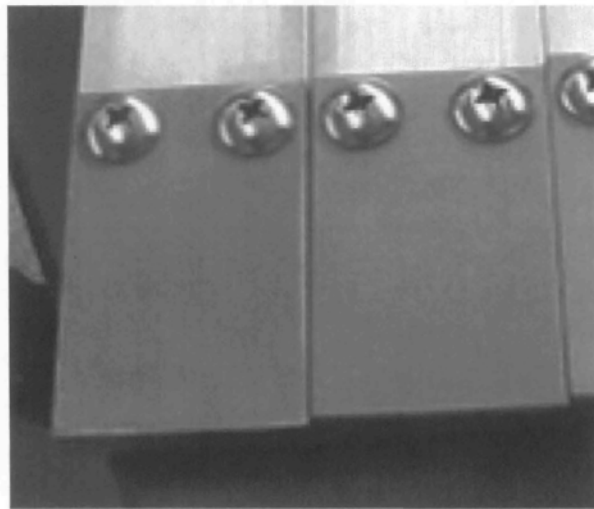
**Figure 6.2**. Samples before ice accumulation (ZnO in Figure).
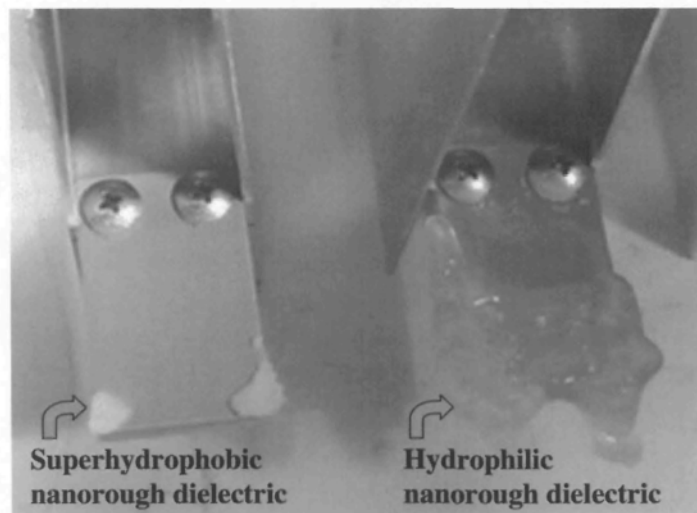


**Figure 6.3.** Superhydrophobic and hydrophilic dielectric (ZnO in Figure) surfaces after ice accumulation in the wind tunnel for the same time.

The samples shown in Figure 6.3 are superhydrophobic and hydrophilic nanorough ZnO surfaces. The ice (or the supercooled water) has almost zero adhesion to the superhydrophobic surfaces, however, since a tiny quantity of ice still sticks in the corners as seen in Figure 6.3, which may be due to surface defects, the ice starts growing in those places and builds up over the surface with the nucleation of ice started from those tiny areas. In these experiments, the superhydrophobic surfaces were exposed to freezing drizzle for a longer time to get the exposed area entirely covered. On the superhydrophobic surfaces, it took usually ~15 minutes to get the exposed area covered and another ~5 minutes to get enough weight of accumulation. In reality, the ice is in contact with the surface probably only in those corner areas, and the ice adhesion strength measured may not be representative of the genuinely superhydrophobic surface since it is not known if the ice was really in contact with that surface. The geometrical areas of contact used in the calculations correspond to the visual area of ice covered on the sample.

The ice adhesion strengths (Table 6.1) on ZnO ($\varepsilon = 8$) [112] and TiO$_2$ ($\varepsilon = 80$) [113,114] coated on flat alumina (~450 and ~460 kPa, respectively) or nanorough alumina (~482 and ~480 kPa, respectively) are similar and comparable to the value obtained on bare Al with the measurement errors taken in to consideration. According to the research hypothesis based on the concept of image charges [20], the dielectric constant should have an effect on ice adhesion. That is, the lower the dielectric constant, the lower the ice adhesion due to the elimination of image charge related electrostatic forces at the ice-dielectric interface, whereas, the values of adhesion strength obtained on the dielectric surfaces are similar and show no dependence on the dielectric constant. However, when

coated with rf-sputtered Teflon®, the flat ZnO surface (*low-ε*) shows a higher adhesion strength (~158 kPa) than the flat $TiO_2$ (high-ε) surface (~138 kPa) which is contrary to the prediction as the low-ε dielectric is supposed to reduce the adhesion strength [20]. On the other hand, rf-sputtered Teflon® coated nanorough ZnO (*low-ε*) shows a lower adhesion strength of ~66 kPa and rf-sputtered Teflon® coated nanorough $TiO_2$ (high-ε) shows a relatively higher adhesion strength of ~122 kPa.

It must be noted that these values are obtained using the geometrical area of coverage of ice visually measured using a ruler. Figure 6.4 and Figure 6.5 show a schematic of the way that ice can form on a hydrophilic and a superhydrophobic surface, to illustrate the following hypothesis. On a hydrophilic surface (without rf-sputtered Teflon® coating) as shown in Figure 6.4 the room temperature or supercooled water drops penetrate the pores and freeze, allowing the ice to grow further and cover the exposed area entirely. The true surface area of ice in contact is greater than the visual geometrical area that has been considered in the calculations to determine the adhesion strength. Conversely, on a superhydrophobic surface (Figure 6.5), the ice, if in contact, is actually in contact with the tips of the rough structure and has a contact fraction of only $f = 0.1$ with the rest of the ice at the interface in contact with air. Therefore, the true area of contact of ice with the substrate is expected to be smaller than the apparent area considered in the calculations. Therefore, the adhesion strength values obtained are not accurate. This inaccuracy also applies to the values obtained by the pulling test where the apparent (geometrical) area of contact of ice with the substrate surface is taken into consideration.
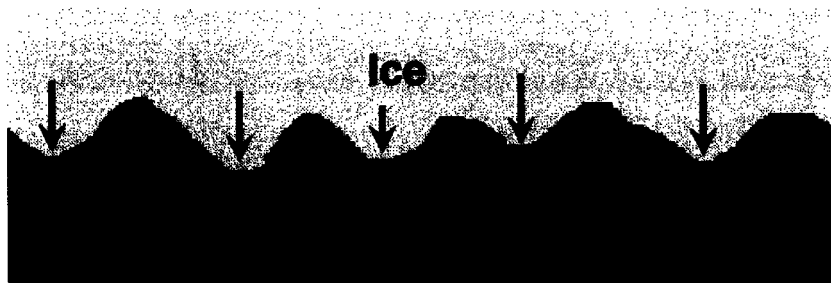
**Figure 6.4.** Ice formed on a hydrophilic rough surface
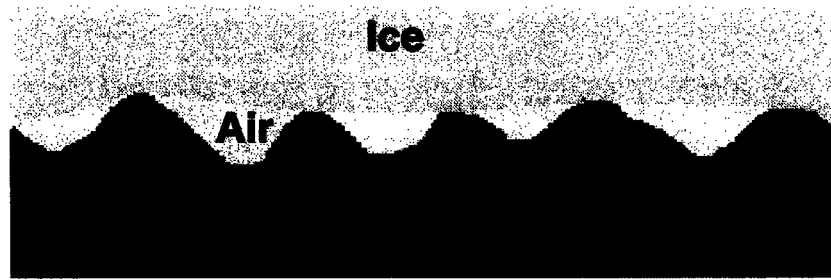


**Figure 6.5.** Ice formed on a superhydrophobic rough surface

In general, the higher ice adhesion encountered on the nanorough dielectric surfaces with no rf-sputtered Teflon® coating using either of the test methods could be attributed to the mechanical interlocking of ice in the pores of the rough structure on the surface as demonstrated by the contact angle investigation which showed either a complete absorption of the water drop (hydrophilicity) as observed on nanorough ZnO surfaces or a very low CA ($25\pm0.1°$) as obtained on nanorough $TiO_2$ surfaces. This observation is in good agreement with the work of Saito *et al.* [29], in which the authors state that a higher roughness can lead to a stronger adhesion of ice. Due to the mechanical interlocking of ice

in the rough structure, the locus of debonding in this case is not at the ice-dielectric interface, rather, the ice itself breaks leaving the interlocked ice as debris on the sample surfaces. The presence of tiny water droplets on the sample surface following exposure to room temperature after ice-shed is an excellent indication of the presence of mechanically interlocked ice.

On the other hand, on superhydrophobic nanorough dielectric surfaces that have been coated with rf-sputtered Teflon®, zero adhesion of ice was encountered using both test methods. The cause for zero adhesion could be attributed to their superhydrophobic behavior as demonstrated by the contact angle measurements which showed a very high water contact angle of $>160°$ and very low CAH of $<2°$ on those surfaces (Table 6.1). These surfaces are highly water repellent demonstrating superhydrophobicity with the water drops rolling off these surfaces due to very low hystereses.

Irrespective of the type of dielectric coating applied on the nanorough alumina substrates or even in absence of a dielectric coating, water drops rolled off these surfaces following rf-sputtered Teflon® coating, which is due to the small area of contact of the water drops on those surfaces and the weak bonding forces between the water drops and the low surface energy passivation layer. Such low hysteresis is due to the presence of rough nanopatterns on the surface allowing the entrapment of air in the pores (troughs) of the rough structure along with the low surface energy coating of rf-sputtered Teflon® reducing its interaction with water, which has a higher surface energy ($72 \ \mathrm{mJm^{-2}}$) as compared to Teflon® ($20 \ \mathrm{mJm^{-2}}$) [27,49]. Moreover, the small contact area fraction $f_1$ of only $\sim 0.1$ calculated from the Cassie-Baxter equation [49] on these superhydrophobic surfaces shows

that the contact area of the water drops is negligible. Due to the negligible area of contact of the water on these surfaces, when frozen the ice still retains the reduced contact area with the surface and therefore slides off those surfaces without much force needed during its separation from the mold (Figure 6.1) in the pulling method. Similarly, the supercooled water droplets also roll off those surfaces during exposure to freezing drizzle in the wind tunnel.

The presence of the low energy rf-sputtered Teflon® on the rough nanostructures, which leads to negligible interaction with water, prevents any mechanical interlocking of ice on those surfaces. Following exposure to room temperature after ice removal, the sample surfaces appeared dry on a macroscopic scale. The XPS investigation of the CAT tested superhydrophobic surfaces shows no significant differences in the elemental composition or in the different components of the rf-sputtered Teflon® providing evidence that the debonding of ice is at the ice- rf-sputtered Teflon® interface (Section 6.3.2.2). Also, the wetting characteristics of those surfaces determined following ice removal by both methods (Table 6.4, Section 6.3.2.2) showed that the surfaces retained their superhydrophobic properties and the CA and CAH results remained similar to those obtained on the same surfaces prior to CAT or pulling tests. The CA investigations, therefore, provide indirect evidence that the debonding of ice is at the ice- rf-sputtered Teflon® interface and not at the rf-sputtered Teflon®-dielectric interface, since the high CA and low CAH obtained following ice-shed is due to the continued presence of rf-sputtered Teflon®. Without the rf-sputtered Teflon® coating, the water would be absorbed by those surfaces making the surfaces hydrophilic (Table 6.1). The observation that the rf-

113

sputtered Teflon® coated nanorough surfaces retain their superhydrophobic properties following ice removal may also indicate that the ice never was in contact with the surface at all (Figure 6.6).
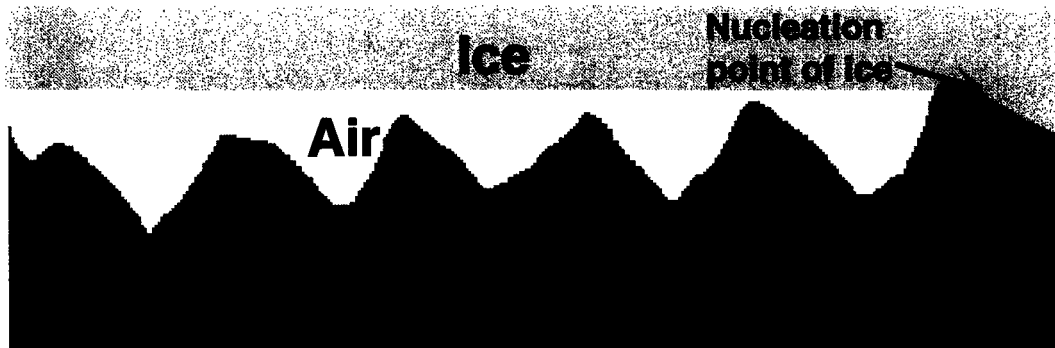


**Figure 6.6.** Ice grown on a nanorough superhydrophobic surface for a prolonged accumulation period with the nucleation sites at edge of the samples in contact with an untreated support.

A strong correlation between CA and ice adhesion strengths has been demonstrated by both pulling and CAT tests as shown in Figure 6.7. The adhesion strength of ice is found to decrease as the contact angle increases following a straight line equation of $\sigma(kPa) = 474 - 2.7\theta$ in the case of the pulling test and $\tau(kPa) = 514 - 2.7\theta$ in the case of CAT tests. Moreover, the adhesion strength of ice is negligible or zero at CAs greater than $160°$, where the surfaces are superhydrophobic. Although there is no report in the literature on ice adhesion on superhydrophobic surfaces, these observations support Petrenko and Peng's results on the shear strength of ice adhesion on various SAM-coated gold surfaces,

showing a linear reduction in the adhesion strength with increasing water CAs [39].

However, those authors did not obtain superhydrophobicity and their reported CA values

were lower than 100°.
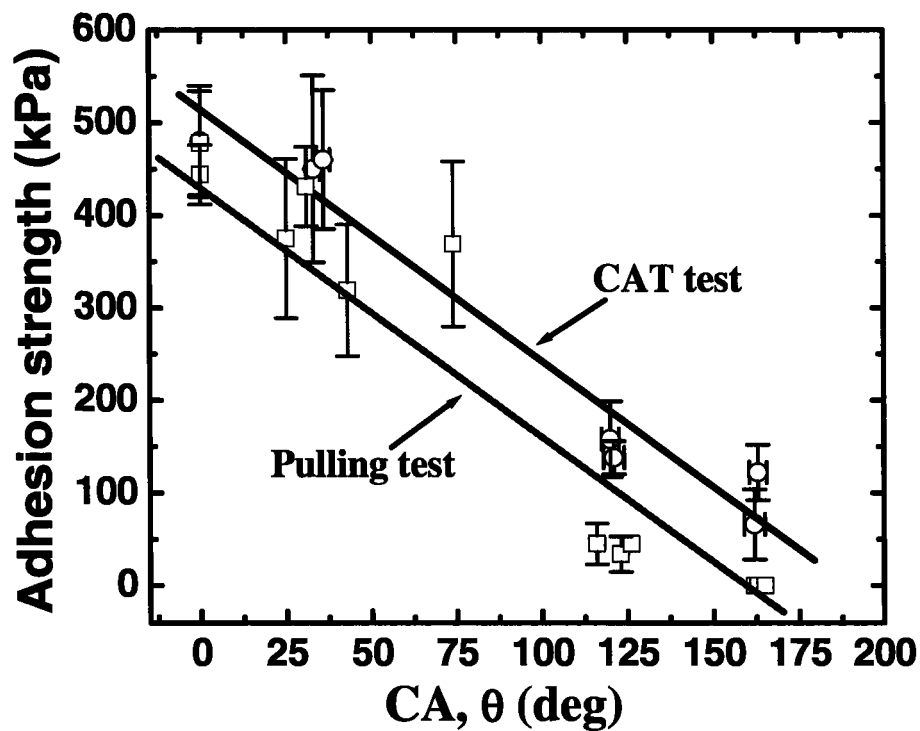


**Figure 6.7.** Correlation between CA and ice adhesion strengths by pulling and CAT tests.

The lower adhesion of ice on the rf-sputtered Teflon® coated surfaces, regardless of

the underlying substrate composition, could be attributed to the low depth of interaction of

water (and hence ice) of only 0.5 nm [174], compared with the thickness of the rf-sputtered Teflon® coating, estimated to be $\geq 4$ nm from the XPS investigation (See Chapter 5 - Nanopattern formation by substrate chemical etching). Both the dielectrics regardless of the dielectric constants showed reduced adhesion following passivation with rf-sputtered Teflon®, and demonstrated superhydrophobic properties. Superhydrophobicity, therefore, is found to confer icephobic properties; however, an effect of the dielectric constant of the dielectric layer on ice adhesion to the passivated surface was not observed in these tests. Ice adhesion and the water contact angle, therefore, are found to depend more upon the substrate roughness pattern and the passivation layer applied on the rough surface of the substrate, rather than the nature of the dielectric film which is effectively masked by the passivation layer. While the roughness of the substrate underlying the passivating layer of rf-sputtered Teflon® has an effect on the contact angle and ice adhesion, the dielectric constant of the substrate does not, because the water cannot "sense" it through the passivating layer due to its low interaction depth [174]. Therefore, to understand the effect of the dielectric constant on ice adhesion, the ice adhesion strengths obtained on the unpassivated dielectric systems were investigated.

From Table 6.1, it can be seen that flat ZnO and $TiO_2$ surfaces showed a high and comparable adhesion strength of 450±101 kPa and 460±75 kPa, respectively, both comparable to 420±27 kPa obtained on bare Al. Therefore, changing $\varepsilon$ from 80 ($TiO_2$) to 10 on alumina (bare Al) or to 8 (ZnO) showed no effect on ice adhesion, however, it can be seen that the adhesion strength is considerably lowered (~133 kPa) when bare Al surfaces were coated with rf-sputtered Teflon®, a dielectric itself with a dielectric constant as low as

$\varepsilon = 2$. Therefore, the dielectric constant may have an influence on ice adhesion; however, it requires a very low value (e.g. 2) to show its effect as reducing $\varepsilon$ to 8 from 80 does not show any effect on ice adhesion. These observations have been complemented by the theoretical prediction based on the image charge concept related to the dielectric constant of the material $\varepsilon$ by the equation $q' = q\dfrac{\varepsilon - 1}{\varepsilon + 1}$, where $q'$ is the image charge produced by a charge $q$ on the ice surface [20]. For ZnO ($\varepsilon = 8$), alumina ($\varepsilon = 10$) and TiO$_2$ ($\varepsilon = 80$), the $q'$ is found to be $0.78q$, $0.82q$ and $0.98q$, respectively. However, for a dielectric with $\varepsilon = 2$ (Teflon®), the image charge $q'$ is found to be only $0.33q$, which is one-third of the charge on ice as compared to the other two dielectrics studied for which the $q'$ is nearly the same as $q$.

Having a very low dielectric constant material reduces the electrostatic forces ($F = \dfrac{qq'}{r^2}$) at the ice-substrate interface due to smaller image charges. However, other forces such as van der Waals forces and hydrogen bonding are also important mechanisms involved in ice adhesion that have not been taken in to consideration in this research work. A study on the fundamental aspects of ice adhesion mechanisms is proposed as a future project.

The adhesion strengths of ice, measured on the flat surfaces with no rf-sputtered Teflon® coating, are not very different from those obtained on the dielectric-coated nanopatterned substrates with no rf-sputtered Teflon® coating and are very high. Therefore, to obtain lower adhesion, a nanotextured morphology with a low surface energy coating would be an asset and further investigations were carried out on the superhydrophobic

117

dielectric coatings by determining the adhesion reduction factor (ARF) (Table 6.1), which is defined as

*ARF = adhesion strength on reference / adhesion strength on candidate*

The highest ARF of 6.36 was obtained on ZnO-coated nanopatterned surfaces after coating with rf-sputtered Teflon® as compared to passivated $TiO_2$ coated nanopatterned surfaces, which showed an ice reduction of only 3.44, similar to that obtained on rf-sputtered Teflon® coated nanopatterned aluminum surfaces (ARF = 3.16).

There is no evidence that the ice adheres to the superhydrophobic surfaces (Figure 6.3), however, even if an ice film forms on superhydrophobic surfaces, it adheres less firmly as compared to the strong adhesion observed on a non-superhydrophobic surface (Table 6.1). Therefore, even if ice were to accumulate over a superhydrophobic surface, it may quickly fall off under its own weight. Also, the higher ARFs on those surfaces indicate that the adhesion of ice is lower on those surfaces, which can lead to easy removal of the any stuck ice from those surfaces.

## 6.3 Surface characterization of ice tested surfaces

The ice adhesion tests performed by the two test methods basically involve a procedure in which the ice grown or formed on the sample surface is detached by a certain force. Does this ice detachment alter the surface morphology and chemistry? SEM and XPS were used to investigate the surfaces following ice detachment and compared to results obtained prior to ice tests. Water contact angle measurements on those surfaces were also performed in

order to evaluate the stability of the superhydrophobicity of the passivated surfaces. These results will be discussed in the following sections.
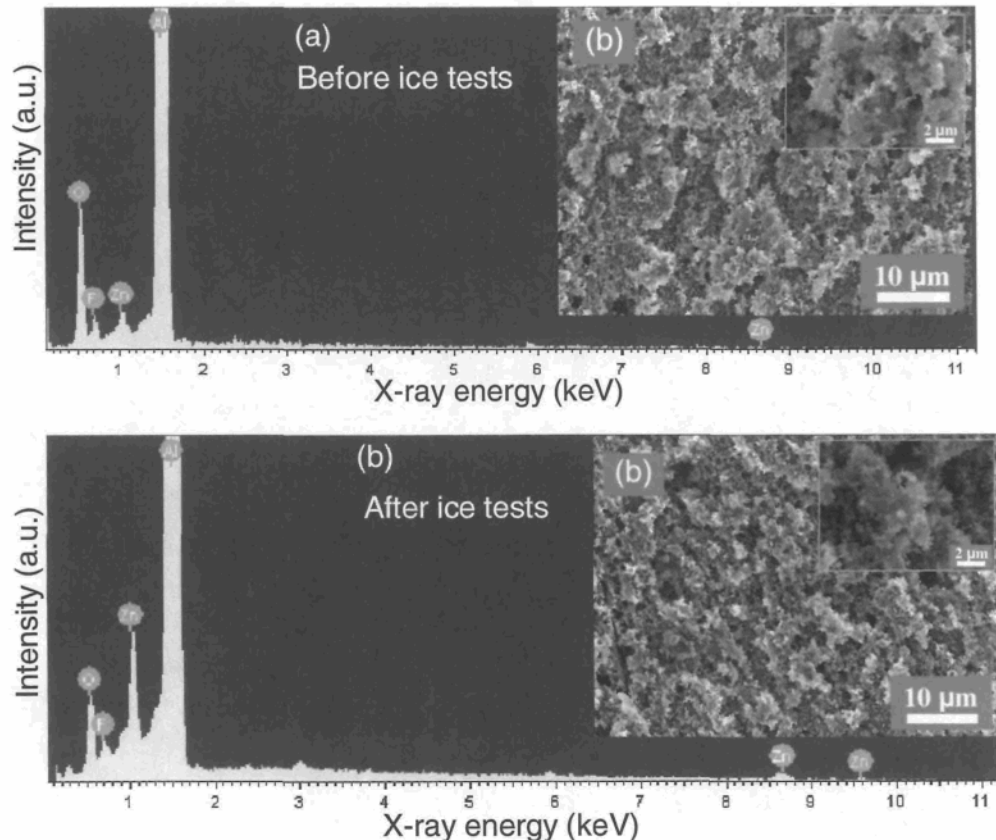


**Figure 6.8.** SEM/EDX images of rf-sputtered Teflon® coated ZnO on nanopatterned Al$_2$O$_3$ surfaces.

### 6.3.1 Morphological analysis of ice-tested nanorough dielectric surfaces

Figure 6.8 (a) and Figure 6.8 (b) shows the SEM images (in insets) and the corresponding EDX spectra of rf-sputtered Teflon® coated nanorough ZnO surfaces prior

119

to and following ice-tests, respectively. It is evident from the SEM images that no significant morphological changes are apparent following the detachment of ice from those surfaces. The EDX spectra of the samples prior to and after ice tests show all the elements of interest namely Zn, O, Al and F. The peak of F refers to the fluorine that originates from the rf-sputtered Teflon® coating on all those surfaces. The peak corresponding to Al arises from the aluminum substrate onto which ZnO was coated.
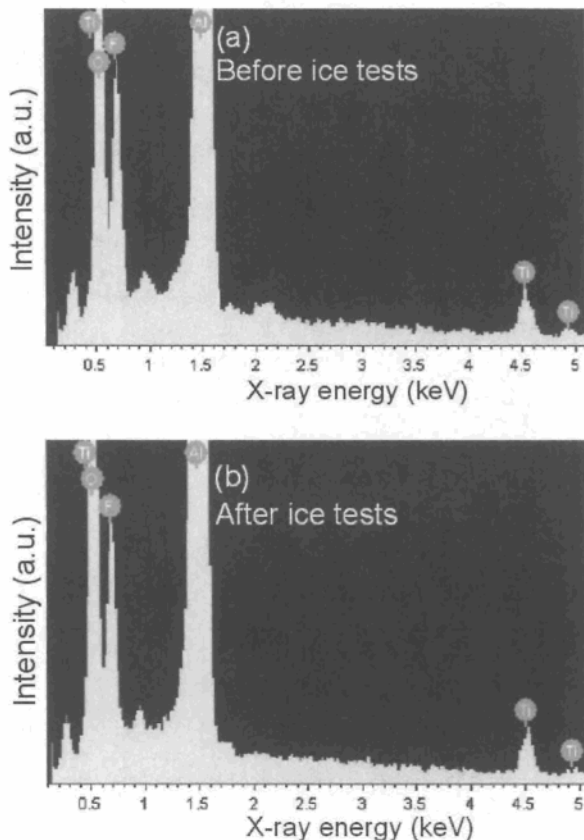


**Figure 6.9.** SEM/EDX spectra of rf-sputtered Teflon® coated nanorough $TiO_2$ surfaces **(a)** before ice tests and **(b)** after ice tests.

Similar results were observed on the TiO$_2$ system; therefore, only the EDX spectra are shown in Figure 6.9. It can be seen from Figure 6.9 that only the elements of Ti, O, Al and F are observed on the rf-sputtered Teflon® coated nanorough TiO$_2$ surfaces before and after ice tests indicating no changes in the elemental components.

## 6.3.2 Chemical analysis of ice-tested nanorough dielectric surfaces

XPS analyses were carried out to understand if any chemical changes occur due to the detachment of ice from those surfaces.

### 6.3.2.1. XPS analyses on the samples used in pulling tests:

The ice adhesion tests showed similar adhesion strengths on both FAS-17 passivated and rf-sputtered Teflon® coated nanorough dielectric surfaces. XPS analyses were performed on both FAS-17 passivated and rf-sputtered Teflon® coated surfaces to evaluate the chemical stability of the two surfaces.

The survey spectra of the FAS-17 passivated nanorough dielectric surfaces presented in Figure 6.10 (ZnO in the Figure) shows the presence of C, F, O and Zn (Ti in case of FAS-17 passivated nanorough TiO$_2$; Figure not shown). The two spectra are very similar showing no differences in the elemental peaks before or after ice tests. Evidently, the apparent concentration of the elements (Table 6.2) before and after ice detachment indicates no loss of FAS-17 from the nanorough dielectric surfaces following detachment of ice from those surfaces.
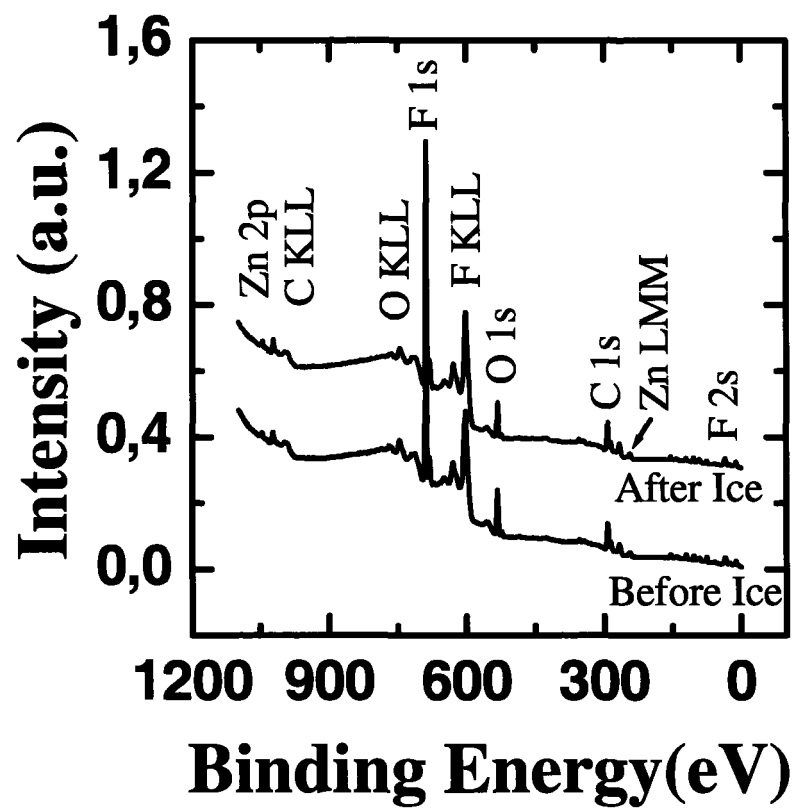
**Figure 6.10.** XPS survey spectra of FAS-17 passivated nanorough dielectric surface (ZnO in Figure) recorded prior to and following ice detachment.

**Table 6.2.** Apparent concentration of different elements before and after ice tests from XPS analysis of FAS-17 coated ZnO as well as TiO$_2$ on nanopatterned Al$_2$O$_3$.

| Elements | ZnO Concentrations (%) | | Elements | TiO$_2$ Concentrations (%) | |
|---|---|---|---|---|---|
| | Before ice tests | After ice tests | | Before ice tests | After ice tests |
| C | 27 | 27 | C | 23 | 25.4 |
| F | 53 | 56 | F | 52 | 56 |
| O | 15 | 11 | O | 18 | 13.4 |
| Si | 3 | 4 | Si | 2.4 | 3 |
| Zn | 2 | 2 | Ti | 4 | 2 |

Similarly, the survey spectra of rf-sputtered Teflon® coated dielectric surfaces (Figure 6.11) also showed no significant differences in the peaks of C and F prior to and following ice tests. The apparent concentrations of C, F and O (Table 6.3) show similar values following ice tests indicating no loss of the rf-sputtered Teflon® coating from the nanorough dielectric surfaces.
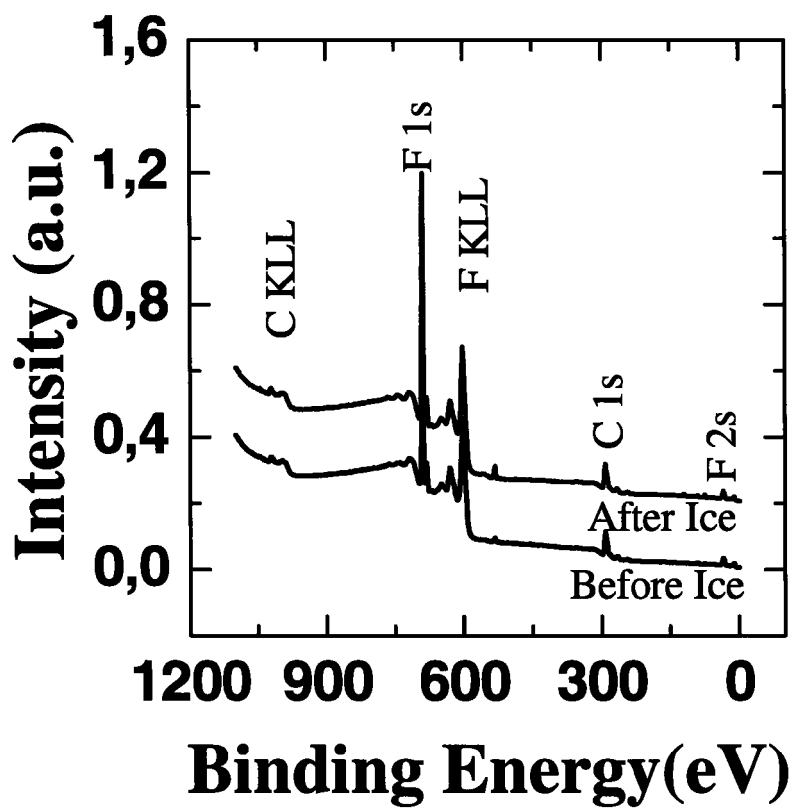
**Figure 6.11.** XPS survey spectra of rf-sputtered Teflon® coated nanorough dielectric surface (ZnO in figure) recorded prior to and following ice detachment.

**Table 6.3.** Apparent concentration of different elements before and after ice tests from XPS analysis of rf-sputtered Teflon® coated ZnO as well as $TiO_2$ on nanopatterned $Al_2O_3$.

| Elements | ZnO Conc. (%) | | Elements | $TiO_2$ Conc. (%) | |
|---|---|---|---|---|---|
| | Before ice tests | After ice tests | | Before ice tests | After ice tests |
| C | 35 | 33 | C | 34.5 | 34 |
| F | 63 | 62 | F | 63 | 62 |
| O | 1.6 | 4 | O | 2 | 3.5 |
| Zn | - | - | Ti | 0.4 | 0.7 |

### 6.3.2.2. XPS analyses on the samples used in CAT tests:

Since we wish to understand if the debonding is at the ice- rf-sputtered Teflon® interface or if the detachment of ice debonds the rf-sputtered Teflon® layer itself, XPS analyses were performed directly on the rf-sputtered Teflon® coated nanorough Al surfaces. Three different samples were analyzed, namely, one sample which was not subjected to ice accumulation and two other samples that were subjected to one or two ice accumulations and removals. Figure 6.12 shows the XPS survey spectra of the three samples which have been normalized with respect to the fluorine peak.

If the rf-sputtered Teflon® is removed during the ice-shed, it is expected that more of the substrate, which is Al, must be exposed following detachment and the Al-F ratio is expected to increase. However, it is found that the Al-F ratio is slightly lower in the ice tested samples as compared to the sample before ice tests (Table 6.4). For example, the Al-

F ratio of the fresh sample is found to be 0.055, whereas, it is found to be 0.042 on the sample where ice was detached once and 0.045 on the sample where ice was detached twice. This difference could be due to three separate samples having been analysed rather than the same sample surface having been analysed three times. The apparent concentration of the different elements, however, does not change within the error. Moreover, the contact angle data show no significant differences in their values before or after ice tests indicating indirectly that there is no loss of the rf-sputtered Teflon® layer following ice detachments. The water drops were found to roll off easily even after two ice detachments.

These analyses on the passivated nanorough surfaces, tested for ice adhesion using both methods, show that the passivation coating does not undergo any mechanical damage due to the separation of the ice from those surfaces.
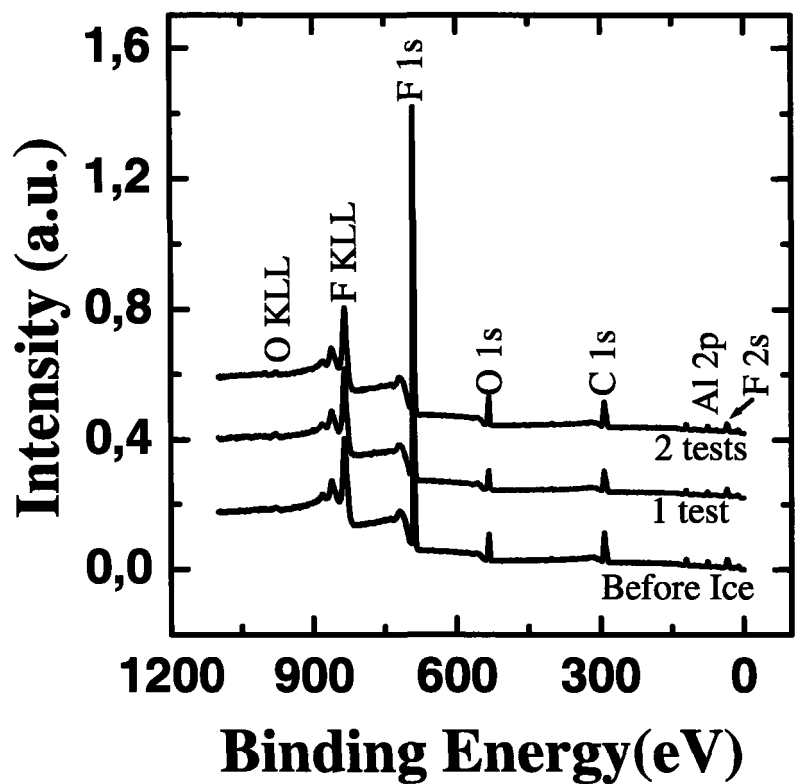
**Figure 6.12.** XPS survey spectra of rf-sputtered Teflon® coated nanorough Al surfaces before ice tests, following one ice detachment, and following two ice detachments.

**Table 6.4.** Concentration of different elements, Al-F ratio and CA data on rf-sputtered Teflon® coated nanorough Al surfaces before and after ice tests.

| | Concentration (%) | | | | | CA (°) | CAH (°) |
|---|---|---|---|---|---|---|---|
| | **Al** | **C** | **F** | **O** | **Al/F** | | |
| Before test | 3.6 ± 0.3 | 25.5 ± 0.5 | 65.8 ± 0.5 | 6 ± 0.2 | 0.055 | 161 ± 3 | 2 ± 1.2 |
| After one test | 2.8 ± 0.2 | 26.1 ± 0.4 | 65.7 ± 0.4 | 5.4 ± 0.1 | 0.042 | 162 ± 2 | 1.5 ± 0.8 |
| After two tests | 3 ± 0.2 | 24 ± 0.4 | 66.2 ± 0.4 | 6.83 ± 0.2 | 0.045 | 159 ± 2.5 | 2 ± 1.5 |

## 6.4 Hydrophobic properties of the ice-tested nanopatterned dielectrics

Previously, in Chapters 4 and 5, it was seen that the presence of a passivation layer on a surface aids in enhancing its water contact angle due to a lowering of the surface energy giving rise to hydrophobicity or in certain cases depending on the surface geometry, even superhydrophobicity. Does the superhydrophobicity persist following detachment of ice from those surfaces? SEM and XPS analyses confirm that there are no significant changes morphologically and chemically on those surfaces. Therefore, if the geometry and chemistry of a superhydrophobic surface remain unaltered, the superhydrophobic properties are also expected to be unchanged. Water contact angle measurements on the various ice-tested samples were performed and compared to the contact angle values obtained on the same surfaces prior to ice testing by both pulling and CAT methods.

Table 6.5 and Table 6.6 show the contact angle and the contact angle hysteresis values measured on hydrophobic and superhydrophobic dielectric surfaces on which the ice

adhesion was characterized by pulling and CAT tests, respectively. It is found that the detachment of ice from those surfaces does not have a significant influence on hydrophobicity as it is evident from the tables that the CA and CAH remain similar following ice tests. The water drops were still found to roll off those surfaces as was observed before the ice tests.

**Table 6.5.** CA and CAH before and after ice detachment by pulling test.

| Sample | CA ($^o$) | | CAH ($^o$) | |
|---|---|---|---|---|
| | Before ice-tests | After ice-tests | Before ice-tests | After ice-tests |
| Tef/ZnO/$Al_2O_3$ | 126 ± 2 | 123 ± 1 | *** | *** |
| Tef/ZnO/nr$Al_2O_3$ | 162 ± 2 | 163 ± 1.5 | 1 ± 0.5 | 1 ± 0.2 |
| Tef/$TiO_2$/$Al_2O_3$ | 123 ± 1.5 | 122 ± 2 | *** | *** |
| Tef/$TiO_2$/nr$Al_2O_3$ | 163 ± 2 | 162 ± 2 | 2 ± 1 | 8 ± 2 |

***These data were unobtainable; Tef refers to rf-sputtered Teflon®; nrAl and nr$Al_2O_3$ stand for Nanorough Al and Nanorough $Al_2O_3$, respectively.

**Table 6.6.** CA and CAH before and after ice detachment by CAT test.

| Sample | CA ($^o$) | | CAH ($^o$) | |
|---|---|---|---|---|
| | Before ice-tests | After ice-tests | Before ice-tests | After ice-tests |
| Tef/ZnO/$Al_2O_3$ | 120 ± 2.5 | 118 ± 2 | *** | *** |
| Tef/ZnO/nr$Al_2O_3$ | 162 ± 3 | 158 ± 2 | 2 ± 0.5 | 2.5 ± 1 |
| Tef/$TiO_2$/$Al_2O_3$ | 121 ± 3 | 123 ± 1.5 | *** | *** |
| Tef/$TiO_2$/nr$Al_2O_3$ | 163 ± 2.5 | 160 ± 3 | 2 ± 1.5 | 3 ± 2 |

***These data were unobtainable; Tef refers to rf-sputtered Teflon®; nrAl and nr$Al_2O_3$ stand for Nanorough Al and Nanorough $Al_2O_3$, respectively.

## 6.5 Summary and conclusions

Ice adhesion tests were performed using two independent test methods on the passivated and unpassivated nanorough dielectric surfaces obtained via substrate chemical etching. The ice adhesion strength on bare Al of ~450 kPa was used as a standard reference, being in good agreement with values obtained on bare Al in the literature. The adhesion strengths of ice on unpassivated dielectric surfaces of ZnO and $TiO_2$ were found to be similar to that obtained on bare Al surfaces. However, with a layer of rf-sputtered Teflon® on those surfaces, a significant reduction in the ice adhesion strength was encountered on flat as well as nanorough dielectric surfaces. In fact, on the nanorough dielectric surfaces or nanorough Al surfaces with an rf-sputtered Teflon® coating, the ice adhesion strength was close to zero. The cause for the non-stick nature of ice on the surfaces coated with rf-sputtered Teflon® is attributed to the low dielectric constant of 2 for Teflon®. If the dielectric constant of the surface is to have an effect on ice adhesion, it has to be as low as 2, as is the case for Teflon®, as changing the dielectric constant from 80 for $TiO_2$ through 8 for ZnO does not show a reduction in ice adhesion. In addition, the water drop in contact with the surface coated with rf-sputtered Teflon® does not "sense" the underlying dielectric coating as the depth of interaction of water with a surface is only 0.5 nm. Morphological and chemical analyses of the ice-tested nanorough dielectric and nanorough Al surfaces compared with results obtained prior to ice tests showed no significant differences suggesting that the ice never wet the rf-sputtered Teflon® coated nanorough surfaces in the first place. Water contact angle measurements performed on the ice tested samples demonstrated the same superhydrophobic properties encountered prior to ice tests. In the

main, a nanorough surface with a low surface energy passivation layer, irrespective of the type of material underlying the passivation layer, will lead not only to superhydrophobic properties, but also to icephobic properties as the room temperature water droplets as well as supercooled water drops roll off those surfaces.

# CHAPTER 7

## CONCLUSIONS AND FUTURE RECOMMENDATIONS

### 7.1 Conclusions

The hypotheses of this thesis work posit that

1. A superhydrophobic surface on which room temperature water drops roll off will be icephobic, since supercooled water droplets also will roll off those surfaces;

2. Even if the ice does form, a *low-ε* dielectric surface will reduce the adhesion strength of ice as on a low-ε surface, the image charge induced by the charge on the ice surface is lower, thereby reducing at least the electrostatic forces involved in the mechanisms of ice adhesion.

Superhydrophobicity is governed by two important properties: surface roughness and low surface energy. It was possible to achieve sufficient surface roughness by using the substrate chemical etching method, and upon coating with low surface energy rf-sputtered Teflon® or passivating with low surface energy fluoroalkyl-silane, superhydrophobic properties were observed, with water drops rolling off those surfaces at the slightest of inclination angles. Morphological analyses using scanning electron microscopy revealed the presence of a rough surface morphology following nanoroughening using substrate chemical etching. The X-ray photoelectron spectroscopy and Fourier transform infrared

spectroscopy analyses confirmed the presence and identity of the dielectric coatings applied on the flat and nanorough substrates as well as the contiguous nature of the low surface energy coating of rf-sputtered Teflon® or fluoroalkyl-silane.

Ice formed on hydrophilic nanorough surfaces of aluminium either uncoated or coated with dielectrics of ZnO or $TiO_2$ was found to strongly adhere with ice adhesion strengths greater than 420 kPa. The nanorough surfaces, when coated with rf-sputtered Teflon®, hardly allowed ice to form under freezing conditions since the supercooled water drops rolled off those surfaces due to the superhydrophobic properties demonstrated by those surfaces. Superhydrophobicity, which is due to the presence of nanoroughness as well as the low surface energy rf-sputtered Teflon® coating, leading to the non-wetting behaviour of water drops at room temperature as well as under freezing conditions, was found to be independent of what is underneath the rf-sputtered Teflon® layer. The principle accomplishment of this thesis is the demonstration that nanorough, passivated surfaces demonstrate not only superhydrophobicity, but also icephobicity.

However, ice was found to form and adhere on flat surfaces of aluminium coated with the different dielectrics of ZnO, $TiO_2$ and rf-sputtered Teflon®, with the realization that Teflon® is also a dielectric with $\varepsilon = 2$. Flat aluminium surfaces with dielectric coatings of $TiO_2$ ($\varepsilon = 80$) and ZnO ($\varepsilon = 8$) showed strong adhesion to ice with adhesion strengths greater than 400 kPa. No dependence of ice adhesion strength on the dielectric constant was observed in the case of these two dielectric materials. When the dielectric coating of rf-sputtered Teflon®, a dielectric itself (with $\varepsilon = 2$) was applied instead, a reduction in the adhesion strength of ice was obvious (~ 188 kPa). Therefore, a moderate reduction in $\varepsilon$

from 80 (TiO$_2$) to 8 (ZnO) was not enough to reduce the adhesion strength of ice as the mirror charge $q'$ changes only slightly from $(79/81)q$ to $(7/9)q$. Moreover, the role of lower mirror charges is related to only the elimination of the electrostatic interactions, while the other interactions such as hydrogen bonding and van der Waals forces still exist and have not been taken into account. However, reducing $\varepsilon$ to 2 (Teflon®) leading to $q' = (1/3)q$ did reduce the ice adhesion as measured on the flat surfaces. A similar behaviour was also observed on the nanorough surfaces which, upon rf-sputtered Teflon® (*low-ε*) coating, showed no adhesion to ice. Therefore, a *low-ε* dielectric surface coating may have an influence in considerably reduce ice adhesion to substrates and a *low-ε* dielectric surface coating on a nanorough surface has been found to have zero adhesion to ice.

The thickness of the rf-sputtered Teflon® layer has been found to be greater than a few nanometers, which is much higher than the depth of interaction of only 0.5 nm between water or ice and a substrate [173]. The water or ice, therefore, does not actually "sense" the substrate underneath the rf-sputtered Teflon® layer, leading to superhydrophobic and icephobic properties on any rf-sputtered Teflon® coated nanorough surface.

In conclusion, a combination of a surface nanoroughness together with a low dielectric constant surface coating has proven to have a great potential and as an icephobic material. The next question is: *"What about the stability of such coatings or surfaces?"*. The morphological characteristics and the chemical composition of those surfaces as studied using scanning electron microscopy and X-ray photoelectron spectroscopy prior to and following detachment of ice showed no significant differences in the respective surface

characteristics. These analyses show that these surfaces are morphologically and chemically stable even after exposure to low temperatures, high wind, freezing rain, etc.

Although we have demonstrated that the icephobic coatings developed in this work are stable with respect to the shedding of ice under laboratory conditions, before proceeding to real-world applications, the durability of the coatings with respect to rough handling and prolonged exposure to cold, and the corrosion and contamination of the surface, remains to be evaluated.

## 7.2 Future recommendations

The following is a brief summary of possible work that may be carried out with a view to acquiring a deeper understanding of the fundamental properties of solids, liquids and ice, which play an important role in the mechanism of ice adhesion.

1.  In this research, superhydrophobicity, a prerequisite in obtaining a reduced ice adhesion strength, has been demonstrated on surfaces obtained by chemical bath deposition and by chemical etching in combination with sol-gel spin-coating of dielectric layers and subsequent passivation with low surface energy materials. Superhydrophobicity has also been observed directly on chemically etched Al surfaces following low surface energy passivation. We conclude, therefore, that a certain nanoroughness on a surface with a low surface energy will lead to superhydrophobic properties. The path to superhydrophobic properties is not limited, however, to the two methods used here, as reviewed in **Chapter 2**. For a desired dielectric coating, another simple and a cost-effective method would be to incorporate a polymer solution into the sol of the desired

dielectric to form a homogenous mixture, which could then be spin-coated onto the substrate. The polymer chosen should be such that it has a melting point lower than that of the temperature at which the as-deposited film will be annealed so that during annealing the polymer will be burnt off leaving behind a final product of a nanorough surface of the dielectric. The surface may be rendered superhydrophobic following a low surface energy passivation.

2. It has been found in this research that the dielectric nature of the surface may play an important role in ice adhesion and that the superhydrophobic properties are achieved only when the dielectric constant is 2 (Teflon®) on nanorough surfaces irrespective of the nature of the material underlying the rf-sputtered Teflon® coating. Therefore, it would be interesting to nanotexture a porcelain surface and then coat it with rf-sputtered Teflon® for real-life applications. A proper etching method must therefore be chosen in creating a nanotexture on a porcelain surface. A common etchant used to chemically etch porcelain or ceramic surfaces is hydrofluoric acid (HF). Plasma etching may be another handy technique. A literature study will therefore be necessary in choosing a method which would be simple, economical and reproducible.

3. According to the literature, higher surface roughnesses can result in stronger ice adhesion to surfaces. However it has been seen in this research that, on a rough surface which is superhydrophobic, the ice adhesion is weaker and almost negligible. Therefore, the importance of surface roughness in ice adhesion must be well understood. Supercooled water drops may be drizzled on surfaces with higher and lower roughnesses, and a high speed camera may be used to record and visually analyze the

136

physical behavior of the supercooled water drops as they come into contact with the surfaces. This experiment will also provide information on the wetting (in other words "freezing") behavior of the supercooled water droplets on the surfaces that are superhydrophobic at room temperature.

4. Morphological and chemical characteristics have been found to remain similar on the superhydrophobic samples prior to and following ice detachment under laboratory conditions. However, in a real-world case, a surface is exposed to winter conditions and several accumulation events. Therefore, the same sample surface must be subjected to several accumulations, that is to say, several ice detachments via CAT or force tests must be performed sequentially in order to evaluate the stability of the coating through morphological and surface chemical tests.

5. With a scarcity of proper test methods for ice adhesion on thin film coatings, a suitable technique may be designed and developed. CIGELE's materials testing system (MTS) may be modified without interrupting its usual operation to test ice adhesion on thin film coatings. The system may consist of a fixed part in strong contact with ice and a movable part which will be coated with an icephobic material which will also be in contact with ice on the side with the icephobic coating. A tension generator connected to the movable part may apply a force to the movable part to separate the movable part from the fixed part and a tension gauge can be used to measure the force applied to separate the icephobic movable part from the ice on the fixed part. This can provide an approximate value of the shear adhesion strength of ice the icephobic coatings.

6. Fundamental aspects of ice adhesion to surfaces such as interactions other than the electrostatic forces considered in this dissertation including chemical bonding and van der Waals interactions need to be researched. Theoretical work may be helpful.

# References

[1] "Hundreds of Thousands Still Without Power", by A. O'Connor (2008-12-14), New York Times. http://thelede.blogs.nytimes.com/2008/12/15/hundreds-of-thousands-still-without-power/; Northwest Arkansas Ice Storm 2009, by Eisenvater, February 1, 2009, http://www.nowpublic.com/world/northwest-arkansas-ice-storm-2009.

[2] http://www.boston.com/bigpicture/2009/01/icy_days_and_nights.html Photo #28.

[3] http://www.sacbee.com/static/weblogs/photos/2008/12/017816.html.

[4] "The Ice Storm of 1998", by Canadian Broadcasting Corporation (CBC) http://archives.cbc.ca/IDD-1-70-258/disasters_tragedies/ice_storm/.

[5] http://www.verglas.netc.net/.

[6] http://www.dailykos.com/story/2005/9/12/185529/315.

[7] "The Implications of Surface Energy in Ice Adhesion",
K. Itagaki, Journal of Adhesion 16 (1983) 41.

[8] "Adhesion of Ice in its Relation to the De-Icing of Airplanes",
A. M. Rothrock, R. F. Selden, N. A. C. A. Technical Note No. 723, Washington 1939.

[9] "NTSB: Crew saw Ice Buildup before Crash", cbsnews.com, February 13, 2009, http://www.cbsnews.com/stories/2009/02/13/national/main4801448.shtml.

[10] "Reduction of ice adhesion to stainless steel by ice electrolysis",
V.F. Petrenko, S. Qi, J. Appl. Phys. 86 (1999) 5450.

[11] "Effects of High Altitude and Atmospheric Icing on the Performance of Outdoor Insulators",
M. Farzaneh, J. Zhang, M. Frechette, T. Sakakibara, E. Da Silva, IEEE PES Transmission and Distribution Conference, Caracas, August 2006, ID-014.

[12] "Survey of electrical and mechanical failures of insulators caused by ice and/or snow",
S. Yoshida, K. Naito, Electra 222 (2005) 22.

[13] "Flashover Performance of Insulators in the Presence of Short Icicles",
M. Farzaneh, O. T. Melo, Int. J. Offshore Polar Eng. 4 (1994) 112.

[14] http://www.aircanada.com/en/about/media/facts/photos_winter.html

[15] "Minimizing Effects from Highway Deicing", EPA 832-F-99-016 (1999).

[16] "Airplane Deicing Fluid Recovery Systems", EPA 832-F-99-043 (1999).

[17] "A new method for measuring ice adhesion strength at an ice-substrate interface",
M. Javan-Mashmool, C. Volat, M. Farzaneh, Hydrol. Process. **20** (2006) 645.

[18] "De-Icing/Anti-Icing Techniques for Power Lines. Current Methods and Future Direction",
C. Volat, M. Farzaneh, A. Leblond, Proceedings of the 10th International Workshop on Atmospheric Icing of Structures (IWAIS XI), Montréal, June 2005, p 323.

[19] "Modeling and Simulation of the Ice Melting Process on a Current-Carrying Conductor",
Z. Peter, PhD thesis in Engineering, UQAC, April 2006.

[20] "Physical Mechanisms Responsible for Ice Adhesion",
I. A. Ryzhkin, V. F. Petrenko, J. Phys. Chem. B **101** (1997) 6267.

[21] "Physics of Ice",
V. F. Petrenko, R. W. Whitworth, Oxford university press, Oxford, 1999.

[22] "Adhesion of ice to coatings and the performance of ice release coatings",
V. K. Croutch, R. A. Hartley, J. Coat. Tech. **64** (1992) 41.

[23] "A hydrophobic self-assembled monolayer with improved adhesion to aluminum for deicing application",
B. Somlo, V. Gupta, Mech. Mater. **33** (2001) 471.

[24] "Tests of the Performance of Coatings for Low Ice Adhesion",
D. N. Anderson, A. D. Reich, NASA Technical Memorandum, 107399 AIAAA-97-0303 (1997).

[25] "Alkylsilane self-assembled monolayers: Modeling their wetting characteristics",
S. A. Kulinich , M. Farzaneh, Appl. Surf. Sci. **230** (2004) 232.

[26] "Non-sticking drops",
D. Quéré, Rep. Prog. Phys. **68** (2005) 2495.

[27] "Purity of the sacred lotus, or escape from contamination in biological surfaces",
W. Barthlott, C. Neinhuis, Planta **202** (1997) 1.

[28] "How a Solid Coating can Reduce the Adhesion of Ice on a Structure",
C. Laforte, J. -L. Laforte, J.-C. Carrier, Proceedings of the International Workshop on
Atmospheric Icing of Structures (IWAIS) (2002) p. 6.

[29] "Water and Ice-repellent Coatings",
H. Saito, K. Takai, G. Yamauchi, Surf. Coat. Int. **80** (no. 4) (1997) 168.

[30] http://en.wikipedia.org/wiki/File:SnowflakesWilsonBentley.jpg.

[31] "Wind energy: cold weather issues",
A. Lacroix, J. F. Manwell, 2000. p. 1–17.

[32] "The physics of clouds",
J. Mason, Oxford University Press, Oxford, 1971.

[33] "An improved approach for the determination of in-cloud icing at wind turbine sites",
R. Cattin, S. Kunz, A. Heimo, R. Oechslin, M. Russi, Federal Office of Meteorology and
Climatology MeteoSwiss COST Action 727.

[34] "Icing Rate Meter Estimation of Atmospheric Cable Icing",
P. McComber, J. Druez, J. Laflamme, International Journal of Offshore and Polar
Engineering Vol. 5, No. I, March 1995 (ISSN 1053-5381).

[35] "A review of surface engineering issues critical to wind turbine performance",
N. Dalili, A. Edrisy, R. Carriveau, Renewable and Sustainable Energy Reviews **13** (2009)
428.

[36] http://weathersavvy.com/A-Winter.html

[37] "Overhead Power Lines: Planning, Design, Construction",
F. Kiessling, P. Nefzger, J. F. Nolasco, U. Kaintzyk, Springer 2003 (ISBN: 978-3-540-
00297-0).

[38] "Assessment of Superstructure Ice Protection as Applied to Offshore Oil Operations
Safety",
C. C. Ryerson, ERDC/CRREL TR-08-14, September 2008.

[39] "Reduction of ice adhesion to metal by using self-assembling monolayers (SAMs)",
V. Petrenko, S. Peng, Can. J. Phys. **81** (2003) 387.

[40] "Test of performance of coating for low ice adhesion",
D. N. Anderson, A. D. Reich, 35th aerospace sciences meeting & exhibit sponsored by the
American Institute of Aeronautics and Astronautics, Reno, Nevada; January 6–10, 1997.

[41] "Progress in evaluating surface coatings for icing control at Corps Hydraulic Structures",
U.S. Army Engineer Research and Development Center, Hanover, New Hampshire. ERDC/CRREL Technical Note 03-4; 2003. p. 1–8.

[42] "Double lap shear testing of coating-modified ice adhesion to space shuttle component surfaces",
M. G. Ferrick, N. D. Mulherin, B. A. Coutermarsh, G. D. Durell, L. A. Curtis, T. L. St. Clair, E. S. Weiser, R. J. Cano, T. M. Smith, C. G. Stevenson, E. C. Martinez, Hanover, New Hampshire: U.S. Army Engineer Research and Development Center; 2006, ERDC/CRREL TR-06-21. p. 1–53.

[43] "Superhydrophobic Coatings with Reduced Ice Adhesion",
D.K. Sarkar, M. Farzaneh, Journal of Adhesion Science and Technology (*in press*).

[44] "Elaboration of $Al_2O_3$/PFFE Coatings for Protecting Aluminium Surfaces",
R. Menini, M. Farzaneh, Surf. Coat. Technol. (2009), doi:10.1016/j.surfcoat.2009.01.030.

[45] http://cigele.ca/index_en.htm.

[46] "Works",
T. Young, Phil. Trans., 84 (1805), edited by Peacock, 1, 432.

[47] "Self-cleaning Surfaces - Virtual Realities",
R. Blossey, Nat. Mater. **2** (2003) 301.

[48] "Resistance of Solid Surfaces to Wetting by Water",
R. N. Wenzel, Ind. Eng. Chem. **28** (1936) 988.

[49] "Wettability of porous surfaces",
A. B. D.Cassie, S. Baxter, Trans. Faraday Soc. **40** (1944) 546.

[50] "Contact Angle, Wettability, and Adhesion",
R. E. Jr. Johnson, R. H. Dettre, Edited by R. F. Gould, Adv Chem Ser **43** (1964) 112.

[51] "The Wonder of Magic: Eliciting Wonder and Analyzing its Expression",
S. T. Raphail, Master of Science in Media Arts and Sciences, Massachusetts Institute of Technology (September 2007).

[52] "Smart, clean surfaces"
P. Gould, Materials Today **6** (2003) 44.

[53] http://www.pbase.com/rubinphoto/image/32993464&exif=N

[54] "Super-Hydrophobic Surfaces: From Natural to Artificial",
L. Feng, S. Li, Y. Li, H. Li, L. Zhang, J. Zhai, Y. Song, B. Liu, L. Jiang, D. Zhu, Adv. Mater. **14** (2002) 1857.

[55] "Biophysics Water-repellent legs of water striders",
X. Gao, L. Jiang, Nature **432** (2004) 36.

[56] "Directional adhesion of superhydrophobic butterfly wings", Y. Zheng, X. Gao, L. Jiang,
Soft Matter **3** (2007) 178.

[57] http://www.dharmaflix.com/

[58] "Microtophography and antifouling properties of the shell surface of the bivalve molluscs Mytilus galloprovincialis and Pinctada imbricata",
A. Scardino, R. De Nys, O. Ison, W. O'Connor, P. Steinberg, Biofouling, **19** (2003) 221.

[59] "A simple route towards the reduction of surface conductivity in gas sensor devices",
J. D. J. S. Samuel, P. Ruther, H.-P. Frerichs, M. Lehmann, O. Paul, J. Ruhe, Sens. Actuators, **B 110** (2005) 218.

[60] "Electrospinning Nanofiber Membranes of Poly[bis(trifluoroethoxy)phosphazene]",
A. Singh, L. Steely, H. R. Allcock, Polym. Prepr. (ACS, Div. Polym. Chem.), **46** (2005) 599.

[61] "Liquid Morphologies on Structured Surfaces: From Microchannels to Microchips",
H. Gau, S. Herminghaus, P. Lenz, R. Lipowsky, Science **283** (1999) 46.

[62] "Super-hydrophobic surfaces improve corrosion resistance of copper in seawater",
T. Liu, Y. Yin, S. Chen, X. Chang, S. Cheng, Electrochim. Acta, **52** (2007) 3709.

[63] "Preparation of Super-Water-Repellent Fluorinated Inorganic-Organic Coating Films on Nylon 66 by the Sol-Gel Method Using Microphase Separation",
K. Satoh, H. Nakazumi, J. Sol–Gel Sci. Technol., **27** (2003) 327.

[64] "Adhesion and Sliding of Wet Snow on a Super-hydrophobic Surface with Hydrophilic Channels",
T. Kako, A. Nakajima, H. Irie, Z. Kato, K. Uematsu, T. Watanabe, K. Hashimoto, J. Mater. Sci., **39** (2004) 547.

[65] "Recent Studies on Super-Hydrophobic Films",
A. Nakajima, K. Hashimoto, T. Watanabe, Monatshefte für Chemie **132** (2001) 31.

[66] "Superhydrophobic surfaces",
M. Ma, M. R., Hill, Current Opinion in Colloid & Interface Science **11** (2006) 193.

[67] "Superhydrophobic surfaces: from structural control to functional application",
X. Zhang, F. Shi, J. Niu, Y. Jiang, Z. Wang, J. Mater. Chem. **18** (2008) 621.

[68] "What do we need for a superhydrophobic surface? A review on the recent progress in the preparation of superhydrophobic surfaces",
X.-M. Li, D. Reinhoudt, M. Crego-Calama, Chem. Soc. Rev. **36** (2007) 1350.

[69] "Recent developments in superhydrophobic surfaces and their relevance to marine fouling: a review",
J. Genzer, K. Efimenko, Biofouling, **22** (2006) 339.

[70] "Super-Water-Repellent Fractal Surfaces",
T. Onda, S. Shibuichi, N. Satoh, K. Tsujii, Langmuir **12** (1996) 2125.

[71] "Electrospinning of Poly[bis(2,2,2-trifluoroethoxy)phosphazene] Superhydrophobic Nanofibers",
A. Singh, L. Steely, H. R. Allcock, Langmuir **21** (2005) 11604.

[72] "Production of superhydrophobic polymer fibers with embedded particles using the electrospinning technique",
R. Menini, M. Farzaneh, Polymer Intl. **57** (2008) 77.

[73] "Fabrication of tunable superhydrophobic surfaces",
J. Y. Shiu, C. W. Kuo, P. Chen, Proceedings of SPIE-The International Society for Optical Engineering, **5648** (2005) 325.

[74] "Two-Level Structured Self-Adaptive Surfaces with Reversibly Tunable Properties",
S. Minko, M. Muller, M. Motornov, M. Nitschke, K. Grundke, M. Stamm, J. Am. Chem. Soc. **125** (2003) 3896.

[75] "Reversible Superhydrophobicity to Superhydrophilicity Transition by Extending and Unloading an Elastic Polyamide Film",
J. L. Zhang, J. A. Li, Y. C. Han, Macromol Rapid Commun **25** (2004) 1105.

[76] "Progess in superhydrophobic surface development",
P. Roach, N. J. Shirtcliffe, M. I. Newton, Soft Matter **4** (2008) 224.

[77] "Superhydrophobicity and Superhydrophilicity of Regular Nanopatterns",
E. Martines, K. Seunarine, H. Morgan, N. Gadegaard, C. D. W. Wilkinson, M. O. Riehle, Nano Lett. **5** (2005) 2097.

[78] "Directed Fabrication of Radially Stacked Multifunctional Oxide Heterostructures Using Soft Electron-Beam Lithography",
Z. Pan, S. K. Donthu, N. Wu, S. Li, V. P. Dravid, Small **2** (2006) 274.

[79] "Fabrication of PECVD-grown fluorinated hydrocarbon nanoparticles and circular nanoring arrays using nanosphere lithography",
D.K. Sarkar, M. Farzaneh, Appl. Surf. Sci. **254** (2008) 3758.

[80] "Digital microfluidics using soft lithography",
J. P. Urbanski, W. Thies, C. Rhodes, S. Amarasinghe, T. Thorsen, Lab Chip **6** (2006) 96.

[81] "Superhydrophobic properties of ultrathin rf-sputtered Teflon films coated etched aluminum surfaces",
D.K. Sarkar, M. Farzaneh, R.W. Paynter, Mater. Lett. **62** (2008) 1226.

[82] "Fabrication of Tunable Superhydrophobic Surfaces by Nanosphere Lithography",
J. Y. Shiu, C. W. Kuo, P. L. Chen, C. Y. Mou, Chem. Mater. **16** (2004) 561.

[83] "Optically transparent superhydrophobic silica-based films",
H. M. Shang, Y. Wang, S. J. Limmer, T. P. Chou, K. Takahashi, G. Z. Cao, Thin Solid Films **472** (2005) 37.

[84] "Super-Liquid-Repellent Surfaces Prepared by Colloidal Silica Nanoparticles Covered with Fluoroalkyl Groups",
M. Hikita, K. Tanaka, T. Nakamura, T. Kajiyama, A. Takahara, Langmuir **21** (2005) 7299.

[85] "Polyelectrolyte Multilayer as Matrix for Electrochemical Deposition of Gold Clusters: Toward Super-Hydrophobic Surface",
X. Zhang, F. Shi, X. Yu, H. Liu, Z. Wang, L. Jiang, X. Li, J. Am. Chem. Soc. **126** (2004) 3064.

[86] "Superhydrophobic properties of silver-coated films on copper surface by galvanic exchange reaction",
A. Safaee, D.K. Sarkar, M. Farzaneh, Appl. Surf. Sci. **254** (2008) 2493.

[87] "UV-Manipulated wettability between superhydrophobicity and superhydrophilicity on a transparent and conductive $SnO_2$ nanorod film",
W. Q. Zhu, X. J. Feng, L. Feng, L. Jiang, Chem. Commun. DOI: 10.1039/b603634a (2006) 2753.

[88] "Thermal effect on superhydrophobic performance of stearic acid modified ZnO nanotowers",
N. Saleema, M. Farzaneh, Appl. Surf. Sci. **254** (2008) 2690.

145

[89] "Super-hydrophobic/super-hydrophilic patterning surfaces by photocatalytic lithography",
H. Notsu, W. Kubo, I. Shitanda, T. Tatsuma, J. Mater. Chem. **15** (2005) 1523.

[90] "Microfabricated textured surfaces for super-hydrophobicity investigations",
M. Callies, Y. Chen, F. Marty, A. Pépin, D. Quéré, Microelectronic Engineering **78–79** (2005) 100.

[91] "Sol-Gel Science: The Physics and Chemistry of Sol-Gel Processing",
C. J. Brinker and G. W. Scherer, Academic Press, New York, 1990.

[92] "Intrinsically Superhydrophobic Organosilica Sol–Gel Foams",
N. J. Shirtcliffe, G. McHale, M. I. Newton, C. C. Perry, Langmuir **19** (2003) 5626.

[93] "Sol-gel Technology for Sensor Applications",
N. K. Chaudhury, R. Gupta, S. Gulia, Defence Science Journal **57** (2007) 241.

[94] "Superhydrophobic nanostructures based on porous alumina",
D. Kim, W. Hwang, H. C. Park, K. –H. Lee, Current Applied Physics **8** (2008) 770.

[95] "Stable Superhydrophobic Surface via Carbon Nanotubes Coated with a ZnO Thin Film",
L. Huang, S. P. Lau, H. Y. Yang, E. S. P. Leong, S. F. Yu, S. Prawer, J Phys Chem B **109** (2005) 7746.

[96] "A Lotus-Leaf-like Superhydrophobic Surface: A Porous Microsphere/Nanofiber Composite Film Prepared by Electrohydrodynamics",
L. Jiang, Y. Zhao, J. Zhai, Angew. Chem. Int. Ed. **43** (2004) 4338.

[97] "Preparation of Transparent Superhydrophobic Boehmite and Silica Films by Sublimation of Aluminum Acetylacetonate",
A. Nakajima, A. Fujishima, K. Hashimoto, T. Watanabe, Adv. Mater. **11** (1999) 1365.

[98] "Super-Hydrophobic Surface of Aligned Polyacrylonitrile Nanofibers",
L. Feng, S. Li, H. Li, J. Zhai, Y. Song, L. Jiang, D. Zhu, Angew. Chem., Int. Ed. **41** (2002) 1221.

[99] "Hydrophobic and Ultrahydrophobic Multilayer Thin Films from Perfluorinated Polyelectrolytes",
R. M. Jisr, H. H. Rmaile, J. B. Schlenoff, Angew. Chem., Int. Ed. **44** (2005) 782.

[100] "Controlling the adhesion between diamond-like carbon (DLC) film and high-density polyethylene (HDPE) substrate",
T. Hoshida, D. Tsubone, K. Takada, H. Kodama, T. Hasebe, A. Kamijo, T. Suzuki, A. Hotta, Surface and Coatings Technology **202** (2007) 1089.

[101] "The properties of fluorine containing diamond-like carbon films prepared by plasma-enhanced chemical vapour deposition",
A. Bendavid, P.J. Martin, L. Randeniya, M.S. Amin, Diamond and Related Materials **18** (2009) 66.

[102] "Physics and Chemistry at Oxide Surfaces",
C. Noguera, Cambridge University Press, Cambridge, 1996.

[103] "Review on methods to deposit catalysts on structured surfaces",
V. Meille, Applied Catalysis A: General, **315** (2006) 1.

[104] "High dielectric constant gate oxides for metal oxide Si transistors",
J. Robertson, Rep. Prog. Phys. **69** (2006) 327.

[105] "Nanomaterials: Synthesis, Properties and Applications",
Edited by A.S. Edelstein, R. C. Cammarata, Institute of Physics Publishing, London, 1998.

[106] "Titanium silicate films with high dielectric constant",
M. A. El-Khakani, D. K. Sarkar, L. Ouellet, D. Brassard, US Patent 7,101,754 (2006).

[107] "Dielectric properties of sol–gel derived high-k titanium silicate thin films",
D. K. Sarkar, D. Brassard , M. A. El-Khakani, L. Ouellet, Thin Solid Films **515** (2007) 4788.

[108] "Size Dependence of Stöber Silica Nanoparticle Microchemistry",
C. A. R. Costa, C. A. P. Leite, F Galembeck, J. Phys. Chem. B., **107** (2003) 4747.

[109] "Organically modified sol-gel sensors",
O. Lev, L. Tsionsky, L. Rabinovich, V. Glezer, S. Sampath, I. Pankratov, J. Gun, Analytical Chemistry **67** (1995) 22A.

[110] "Electrical properties of $Al_2O_3$ films for TFEL-devices made with sol–gel technology",
K. Vanbesien, P. De Visschere, P. F. Smet, D. Poelman, Thin solid films **514** (2006) 323.

[111] "Sol–gel production of zirconia nanoparticles with a new organic precursor",
C. Suciu, L. Gagea, A.C. Hoffmann, M. Mocean, Chemical Engineering Science **61** (2006) 7831.

147

[112] "Dielectric properties of sol-gel derived ZnO thin films",
T.P. Alexander, T.J. Bukowski, G. Teowee, D.R. Uhlmann, K.C. McCarthy, J. Dawley,
B.J.J. Zelinski, Proceedings of the IEEE International Symposium on Applications of
Ferroelectrics 2 (1996) 585.

[113] "Dielectric properties of sol–gel derived high-k titanium silicate thin films",
D. K. Sarkar, D. Brassard, M. A. El-Khakani, L. Ouellet, Thin Solid Films 515 (2007) 4788.

[114] "Titanium silicate films with high dielectric constant",
M. A. El-Khakani, D. K. Sarkar, L. Ouellet, D. Brassard, US Patent 7,101,754 (2006)

[115] "Band offsets of wide-band-gap oxides and implications for future electronic
devices",
Robertson J, J. Vac. Sci. Technol. B 18 (2000) 1785.

[116] "Superhydrophobic ZnO nanotowers"
N. Saleema, D. K. Sarkar, M. Farzaneh, E. Sacher, Proceedings of Nanotech 2006, Boston,
7-11 May 2006, p. 158.

[117] "User Manual for drop shape analyzer" Krüss GmbH, DSA1 v1.9-03.

[118] "Analysis and Testing of Adhesive Bonds",
G. P. Anderson, S. J. Bennet, K. L. DeVries, Academic Press, New York, 1997.

[119] "Evaluation of Coatings for Icing Control at Hydraulic Structures",
Ice Engineering, CRREL, US Army Corps of Engineers, No. 33, January 2002.

[120] "Measurement and control of Ice Adhesion to Aluminum 6061 Alloy",
P. Archer, V. Gupta, J. Mech. Phys. Solids 46 (1998) 1745.

[121] "Icephobic Material Centrifuge Adhesion Test",
C. Laforte, A. Beisswenger, Proceedings of the International Workshop on Atmospheric
Icing of Structures (IWAIS XI), Montréal, 16 June 2005, p. 357.

[122] "Adhesive properties of ice"
H. H.G. Jellinek, J. Colloid. Sci. 14 (1959) 268.

[123] "A 5% efficient photoelectrochemical solar cell based on nanostructured ZnO
electrodes",
K. Keis, E. Magnusson, H. Lindstorm, S.E. Lindquist, A. Hagfeldt, Sol. Energy, 73 (2002)
51.

[124] "ZnO Schottky ultraviolet photodetectors",
S. Liang, H. Sheng, Y. Liu, Z. Hio, Y. Lu, H. Shen, J. Cryst. Growth, 225 (2001) 110.

[125] "Low-Temperature Fabrication of Light-Emitting Zinc Oxide Micropatterns using Self-Assembled Monolayers",
N. Saito, H. Haneda, T. Sekiguchi, N. Ohashi, I. Sakaguchi, K. Koumoto, Adv. Mater. **14** (2002) 418.

[126] "Microstructural Evolution and Preferred Orientation Change of Radio-Frequency-Magnetron Sputtered ZnO Thin Films",
Y.E. Yee, J.B. Lee, Y.J. Kim, H.K. Yang, J.C. Park, H.J. Kim, J. Vac. Sci. Tech. A **14** (1996) 1943.

[127] "Characteristics of high quality ZnO thin films deposited by pulsed laser deposition",
V. Craciun, J. Elders, J.G.E. Gardenievs, I.W. Boyd, Appl. Phys. Lett. **65** (1994) 2963.

[128] "Low-temperature electrical conductivity and optical absorption edge of ZnO films prepared by chemical vapour deposition",
Y. Natsume, H. Sakata, T. Hirayama, Phys. Status Solidi A **148** (1995) 485.

[129] "Effects of thermal annealing of ZnO layers grown by MBE",
K. Ogata, K. Sakurai, Sz. Fujita, Sg. Fujita, K. Matsushige, J. Cryst. Growth **214** (2000) 312.

[130] "Zinc oxide films prepared by sol-gel spin-coating", Y. Natsume, H. Sakata, Thin Solid Films **372** (2000) 30.

[131] "Water Ultrarepellency Induced by Nanocolumnar ZnO Surface",
X. -T. Zhang, O. Stao, A. Fujishima, Langmuir **20** (2004) 6065.

[132] "Thin-film transistors with active layers of zinc oxide (ZnO) fabricated by low-temperature chemical bath method",
H. -C. Cheng, C. -F. Chen, C. -C. Lee, Thin Solid Films **498**, (2006) 142.

[133] "Electrochemical Deposition of Conductive Superhydrophobic Zinc Oxide Thin Films",
M. Li, J. Zhai, H. Liu, Y. Song, L. Jiang, D. Zhu, J. Phys. Chem. B **107** (2003) 9954.

[134] "Thermal Decomposition of Surfactant Coatings on Co and Ni Nanocrystals",
V. Pérez-Dieste, O. M. Castellini, J. N. Crain, M. A. Eriksson, A. Kirakosian, J. -L. Lin, J. L. McChesney, F. J. Himpsel, C. T. Black, C. B. Murray, Appl. Phys. Lett. **83** (2003) 5053.

[135] "Desorption of surfactant and sintering of surface-modified $Pd_xNi_{1-x}$ nanoparticles",
K. -W.Wang, S. -R. Chung, W. -H. Hung, T. P. Perng, Appl. Surf. Sci. **252** (2006) 8751.

[136] "Powder diffraction pattern of ZnO", JCPDS #75-1526.

[137] "Low-temperature growth of ZnO nanorods by chemical bath deposition",
S. –H. Yi, S. –K. Choi, J. –M. Jang, J. –A. Kim,W. –G. Jung, J. Coll. Int. Sci. **313** (2007) 705.

[138] "Control of ZnO nanorod array alignment synthesized via seeded solution growth",
Y. –J. Lee, T. L. Sounart, D. A. Scrymgeour, J. A. Voigt, J. W. P. Hsu, J. Cryst. Growth **304** (2007) 80.

[139] "Hybrid polymer/metal oxide solar cells based on ZnO columnar structures",
A. M. Peiró , P. Ravirajan, K. Govender, D. S. Boyle, P. O'Brien, D. D. C. Bradley, J. Nelson, J. R. Durrant, J. Mater. Chem. **16** (2006) 2088.

[140] "Synthesis of size-tunable ZnO nanorod arrays from $NH_3 \cdot H_2O/ZnNO_3$ solutions",
K. Yu, Z. Jin, X. Liu, Z. Liu, Y. Fu, Mater. Lett. **61** (2007) 2775.

[141] "Self-assembled ZnO agave-like nanowires and anomalous superhydrophobicity",
Y. H. Yang, Z. Y. Li, B.Wang, C. X.Wang, D. H. Chen, G. W. Yang, J. Phys.: Condens. Mat. **17** (2005) 5441.

[142] "Superhydrophobic Films from Raspberry-like Particles",
W. Ming, D. Wu, R. van Benthem, G. de With, Nano Lett. **5** (2005) 2298.

[143] "Superhydrophobicity on Two-Tier Rough Surfaces Fabricated by Controlled Growth of Aligned Carbon Nanotube Arrays Coated with Fluorocarbon",
L. Zhu, Y. Xiu, J. Xu, P. A. Tamirisa, D. W. Hess, C. -P. Wong, Langmuir **21** (2005) 11208.

[144] "Superhydrophobic states",
A. Lafuma, D. Quéré, Nat. Mater. **2** (2003) 457.

[145] "The Wetting of Gold and Silicon Nanoscale Arrays",
M. –V. Meli, R. B. Lennox, Langmuir **23** (2007) 1619.

[146] "From micro to nano contacts in biological attachment devices",
E. Arzt, S. Gorb, R. Spolenak, Proc. Natl. Acad. Sci. U.S.A. **100** (2003) 10603.

[147] "Ferroelectric Lithography of Multicomponent Nanostructures",
S. V. Kalinin, D. A. Bonnell, T. Alvarez, X. J. Lei, Z. H. Hu,. R. Shao, J. H. Ferris, Adv. Mater. **16** (2004) 795.

[148] "Planned Nanostructures of Colloidal Gold via Self-Assembly on Hierarchically Assembled Organic Bilayer Template Patterns with In-situ Generated Terminal Amino Functionality",
S. Liu, R. Maoz, J. Sagiv, Nano Lett. **4** (2004) 845.

150

[149] "Nonlithographic Micro- and Nanopatterning of $TiO_2$ Using Polymer Stamped Molecular Templates",
H. Tokuhisa, P. T. Hammond, Langmuir **20** (2004) 1436.

[150] "Chip and solution detection of DNA hybridization using a luminescent zwitterionic polythiophene derivative",
K. P. R. Nilsson, O. Inganäs, Nat. Mater. **2** (2003) 419.

[151] "Nanoscale patterning with block copolymers",
S. Krishnamoorthy, C. Hinderling, H. Heinzelmann, Mater. Today **9** (2006) 40.

[152] "Fabrication of light absorbing $TiO_2$ µ-donuts",
N. Saleema, M. Farzaneh, R. W. Paynter, Materials Letters **63** (2009) 233.

[153] "Bio-nanopatterning of Surfaces",
P. M. Mendes, C. L. Yeung, J. A. Preece, Nanoscale Res. Lett. **2** (2007) 373.

[154] "Micro- and Nanopatterning Techniques for Organic Electronic and Optoelectronic Systems",
E. Menard, M. A. Meitl, Y. Sun, J. –U. Park, D. J. –L. Shir, Y. –S. Nam, S. Jeon, J. A. Rogers, Chem. Rev. **107** (2007) 1117.

[155] "Controlled patterning of polymer films using an AFM tip as a nano-hammer",
G. Li, L. W Burggraf, Nanotechnology **18** (2007) 245302.

[156] "The construction of orientation-dependent crystal growth and etch rate functions II: Application to wet chemical etching of silicon in potassium hydroxide",
E. van Veenendaal, J. van Suchtelen, W. J. P. van Enckevort, K. Sato, A. J. Nijdam, J. G. E. Gardeniers, M. Elwenspoek, J. Appl. Phys. **87** (2000) 8732.

[157] "Templated Fabrication of Periodic Metallic Nanopyramid Arrays", C. –H. Sun, N. C. Linn, P. Jiang, Chem. Mater. **19** (2007) 4551.

[158] "New structure for corner compensation in anisotropic KOH etching",
P. Enoksson, J. Micromech. Microeng. **7** (1997) 141.

[159] "The Influence of Defects on the Morphology of Si (111) Etched in $NH_4F$",
H. Zhou, J. Fu, R. M. Silver, J. Phys. Chem. B **109** (2005) 23386.

[160] "Morphological-Studies of Binary Homopolymer Block-Copolymer Blends - Effect of Molecular-Weight",
C. Prahsarn, A. M. Jamieson, Polymer **38** (1997) 1273.

[161] "Thermal behavior and surface morphology studies on polystyrene grafted sago starch",
P. Janarthanan, W. Md, Z. W. Yunus, M. B. Ahmad, J. Appl. Polym. Sci. **90** (2003) 2053.

[162] "Preparation of PMMA/SiO$_2$ composite particles via emulsion polymerization",
Y. Yang, Y. Dan, Colloid. Polym. Sci. **281** (2003) 794.

[163] "Microcontact Printing of Alkanephosphonic Acids on Aluminum: Pattern Transfer by Wet Chemical Etching",
L. B. Goetting, T. Deng, G. M. Whitesides, Langmuir **15** (1999) 1182.

[164] "Relative effect of extra-atomic relaxation on Auger and binding-energy shifts in transition metals and salts",
S.P. Kowalczyk, L. Ley, F.R. McFeely, R.A. Pollak, D.A. Shirley, Phys. Rev. B **9** (1974) 381.

[165] "Electronic Core Levels of Zinc Chalcogenides",
D. W. Langer, C. J. Vesely, Phys. Rev. B **2** (1970) 4885.

[166] "Fabrication of TiO$_2$ μ-donuts by gel-sol spin-coating using a polymer mask",
N. Saleema, M. Farzaneh, R. W. Paynter, Appl. Surf. Sci. **255** (2009) 5837.

[167] "Comparing the growth of PVD silver nanoparticles on ultra thin fluorocarbon plasma polymer films and self-assembled fluoroalkyl silane monolayers",
X. Wang, J. Zuo, P. Keil, G. Grundmeier, Nanotechnology **18** (2007) 265303.

[168] "Plasma polymer films rf sputtered from PTFE under various argon pressures",
V. Stelmashuk, H. Biederman, D. Slavínská, J. Zemek, M. Trchová, Vacuum **77** (2005) 131.

[169] "Deposition of PTFE thin films by RF plasma sputtering on 1 0 0 silicon substrates",
D.S. Bodas, A.B. Mandale, S.A. Gangal, Appl. Surf. Sci. **245** (2005), 202.

[170] "Adhesion of freezing precipitates to aircraft surfaces",
Optima Specialty Chemicals and Technology Inc., November 1996, TP 12860E, Safety and Security Transport Canada.

[171] "Ice releasing block-copolymer coatings",
H. H. G. Jellinek, H. Kachi, S. Kittaka, M. Lee, R. Yokota, Colloid and Polymer Sci. **256** (1978) 544.

[172] "Mechanical Strength of Thin Film of Metals",
J. W. Beams, J. B. Breazeale, W. L. Bart, Physical Review **100** (1955) 1657.

[173] "The Adhesion and Strength properties of Ice",
L. E. Raraty, D. Tabor, Proc. R. Soc. Lond. A, **245** (1958) 184.

[174] "Depth sensitivity of wetting: monolayers of omega-mercapto ethers on gold",
C. D. Bain, G. M. Whitesides, J. Am. Chem. Soc. **110** (1988) 5897.

## My list of publications

### Refereed Journal Papers:

1. "Fabrication of light absorbing $TiO_2$ μ-donuts", **N. Saleema,** M. Farzaneh, R. W. Paynter, Materials Letters 63 (2009) 233–235.

2. "Fabrication of $TiO_2$ μ-donuts by gel-sol spin-coating using a polymer mask", **N. Saleema,** M. Farzaneh, R. W. Paynter, Applied Surface Science 255 (2009) 5837–5842.

3. "Thermal effect on superhydrophobic performance of stearic acid modified ZnO nanotowers", **N. Saleema,** M. Farzaneh, Applied Surface Science, 254 (2008) 2690.

### Book Chapters:

4. "Effect of temperature on superhydrophobic zinc oxide nanotowers", **N. Saleema,** D. K. Sarkar, and M. Farzaneh, Book chapter, Contact Angle, Wettability and Adhesion, Volume 5, Part-3, BRILL publishers, 2008.

### Refereed Conference Papers:

5. "Superhydrophobic ZnO nanotowers", **N. Saleema,** D. K. Sarkar, M. Farzaneh and E. Sacher, Proceedings of Nanotech 2006, Boston, pp. 158-161 (2006).

### Conferences attended (oral and poster presentations):

1. "Ice Adhesion on Superhydrophobic Nanostructured Dielectric Coatings", **N. Saleema,** M. Farzaneh, R. W. Paynter
**Poster presentation,** INOR2008 (Inorganic Materials by Elsevier Science), 26-30 September 2008, Dresden, Germany

2. "Nanostructured dielectric coatings for prevention of ice accretion on high-voltage insulator surfaces", **N. Saleema,** M. Farzaneh, R. W. Paynter
**Oral and Poster Presentation,** Functional Coatings and Surface Engineering Symposia, 1-4 June 2008, Montréal, QC, Canada

3. "Superhydrophobic properties of stearic acid passivated zinc oxide nanotowers", **N. Saleema,** M. Farzaneh, R. W. Paynter
**Poster presentation,** Nano 2007, NanoQuébec, 7 February 2007, Montréal, QC, Canada

4. "Effect of temperature on superhydrophobic zinc oxide nanotowers", **N. Saleema**, D. K. Sarkar, and M. Farzaneh
**Oral Presentation,** Fifth International Symposium on Contact Angle Wettability and Adhesion, Session IV, 21-23 June 2006, Toronto, Canada


**Colloquia (oral presentations):**

1. "Superhydrophobic and icephobic properties of dielectric-coated nanostructured aluminum surfaces", **N. Saleema**, M. Farzaneh & R. Paynter, 10$^{th}$ Annual Colloquium of CIGELE/INGIVRE, Université du Québec à Chicoutimi, June 2008.

2. "Nanostructured Dielectric Thin Films for Icephobic Applications", **N. Saleema**, M. Farzaneh & R. Paynter, 9$^{th}$ Annual Colloquium of CIGELE/INGIVRE, Université du Québec à Chicoutimi, June 2007.

3. "Effect of temperature on superhydrophobic ZnO nanotowers and their surface morphology", **N. Saleema**, M. Farzaneh, D. K. Sarkar & E. Sacher, 8$^{th}$ Annual Colloquium of CIGELE/INGIVRE, Université du Québec à Chicoutimi, June 2006.

# APPENDIX 1

## PHYSICAL PROPERTIES OF SOL-GEL DERIVED TiO$_2$ THIN FILMS

As a part of the optimization processes, the thickness of TiO$_2$ films on Si (100) substrates was varied by varying the molar concentration of the TBOT sol between 0.10M and 0.30M. The thickness of each film was evaluated by RBS measurements using 2 MeV He ions and spectra from silicon and germanium samples were used for calibration. Figure A1.1 shows the RBS spectra of the TiO$_2$ films and Table A1.1 shows the thickness information obtained using GISA 3 software. The thickness of the films varied between 35 and 125 nm.
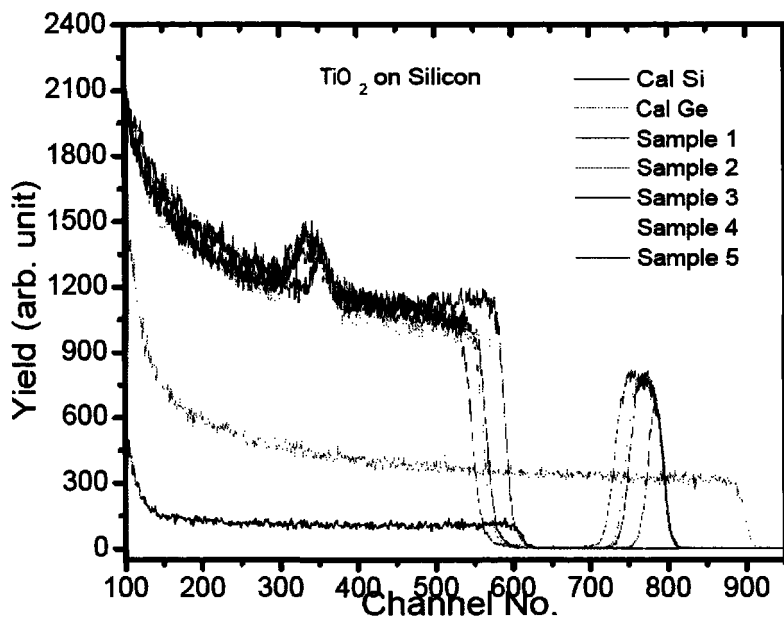
**Figure A1.1.** RBS spectra of films deposited using various molar concentrations of $TiO_2$.

**Table A1.1.** $TiO_2$ thickness information based on RBS analysis using GISA 3 software.

| Sample No. | Molar conc. of TiO₂ (M) | Thickness (nm) | Composition (at%) | |
|---|---|---|---|---|
| | | | Ti | O |
| Sample 1 | 0.30 | 125 | 33.3 | 66.7 |
| Sample 2 | 0.25 | 100 | 33.3 | 66.7 |
| Sample 3 | 0.20 | 85 | 33.3 | 66.7 |
| Sample 4 | 0.15 | 55 | 33.3 | 66.7 |
| Sample 5 | 0.10 | 35 | 33.3 | 66.7 |

157

The XRD measurements of the different films confirmed that the sol-gel TiO$_2$ thin films are composed of the anatase phase. **Figure A1.2.** shows the XRD spectra of the TiO$_2$ films of varying thicknesses within 2θ values between 20° and 55°.
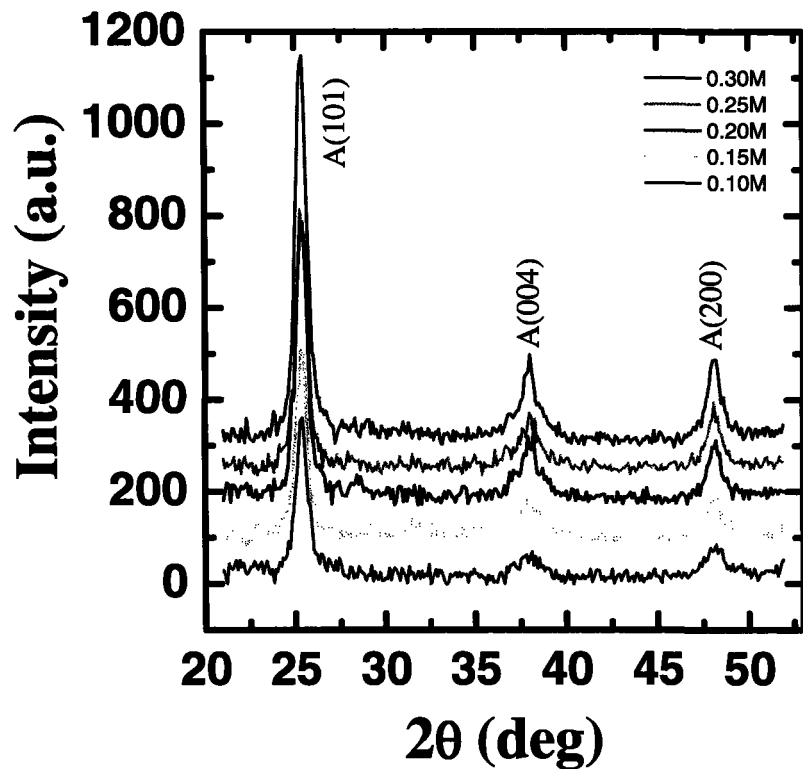


**Figure A1.2.** XRD pattern of sol-gel derived TiO$_2$ films of varying thicknesses coated on Si (100) substrates [A=Anatase].

The TiO$_2$ film of thickness 100 nm was chosen for ice adhesion investigations as the dielectric constant of the anatase phase TiO$_2$ of film thickness 100 nm (measured using cross-sectional SEM) obtained using similar procedure by Sarkar *et al.* was reported to be 80 and in the higher range [113,114]. The physical properties being in consistent with those reported by Sarkar *et al.*, the electrical properties are also expected to be similar and therefore the dielectric constant of the TiO$_2$ films prepared in this study of the same thickness using same procedures is considered to be about 80.